The oncometabolite D-2-hydroxyglutarate promotes DNA hypermethylation at lineage-specific enhancers controlling microglial activation in IDH^{mut} gliomas

Alice Laurenge[1,2*], Pietro Pugliese[1*], Quentin Richard[1], Bertrand Mathon[3], Stéphanie Jouannet[1], Yvette Hayat[1], Sarah Scuderi[1], Laurent Capelle[3Ŧ], Pauline Marijon[3], Karim Labreche[1,4], Agustí Alentorn[1,2], Maïté Verreault[1], Ahmed Idbaih[1,2], Cristina Birzu[1,2], Emmanuelle Huillard[1], Nina Pottier[1], Aurore Desmons[5], Inès Fayache[5], Garrett A. Kaas[6], Philip J. Kingsley[7], Lawrence J. Marnett[8], Eric Duplus[9], Elias El-Habr[10], Lucas A. Salas[11], Karima Mokhtari[1,12], Suzanne Tran[1,12], Mehdi Touat[1,2], Franck Bielle[1,12], Mario L. Suvà[13,14], Antonio Iavarone[15], Michele Ceccarelli[16], Michel Mallat[1], Marc Sanson[1,2,17], Luis Jaime Castro-Vega[1]

[1]Sorbonne Université, Inserm UMRS 1127, CNRS UMR 7225, ICM – Institut du Cerveau, F-75013 Paris, France; Équipe Labellisée Par La Ligue Nationale Contre Le Cancer.

[2]Department of Neuro-Oncology, AP-HP, Hôpital Pitié-Salpêtrière, F-75013 Paris, France.

[3]Department of Neurosurgery, AP-HP, Hôpital Pitié Salpêtrière, F-75013 Paris, France.

[4]Sorbonne Université, CinBioS, UMS 37 PASS Production de données en Sciences de la vie et de la Santé.

[5]Clinical Metabolomic Department, AP-HP, Hôpital Saint Antoine, Sorbonne Université, Paris, France.

[6]Division of Genetic Medicine, Vanderbilt University Medical Center, Nashville, TN, USA.

[7]Department of Biochemistry, Vanderbilt University, Nashville, TN, USA.

[8]Departments of Biochemistry, Chemistry, and Pharmacology, Vanderbilt Institute of Chemical Biology, Vanderbilt-Ingram Cancer Center, Vanderbilt University School of Medicine, Nashville, TN, USA.

[9]Sorbonne Université, IBPS, CNRS UMR8256, INSERM ERL1114, Biological Adaptation and Aging, Paris, France.

[10]Sorbonne Université, IBPS, CNRS UMR8246, Inserm U1130, Neuroscience Paris Seine Laboratory, Paris, France.

[11]Geisel School of Medicine at Dartmouth, Dartmouth Cancer Center, Lebanon, NH, 03756, USA.

[12]Department of Neuropathology, AP-HP, Hôpital Pitié Salpêtrière, F-75013 Paris, France.

[13]Department of Pathology and Krantz Family Center for Cancer Research, Massachusetts General Hospital and Harvard Medical School, Boston, MA, 02114, USA.

[14]Broad Institute of Harvard and MIT, Cambridge, MA 02142, USA.

[15]Department of Neurological Surgery and Department of Biochemistry, Sylvester Comprehensive Cancer Center, University of Miami Miller School of Medicine, Miami, FL, USA.

[16]Department of Public Health Sciences and Sylvester Comprehensive Cancer Center, University of Miami Miller School of Medicine, Miami, FL, USA.

[17]Onconeurotek Tumor Bank, AP-HP, Hôpital Pitié-Salpêtrière, F-75013 Paris, France.

[*]These authors contributed equally to this work

[Ŧ]Dr. Laurent Capelle passed away in June, 2023. This study is dedicated to his memory.

Corresponding authors:

Marc Sanson, M.D., Ph.D.

Email address: marc.sanson@aphp.fr

Genetics & Development of Brain Tumors

ICM - Paris Brain Institute, 75013, Paris, France

Luis J. Castro-Vega, M.D., Ph.D.

Email address: luis.castrovega@icm-institute.org

Genetics & Development of Brain Tumors

ICM - Paris Brain Institute, 75013, Paris, France

Abstract

Tumor-associated macrophages and microglia (TAMs) are highly abundant myeloid cells in gliomas, with their phenotypes and immune responses shaped by ontogeny and microenvironment. TAMs display distinctive transcriptional programs based on the IDH status of tumors, yet the underlying signaling mechanisms remain largely unknown. Herein, we uncover that CD11B+ myeloid cells in human IDH-mutant gliomas exhibit DNA hypermethylation, predominantly at distal enhancers. This hypermethylation impairs the binding of core transcription factors that govern microglial responses, resulting in reduced expression of inflammatory and glycolytic metabolism programs. Prolonged exposure of human primary microglia to D-2-hydroxyglutarate (D-2HG) inhibits TET-mediated demethylation at lineage-specific enhancers, evidenced by elevated 5mC/5hmC ratios near binding motifs. D-2HG-treated microglia showed reduced proinflammatory capacity and enhanced oxidative phosphorylation, consistent with the remodeled enhancer landscape. Conversely, depletion of D-2HG following treatment of a glioma patient with an IDH-mutant inhibitor unleashed microglial reactivity, as assessed by snRNA-seq. Our findings provide a mechanistic rationale for the hyporesponsive state of microglia in IDH-mutant gliomas and support the concept that oncometabolites may disrupt the function of immune cells residing in the tumor microenvironment.

Keywords: D-2HG, 5mC, 5hmC, Glioma, TAMs, IDH mutation, Tumor Microenvironment

Introduction

Diffuse gliomas are the most common malignant primary brain tumors and are refractory to standard therapies[1]. A high proportion of these tumors harbor an IDH mutation that confers the neomorphic ability to convert α-ketoglutarate (α-KG) to (D)-2-hydroxyglutarate (D-2HG)[2]. It is believed that D-2HG drives cellular transformation by inhibiting α-KG-dependent dioxygenases, including the TET family of DNA demethylases, KDMs histone demethylases, and FTO/ALKBH RNA demethylases, ultimately leading to widespread epigenomic dysregulation and blockage of cell differentiation[3]. Little is known about the tumor cell-extrinsic effects of this oncometabolite, which accumulates in the tumor microenvironment (TME)[4,5]. Emerging evidence indicates that D-2HG released by IDH^{mut} cells suppresses T cells and impairs the metabolism of infiltrating macrophages, dendritic cells, and CD8+ T cells via non-epigenetic mechanisms[6-10]. It remains to be determined whether D-2HG can reshape the epigenetic landscape of the TME, particularly in resident microglia, which are abundant in IDH^{mut} gliomas and are exposed to this oncometabolite from tumor initiation.

Tumor-associated macrophages and microglia (TAMs) comprise almost 40% of the tumor mass and play critical roles in tumor progression[11]. As such, these cells may serve as prognostic biomarkers and therapeutic targets[12,13]. TAMs are plastic cells, and their phenotypes and immune responses are determined by both ontogeny and microenvironment[14,15]. Previous studies on IDH^{wt} glioma models have revealed that resident microglia and monocyte-derived macrophages (MDMs) display distinctive transcriptional and chromatin landscapes[16]. Transcriptional differences have also been observed in the myeloid compartment of gliomas as a function of the IDH status[17,18]. In IDH^{wt} tumors, MDMs and microglial cells exhibit expression changes associated with activation, including elevated expression of MHC class genes[17]. In contrast, in IDH^{mut} gliomas, these cells display a hyporeactive phenotype similar to that of homeostatic microglia in non-tumor tissues[17].

The relative proportion of MDMs and microglial cells varies according to IDH^{mut} status[17-21] and/or tumor grade[22,23]. Glioma progression involves cellular competition, wherein infiltrating macrophages overtake the niche occupied by resident microglia[24,25]. Recent single-cell RNA-seq studies of the myeloid compartment in human gliomas have further revealed subsets of MDMs with mesenchymal-like, lipid, and hypoxic/glycolytic signatures, as well as subsets of inflammatory and oxidative phosphorylation (OXPHOS)-related microglia[20-22,24,26], some of which have been linked to clinical outcomes. Additionally, it has been reported that myeloid cells express overlapping immunomodulatory activity programs, regardless of their ontological origin[23]. The epigenetic changes, such as DNA methylation, that drive the transcriptional programs and cell states of TAMs in human glioma, along with the effects of tumor-derived signals on the TAM methylome remain largely uncharacterized.

Inhibition of TET-mediated demethylation by D-2HG in tumor cells accounts for the DNA hypermethylation observed in IDH^{mut} gliomas[27]. Given the elevated concentrations of this oncometabolite in the TME and its uptake by myeloid cells[9,28], we hypothesized that such a mechanism could also be at play in the CD11B+ myeloid cells of these tumors, thus contributing to both epigenetic intratumoral heterogeneity and altered immune functions. To investigate whether and how TAMs in IDH^{mut} gliomas exhibit functional changes in DNA methylation, we first profiled the bulk transcriptome and methylome of CD11B+ myeloid cells isolated from a well-characterized series of human gliomas and non-tumor tissues. Our findings revealed that myeloid cells in IDH^{mut} tumors exhibit DNA hypermethylation at enhancer elements that regulate gene networks involved in microglial activation. We demonstrated the direct effects of D-2HG on TET-mediated DNA demethylation at lineage-specific enhancers in primary cultures of human microglia, providing a mechanistic foundation for the hyporesponsive behavior of these cells in IDH^{mut} gliomas. These results have implications for therapies targeting IDH-mutant enzymes or for strategies aimed at repolarizing TAMs.

Results

Study design

To determine the mechanistic underpinnings of the TAM phenotype associated with the IDH status, we analyzed the bulk DNA methylome and/or transcriptome of CD11B+ myeloid cells isolated by magnetic sorting from adult-type human diffuse gliomas (n=36), comprising IDH^{wt}, IDH^{mut} oligodendrogliomas, and IDH^{mut} astrocytomas. In addition, we analyzed available methylome data of CD11B+ cells from normal brains, isolated using a similar method and profiled with the same technology[29] (Fig. 1A). To control for potential confounding variables, the samples were matched by age and sex, while being fully characterized for their clinical, pathological, and genetic features (Supplementary Table S1). Contamination of CD11B+ fractions by tumor cells was assessed by analyzing IDH1 R132H or TERT C228T/C250T promoter mutations using droplet digital PCR (ddPCR), and further verified through RNA-seq-based analysis of IDH variant allelic frequency (Supplementary Fig. S1A and S1B). The estimated purity of the CD11B+ samples included in downstream analyses reached ~95%. This analysis ruled out the possibility that TAMs from our study cohort harbored the IDH1 R132H mutation to a significant extent, as previously reported[30].

CD11B+ myeloid cells in human IDH^{mut} gliomas display global DNA hypermethylation

To confirm the DNA methylation status of the cohort in relation to the IDH mutation, we first profiled glioma cell-enriched CD11B- fractions isolated from both IDH^{wt} and IDH^{mut} tumors (n=17, Supplementary Table S1) using MethylationEPIC (EPIC) arrays. Analysis of methylation levels across all probes targeting CpG sites confirmed that IDH^{mut} tumors display global hypermethylation, though with a high degree of heterogeneity, as previously reported[31-33] (Supplementary Fig. S2A and S2B). In total, 49,676 CpG sites were differentially methylated (absolute $\Delta\beta > 0.2$, FDR < 0.05), with 92.5% of these sites being hypermethylated in IDH^{mut} samples compared to IDH^{wt} glioma samples (Supplementary Fig. S2C). Analysis of the distribution across functional genomic regions revealed a high proportion of hypermethylated CpGs located in promoters and enhancers. Promoters were defined as genomic regions within -1.5 kb to +0.5 kb of the transcription start site (TSS), whereas

enhancers were defined as distal regulatory elements associated with robust FANTOM promoters within a range of up to 500 kb (FDR < 1e-5; Pearson's correlation), as outlined by the FANTOM5 consortium[34]. Our analysis confirmed that enhancers are particularly sensitive to hypermethylation in IDH^{mut} glioma cells[35] (Supplementary Fig. S2C and S2D).

We then examined methylome changes in the CD11B+ myeloid cell fraction isolated from gliomas (n=26) and normal brain tissues (n=6) (Supplementary Table S1). Principal component analysis (PCA) revealed distinct segregation of myeloid cells based on both tissue origin and IDH status along component 1, which accounted for 48% of the variance (Fig. 1B). Despite the substantial heterogeneity in methylome data in CD11B+ samples from IDH^{mut} tumors, we identified 37,198 differentially methylated CpG sites (absolute $\Delta\beta > 0.2$, FDR < 0.05) compared to CD11B+ cells from IDH^{wt} gliomas (Fig. 1C). Strikingly, similar to what was observed in glioma cells, CD11B+ samples from corresponding IDH^{mut} tumors exhibited a bias towards hypermethylation, particularly in regulatory regions (Fig. 1C). IDH^{wt} glioblastomas are known to be enriched in MDMs, whereas the TME of IDH^{mut} tumors is dominated by tissue-resident microglia[17,18]. However, the asymmetric distribution of the observed methylation changes suggests that this was not simply an effect of differences in cell composition. Indeed, global hypermethylation was also observed when comparing the DNA methylome of CD11B+ cells isolated from IDH^{mut} tumors to that of CD11B+ cells from normal brain tissues, both of which are predominantly composed of microglial cells (Fig. 1C). In this comparison, the number of differentially methylated CpG sites and genomic regions was higher, with a notable overlap in the regulatory regions that exhibited hypermethylation in both comparisons (Fig. 1D). Among these, the number and methylation levels of the affected enhancers, along with their overlap between the two comparisons, were greater than those observed for the promoters (Fig. 1D). Functional enrichment analysis of genes regulated by hypermethylated regulatory regions intersected in the two comparisons indicated roles in inflammatory responses, such as TNF-α, IFN-γ, and IL2/IL6 signaling, as well as in complement and hypoxia pathways (Fig. 1E and Supplementary Table S2).

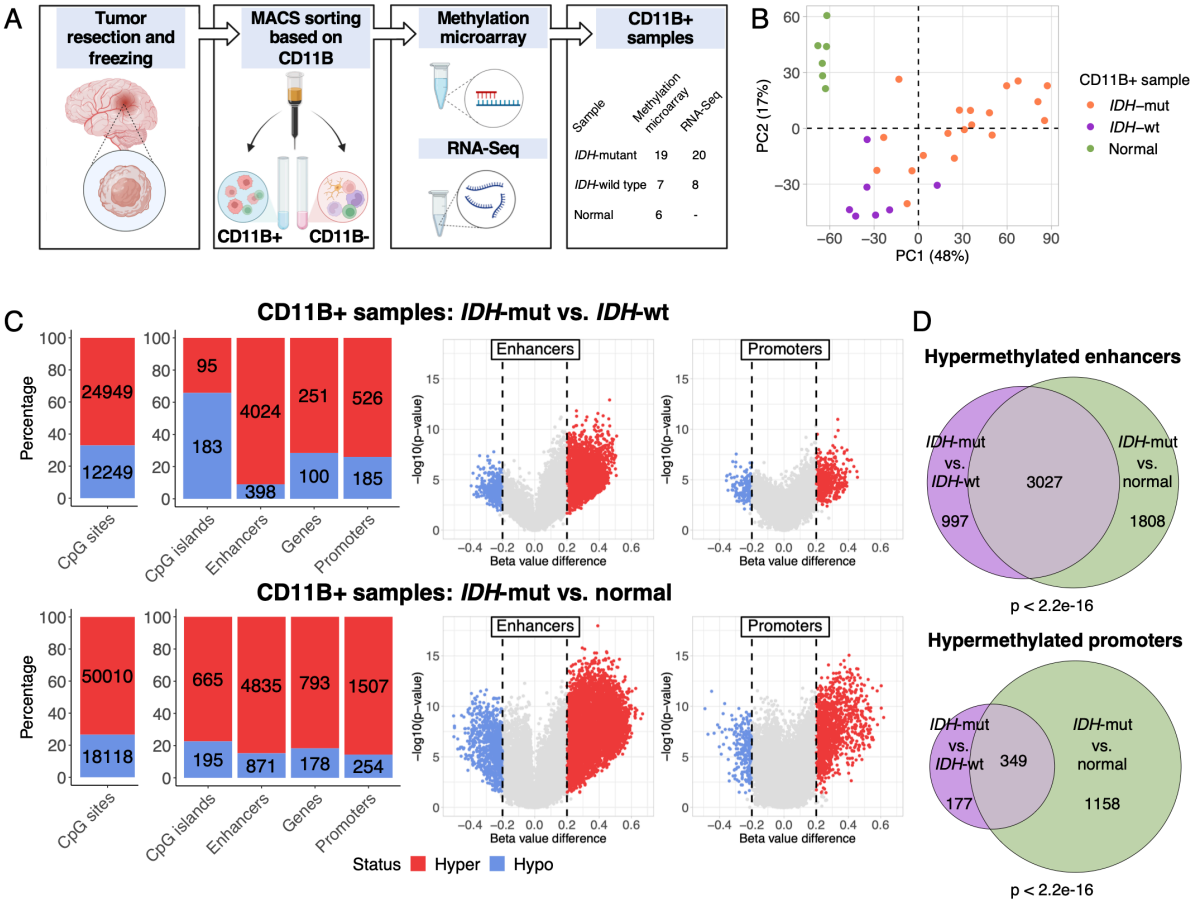
A
Tumor resection and freezing
MACS sorting based on CD11B
CD11B+
CD11B-
Methylation microarray
RNA-Seq
CD11B+ samples
Sample
Methylation microarray
RNA-Seq
IDH-mutant 19 20
IDH-wild type 7 8
Normal 6 -
B
PC2 (17%)
PC1 (48%)
CD11B+ sample
IDH–mut
IDH–wt
Normal
C
CD11B+ samples: IDH-mut vs. IDH-wt
Percentage
24949
12249
95
183
4024
398
251
100
526
185
CpG sites
CpG islands
Enhancers
Genes
Promoters
Enhancers
Promoters
−log10(p−value)
Beta value difference
CD11B+ samples: IDH-mut vs. normal
50010
18118
665
195
4835
871
793
178
1507
254
Status Hyper Hypo
D
Hypermethylated enhancers
IDH-mut vs. IDH-wt
IDH-mut vs. normal
997
3027
1808
p < 2.2e-16
Hypermethylated promoters
IDH-mut vs. IDH-wt
IDH-mut vs. normal
177
349
1158
p < 2.2e-16
E
Hypermethylated enhancers in CD11B+ samples of IDH-mut gliomas
TNFA SIGNALING VIA NFKB
INFLAMMATORY RESPONSE
ALLOGRAFT REJECTION
INTERFERON GAMMA RESPONSE
COMPLEMENT
HEME METABOLISM
IL2 STAT5 SIGNALING
HYPOXIA
APOPTOSIS
IL6 JAK STAT3 SIGNALING
PI3K AKT MTOR SIGNALING
REACTIVE OXYGEN SPECIES PATHWAY
GeneRatio
Count
FDR
F
Motifs enriched in hypermethylated enhancers
Motif p-value % of targets Best match
1e-356 36% SPI1
1e-161 27% AP-1
1e-98 21% CEBP
1e-90 19% RUNX
1e-68 8% IRF
1e-50 13% NFKB
Hypermethylated promoters in CD11B+ samples of IDH-mut gliomas
INFLAMMATORY RESPONSE
IL2 STAT5 SIGNALING
ALLOGRAFT REJECTION
INTERFERON GAMMA RESPONSE
KRAS SIGNALING UP
TNFA SIGNALING VIA NFKB
GeneRatio
Count
FDR
Motifs enriched in hypermethylated promoters
Motif p-value % of targets Best match
1e-35 32% SPI1
1e-16 9% IRF
1e-15 2% RUNX

Figure 1. DNA methylome profiling of CD11B+ cells underscores hypermethylation in the myeloid compartment of IDH^{mut} gliomas. (A) Overview of the *ex vivo* study workflow. Tumor samples (n=36) underwent enzymatic dissociation, followed by CD11B-based magnetic sorting. DNA and/or RNA extraction was performed on both CD11B+ and CD11B- fractions for downstream analyses. Available methylome data of CD11B+ cells from six normal brains were included as controls for comparisons. Clinical, pathological, and genetic annotations of the study cohort are detailed in Supplementary Table S1. **(B)** Principal component analysis performed using methylome data from around 600,000 CpG sites across the genome in CD11B+ samples from the study cohort. **(C)** Stacked bar charts (left) show absolute numbers and relative percentages of CpG sites and of four genomic regions with respect to the methylation status (absolute $\Delta\beta > 0.2$, FDR < 0.05) for the indicated comparisons. Volcano plots (right), colored by methylation status, depict the magnitude and extent of differentially methylated enhancers and promoters for the indicated comparisons. **(D)** Venn diagrams illustrate significant overlaps between hypermethylated enhancers (upper panel) or promoters (bottom panel) in CD11B+ cells from IDH^{mut} gliomas, compared to IDH^{wt} gliomas or normal brain tissues. P-values were computed using over-representation analysis (ORA). **(E)** Bubble plots indicate the hallmark gene sets enriched in the lists of genes exhibiting hypermethylated enhancers (n=3027) and promoters (n=349) in CD11B+ samples from IDH^{mut} gliomas in comparison to CD11B+ samples from IDHwt gliomas and normal brain tissues (Fig. 1D). The size and color code of each dot indicate the number of genes with significant enrichment for the indicated categories (FDR < 0.05). **(F)** Significant sequence motifs (ranked by p-value) enriched in hypermethylated enhancers and promoters in CD11B+ samples from IDH^{mut} gliomas, in comparison to CD11B+ samples from IDH^{wt} gliomas and normal brain tissues (Fig. 1D), were determined using HOMER.

Transcription factors (TFs) bind to specific DNA motifs on promoters and enhancers to control cell type-specific transcriptional programs, and their affinity can be modulated by methylation status[36-38]. Since a substantial proportion of hypermethylation observed in CD11B+ cells from IDH^{mut} tumors occurred in regulatory elements across both comparisons (Fig. 1D), we examined the enrichment of TF-binding motifs located within the identified hypermethylated regulatory regions. This analysis revealed an overrepresentation of 21 motifs in 349 hypermethylated promoters and 24 motifs in 3027 hypermethylated enhancers (p-value < 10^{-12}) (Fig. 1F). Notably, SPI1 (PU.1) was the most significantly enriched motif in both hypermethylated regulatory regions, accounting for 36% of enhancers and 32% of promoters. The other highly enriched motifs are bound by the core set of TFs that control an environment-dependent transcriptional network in microglial cells, such as C/EBP, AP-1, RUNX, and IRF[39], alongside NF-κβ. Collectively, these results revealed extensive differences in the DNA methylome of TAMs as a function of the IDH mutational status.

Hypermethylation correlates with reduced expression of inflammatory regulons in CD11B+ cells from human IDH^{mut} gliomas

To investigate the transcriptomic landscape of TAMs in gliomas, we performed RNA-seq on CD11B+ fractions (n=28, Supplementary Table S1). PCA showed a clear separation between samples derived from the IDH^{wt} and IDH^{mut} cases (Supplementary Fig. S3A). Differential expression analysis revealed 2714 upregulated genes and 1404 downregulated genes (log2FC > 1 or < -1, respectively; FDR < 0.05) in TAMs from IDH^{mut} compared to those from IDH^{wt} (Supplementary Table S3). We found a significant overlap between the list of downregulated genes in our CD11B+ sample series and those reported by Klemm et al., who further distinguished the expression changes between microglia and MDMs (Supplementary Fig. S3B). Notheworthy, the largest overlap occurred in downregulated genes within microglial cells from IDH^{mut} tumors, with 156 of the 357 genes falling into this category. Furthermore, a significant proportion of genes defining normal microglial signatures also intersected with the list of downregulated genes from our series of CD11B+ fractions in IDH^{mut} gliomas (Supplementary Fig. S3C). Enrichment analysis revealed that these downregulated genes were involved in proinflammatory pathways, including INF-γ/α response and IL6/JAK/STAT3 signaling, cell cycle/proliferation, hypoxia, glycolysis, and the acquisition of mesenchymal-like traits (Supplementary Fig. S3D).

DNA methylation is a key mechanism in the regulation of gene expression. To evaluate the impact of methylation on the observed transcriptional changes in CD11B+ cells isolated from IDH^{mut} gliomas, we intersected the list of differentially expressed genes with the list of differentially methylated promoters or enhancers. This analysis involved 36 CD11B+ samples, 18 of which had both sets of available data (Supplementary Table S1). In contrast to IDH^{mut} glioma cells, where methylation and expression changes have been shown to be uncoupled[35,40], myeloid cells from these tumors displayed confident overlaps in the expected direction. For instance, reduced gene expression was strongly associated with hypermethylation at promoters and enhancers (p-value=2.5e-14 and p-value=7.7e-18, respectively, over-representation analysis (ORA) (quadrant IV, Fig. 2a), while the occurrence

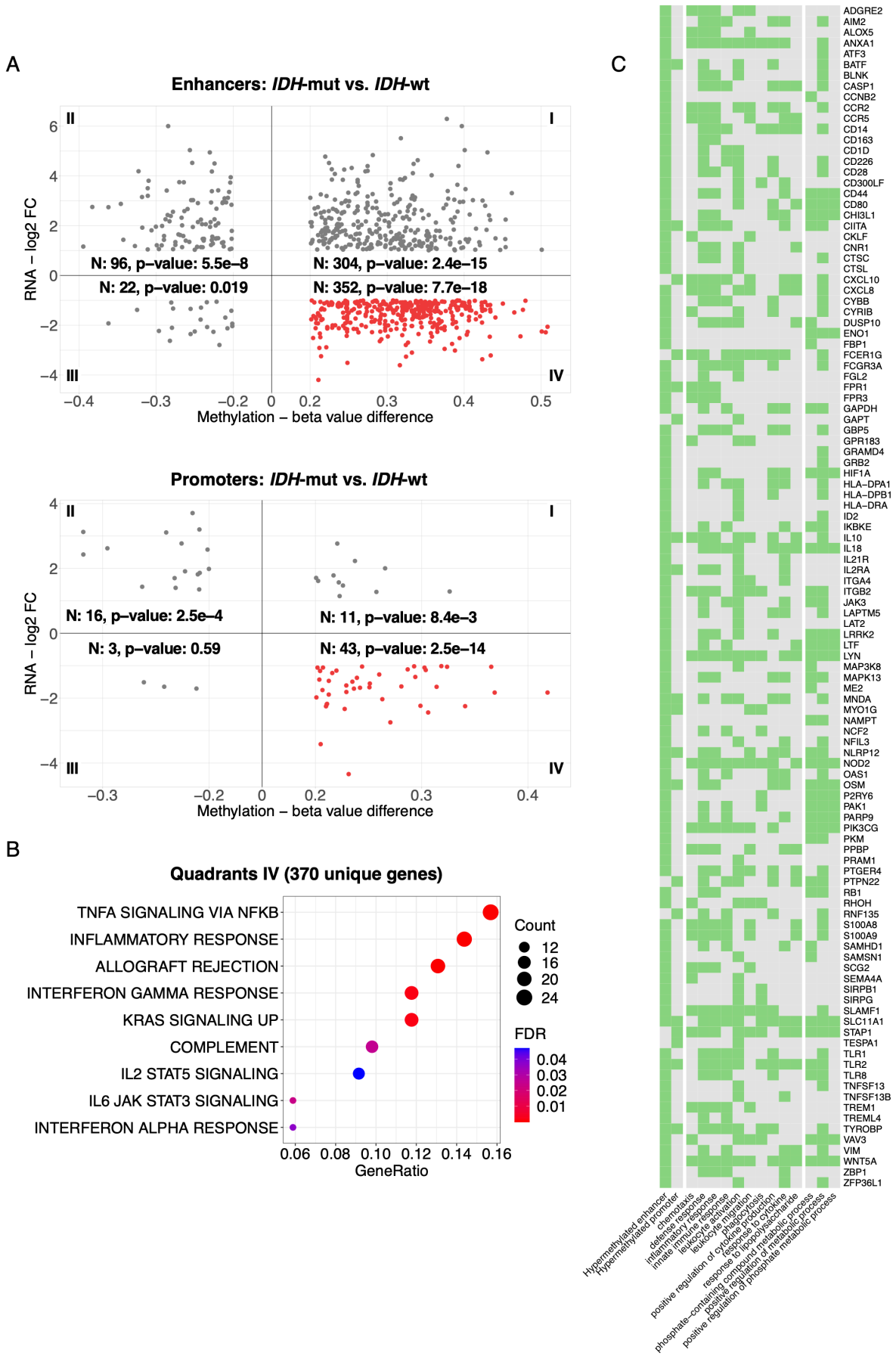
A
Enhancers: IDH-mut vs. IDH-wt
II
I
III
IV
N: 96, p–value: 5.5e–8
N: 304, p–value: 2.4e–15
N: 22, p–value: 0.019
N: 352, p–value: 7.7e–18
RNA – log2 FC
Methylation – beta value difference
Promoters: IDH-mut vs. IDH-wt
N: 16, p–value: 2.5e–4
N: 11, p–value: 8.4e–3
N: 3, p–value: 0.59
N: 43, p–value: 2.5e–14
B
Quadrants IV (370 unique genes)
TNFA SIGNALING VIA NFKB
INFLAMMATORY RESPONSE
ALLOGRAFT REJECTION
INTERFERON GAMMA RESPONSE
KRAS SIGNALING UP
COMPLEMENT
IL2 STAT5 SIGNALING
IL6 JAK STAT3 SIGNALING
INTERFERON ALPHA RESPONSE
GeneRatio
Count
12
16
20
24
FDR
0.04
0.03
0.02
0.01
C
ADGRE2
AIM2
ALOX5
ANXA1
ATF3
BATF
BLNK
CASP1
CCNB2
CCR2
CCR5
CD14
CD163
CD1D
CD226
CD28
CD300LF
CD44
CD80
CHI3L1
CIITA
CKLF
CNR1
CTSC
CTSL
CXCL10
CXCL8
CYBB
CYRIB
DUSP10
ENO1
FBP1
FCER1G
FCGR3A
FGL2
FPR1
FPR3
GAPDH
GAPT
GBP5
GPR183
GRAMD4
GRB2
HIF1A
HLA–DPA1
HLA–DPB1
HLA–DRA
ID2
IKBKE
IL10
IL18
IL21R
IL2RA
ITGA4
ITGB2
JAK3
LAPTM5
LAT2
LRRK2
LTF
LYN
MAP3K8
MAPK13
ME2
MNDA
MYO1G
NAMPT
NCF2
NFIL3
NLRP12
NOD2
OAS1
OSM
P2RY6
PAK1
PARP9
PIK3CG
PKM
PPBP
PRAM1
PTGER4
PTPN22
RB1
RHOH
RNF135
S100A8
S100A9
SAMHD1
SAMSN1
SCG2
SEMA4A
SIRPB1
SIRPG
SLAMF1
SLC11A1
STAP1
TESPA1
TLR1
TLR2
TLR8
TNFSF13
TNFSF13B
TREM1
TREML4
TYROBP
VAV3
VIM
WNT5A
ZBP1
ZFP36L1
Hypermethylated enhancer
Hypermethylated promoter
chemotaxis
defense response
inflammatory response
innate immune response
leukocyte activation
leukocyte migration
phagocytosis
positive regulation of cytokine production
response to cytokine
response to lipopolysaccharide
phosphate–containing compound metabolic process
positive regulation of metabolic process
positive regulation of phosphate metabolic process

Figure 2. Integration of significant changes in the transcriptome and methylome displayed by CD11B+ myeloid cells in IDH^{mut} gliomas. (A) Cartesian diagrams represent genes (dots) exhibiting significant changes in both expression (Y-axis) and methylation (X-axis) at promoters or enhancers in CD11B+ cells from IDH^{mut} vs. IDH^{wt} gliomas. The total number of genes displaying differential methylation and expression changes is indicated for each quadrant. Over-representation of canonical methylation/expression associations (quadrants II and IV) and under-representation of non-canonical associations (quadrants I and III) were evaluated using ORA and URA, respectively. Quadrants IV (highlighted in red) indicate genes of interest exhibiting downregulation and hypermethylation at either promoters or enhancers. **(B)** Bubble plot indicates the hallmark gene sets enriched in the integrative gene list (n=370) obtained by combining quadrants IV from both promoters and enhancers analyses. The size and color code of each dot indicate the number of genes with significant enrichment in the corresponding categories (FDR < 0.05). **(C)** The plot illustrates a subset of genes (n=110) from the integrative list that are enriched (FDR < 0.05) in Gene Ontology biological processes related to immune response and metabolism. The hypermethylation status at promoter and enhancer regions is also indicated. Positive or negative hits are represented in green or gray, respectively.

of genes showing non-canonical associations, such as overexpression coupled with hypermethylation at promoters and enhancers, was lower than expected (quadrants I, Fig. 2A) (p-value=8.4e-3 and 2.4e-15, under-representation analysis (URA)). This Integrative analysis of methylome and transcriptome changes revealed 370 unique genes with a hypermethylated enhancer and/or promoter linked to downregulated expression in CD11B+ cells from IDH^{mut} tumors (Supplementary Table S4).

The integrative gene list contained key factors involved in TNF-α signaling via NF-κβ, IL6/JAK/STAT3 signaling, and response to IFN-γ/α (Fig. 2B; Supplementary Table S4). Biological processes such as chemotaxis, leukocyte activation, and positive regulation of metabolism were also enriched in this gene list (Fig. 2C). Among the genes whose downregulation was associated with hypermethylation in both regulatory regions, we found CIITA, the most important transactivator of MHC class II, the cytokine oncostatin M (OSM), and myeloid receptors, such as formyl peptide receptor 1 (FPR1) and Toll-like receptor 2 (TLR2) (Fig. 2C). Hypermethylation at either the promoter or enhancer, together with reduced expression, was observed for HLA genes, including proinflammatory cytokines CXCL10, IL18, and CXCL8; chemokine receptors CCR2/5, FPR3, and TLR1/8; master regulators of glycolysis/hypoxia HIF1A, PKM, ENO1, CD44; and signaling components or enzymes

involved in cytokine production and NAD biosynthesis, such as TYROBP and NAMPT, respectively (Fig. 2C). Therefore, hypermethylation appears to affect various levels of signaling regulation within inflammatory pathways, and possibly the activation of myeloid cells.

To assess the effect of DNA hypermethylation on TF binding at the enhancers highlighted in quadrants I and IV (Fig. 2A), we estimated TF activity by examining high-confidence TF-gene interactions (n=1,209 human TFs)[41,42] in our RNA-seq data from CD11B+ samples. Analysis of regulons identified 45 TFs with differential activity (FDR <0.05; Wilcoxon's test) based on the IDH status of the corresponding tumors, with the majority of TFs showing decreased activity in IDH^{mut} gliomas (Fig. 3A). Consistent with the binding motifs enriched in the entire repertoire of hypermethylated enhancers (Fig. 1F), this analysis emphasized that lineage-determining and stimulus-related microglial TFs are repressed from DNA binding by methylated CpGs in CD11B+ cells from IDH^{mut} gliomas. Among these, SPI1 (PU.1), the AP-1 complex (ATF2, FOS, and JUN), and CEBPB have previously been shown to be sensitive to methylation[43-45], whereas NFATC2, RELA, and STAT3 have been associated with microglial super-enhancers[39]. Similar results were observed when the entire set of hypermethylated promoters was used (Supplementary Fig. S4). In addition, these analyses revealed reduced activity of MYC and HIF1A (Fig. 3A; Supplementary Fig. S4).

In contrast, a few TFs appeared activated in these cells, including TP63, TP73, SNAI1, CTNNB1, EPAS1/HIF2A, and KLF4. In such cases, methylated CpGs could promote TF binding[46]. Upon closer examination of specific TFs inactivated in CD11B+ cells from IDH^{mut} gliomas, a network inference analysis also suggested that TF target genes implicated in inflammation and antigen presentation were effectively downregulated as a result of disrupted cooperative effects of core microglial TFs (Fig. 3B). Similarly, targets that are positively regulated by both MYC and HIF1A, which play roles in the response to hypoxia and glycolysis, were more enriched in the list of downregulated genes in CD11B+ cells from IDH^{mut} vs. IDH^{wt} tumors, than the targets regulated by each individual TF (Fig. 3C).

A

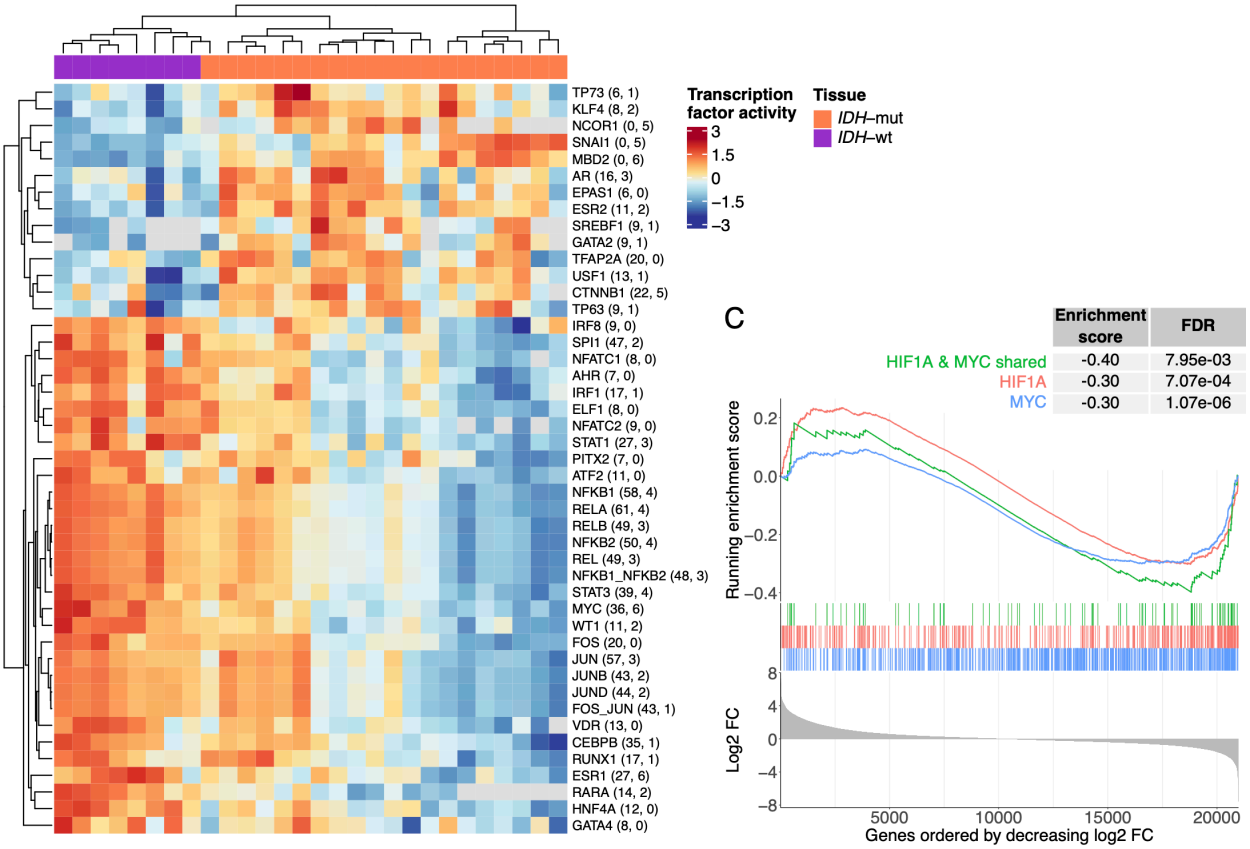
TP73 (6, 1)
KLF4 (8, 2)
NCOR1 (0, 5)
SNAI1 (0, 5)
MBD2 (0, 6)
AR (16, 3)
EPAS1 (6, 0)
ESR2 (11, 2)
SREBF1 (9, 1)
GATA2 (9, 1)
TFAP2A (20, 0)
USF1 (13, 1)
CTNNB1 (22, 5)
TP63 (9, 1)
IRF8 (9, 0)
SPI1 (47, 2)
NFATC1 (8, 0)
AHR (7, 0)
IRF1 (17, 1)
ELF1 (8, 0)
NFATC2 (9, 0)
STAT1 (27, 3)
PITX2 (7, 0)
ATF2 (11, 0)
NFKB1 (58, 4)
RELA (61, 4)
RELB (49, 3)
NFKB2 (50, 4)
REL (49, 3)
NFKB1_NFKB2 (48, 3)
STAT3 (39, 4)
MYC (36, 6)
WT1 (11, 2)
FOS (20, 0)
JUN (57, 3)
JUNB (43, 2)
JUND (44, 2)
FOS_JUN (43, 1)
VDR (13, 0)
CEBPB (35, 1)
RUNX1 (17, 1)
ESR1 (27, 6)
RARA (14, 2)
HNF4A (12, 0)
GATA4 (8, 0)
Transcription factor activity
3
1.5
0
−1.5
−3
Tissue
IDH–mut
IDH–wt
C
Enrichment score
FDR
HIF1A & MYC shared -0.40 7.95e-03
HIF1A -0.30 7.07e-04
MYC -0.30 1.07e-06
Running enrichment score
0.2
0.0
−0.2
−0.4
Log2 FC
8
4
0
−4
−8
5000
10000
15000
20000
Genes ordered by decreasing log2 FC

B

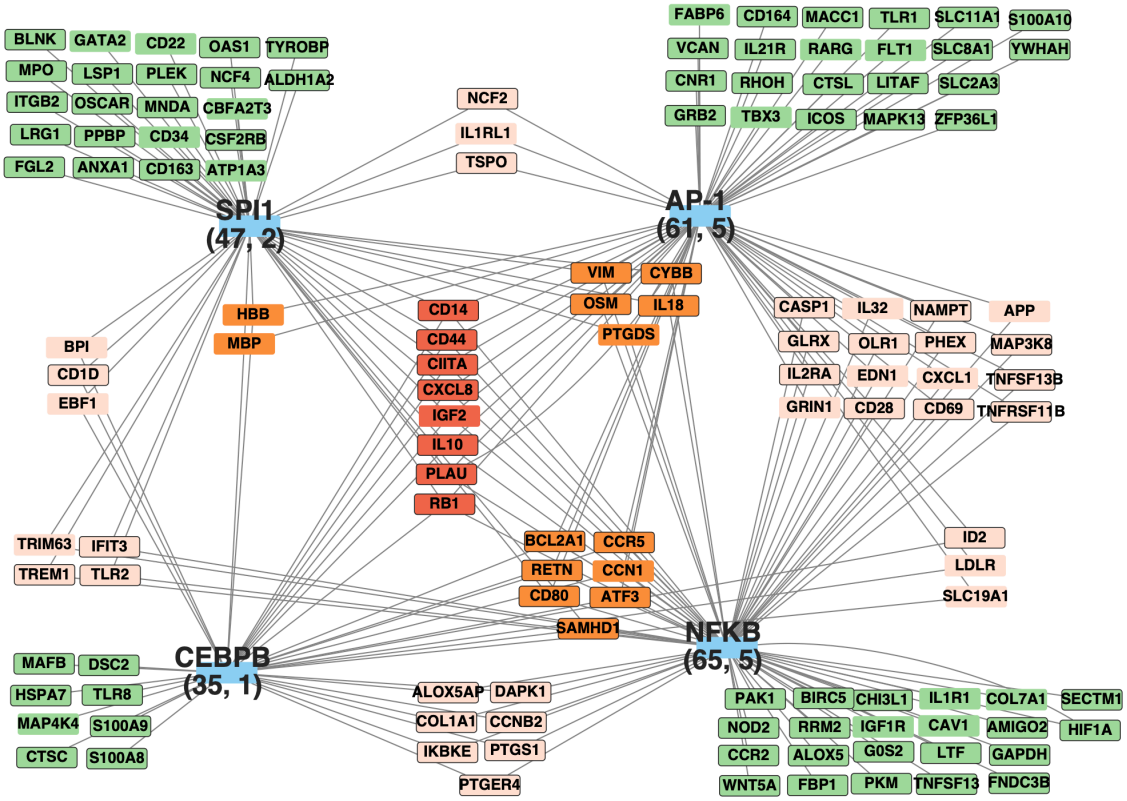
BLNK
GATA2
CD22
OAS1
TYROBP
MPO
LSP1
PLEK
NCF4
ALDH1A2
ITGB2
OSCAR
MNDA
CBFA2T3
LRG1
PPBP
CD34
CSF2RB
FGL2
ANXA1
CD163
ATP1A3
SPI1
(47, 2)
NCF2
IL1RL1
TSPO
FABP6
CD164
MACC1
TLR1
SLC11A1
S100A10
VCAN
IL21R
RARG
FLT1
SLC8A1
YWHAH
CNR1
RHOH
CTSL
LITAF
SLC2A3
GRB2
TBX3
ICOS
MAPK13
ZFP36L1
AP-1
(61, 5)
VIM
CYBB
OSM
IL18
PTGDS
HBB
MBP
CD14
CD44
CIITA
CXCL8
IGF2
IL10
PLAU
RB1
CASP1
IL32
NAMPT
APP
GLRX
OLR1
PHEX
MAP3K8
IL2RA
EDN1
CXCL1
TNFSF13B
GRIN1
CD28
CD69
TNFRSF11B
BPI
CD1D
EBF1
TRIM63
IFIT3
TREM1
TLR2
BCL2A1
CCR5
RETN
CCN1
CD80
ATF3
SAMHD1
ID2
LDLR
SLC19A1
MAFB
DSC2
HSPA7
TLR8
MAP4K4
S100A9
CTSC
S100A8
CEBPB
(35, 1)
ALOX5AP
DAPK1
COL1A1
CCNB2
IKBKE
PTGS1
PTGER4
NFKB
(65, 5)
PAK1
BIRC5
CHI3L1
IL1R1
COL7A1
SECTM1
NOD2
RRM2
IGF1R
CAV1
AMIGO2
HIF1A
CCR2
ALOX5
G0S2
LTF
GAPDH
WNT5A
FBP1
PKM
TNFSF13
FNDC3B

Figure 3. Gene regulatory network analysis reveals lower activity of core microglial TFs linked to hypermethylated enhancers in CD11B+ cells from IDH^{mut} gliomas. (A) The heatmap depicts TFs (n=45) exhibiting differential activity (FDR <0.05; Wilcoxon's test) in CD11B+ cells according to the IDH mutation status of corresponding tumors. The TFs targets used for this analysis, retrieved from the CollecTRI database were searched among the genes displaying upregulated/downregulated expression and hypermethylation at enhancers in myeloid cells from IDH^{mut} gliomas (quadrants I and IV, Fig. 2A). The number of targets regulated positively and negatively by each TF is indicated in brackets. Unsupervised clustering was performed using the z-scores of TF activity, where red and blue colors indicate high and low activity, respectively, and non-significant activity is colored in gray. **(B)** Gene regulatory network of four representative TFs (blue background) having lower activity in CD11B+ cells from IDH^{mut} compared to IDH^{wt} gliomas. TFs targets have a red, orange, pink or green background if they are controlled by four, three, two or one TF, respectively. Targets with or without black box come from quadrant I (hypermethylated enhancers and upregulated expression) or quadrant IV (hypermethylated enhancers and downregulated expression) of Fig. 2A, respectively. **(C)** Gene set enrichment analysis of positive gene targets of HIF1A, MYC (retrieved from CollecTRI database) and those in common between these TFs. Genes are ranked using log2 fold change from differential expression analysis of CD11B+ samples in human gliomas (IDH^{mut}, n=14 vs. IDH^{wt}, n=8).

Notably, shared targets of these TFs involved in glycolysis (CD44, ENO1, GAPDH, HIF1A, and ID2), as well as HIF1A targets involved in NADH regeneration and mitochondrial function (ENO2, NAMPT, PKM, PFKFB4, and SDHB), also appeared in the integrative gene list (Fig. 2C). These findings were validated using published RNA-seq data of microglia and MDMs from IDH^{mut} vs. IDH^{wt} gliomas, with the most significant differences observed in microglia compared to MDMs (Supplementary Fig. S5). Overall, these results highlight enhancers as the main targets of microenvironmental perturbations that affect microglial activation in IDH^{mut} gliomas, and raise important questions about the underlying mechanisms driving hypermethylation.

D-2HG inhibits TET-mediated 5mC oxidation and promotes DNA hypermethylation at lineage-specific enhancers in human microglia

We hypothesized that D-2HG, the oncometabolite produced by IDH^{mut} glioma cells and released into the TME, could impact the DNA methylome of CD11B+ cells. Ten-eleven translocation (TET) enzymes are α-KG-dependent dioxygenases that mediate the first step of active DNA demethylation by catalyzing the conversion of 5-methylcytosine (5mC) to 5-hydroxymethylcytosine (5hmC)[47] (Supplementary Fig. S6A). Inhibition of TET-mediated DNA demethylation by D-2HG results in decreased levels of 5hmC and increased levels of 5mC

after several rounds of cell replication, ultimately establishing the G-CIMP-high phenotype of IDH^{mut} gliomas[27,48]. To explore whether this mechanism is at play in the myeloid cells of these tumors, we analyzed global levels of 5hmC and 5mC, as well as the cumulative cell replication history, in an independent series of CD11B+ and CD11B- fractions isolated from human gliomas and normal tissues used as controls (Supplementary Fig. S6B and S6C). We confirmed a higher 5mC/5hmC ratio in CD11B- cells of IDH^{mut} gliomas than in non-tumor tissues (Supplementary Fig. S6B). Remarkably, a significant increase in the 5mC/5hmC ratio was also observed in the corresponding myeloid cells, along with a higher cumulative number of cell divisions, as indicated by epigenetic clock analysis (Supplementary Fig. S6C). These results suggest that TET inhibition contributes to the global DNA hypermethylation observed in myeloid cells, most likely microglia, from IDH^{mut} gliomas.

To ascertain the effect of D-2HG on TET-mediated DNA demethylation in human microglia, we established primary cultures from tissue aspirates of patients who underwent surgery for glioma or drug-resistant epilepsy (Fig. 4A). Microglial cells maintained in serum-free defined culture medium[49] are viable for up to 15 days. Over 95% of these cells expressed the markers ionized calcium-binding adapter molecule 1 (IBA1) and transmembrane protein 119 (TMEM119) (Fig. 4B), while less than 5% of the cells were proliferating (KI67+) (not shown). Furthermore, these cells maintained a stable RNA-seq microglial signature over time (Supplementary Fig. S7A) and were functional, as evidenced by the proinflammatory response upon lipopolysaccharide (LPS) stimulation at 48 h or 14 days (Supplementary Fig. S7B and S7C). To evaluate the uptake of D-2HG by human microglial cells, we measured intracellular levels after 48 h of treatment at a concentration estimated to occur in the TME[4,5], which does not affect cell viability. We found that the levels of D-2HG reached by microglial cells were comparable to those observed in *bona fide* IDH^{mut} cells (Supplementary Fig. S8A and S8B; Fig. 4C) and were sufficient to induce a significant decrease in TET enzymatic activity (Fig. 4D; Supplementary Fig. S8C). We then exposed primary microglial cultures to D-2HG for a prolonged period and observed opposite trends in the global levels of 5hmC over time

between treated and control microglia, resulting in a significant decrease in 5hmC levels in treated cells at 14 days (Fig. 4E; Supplementary Fig. S8D).

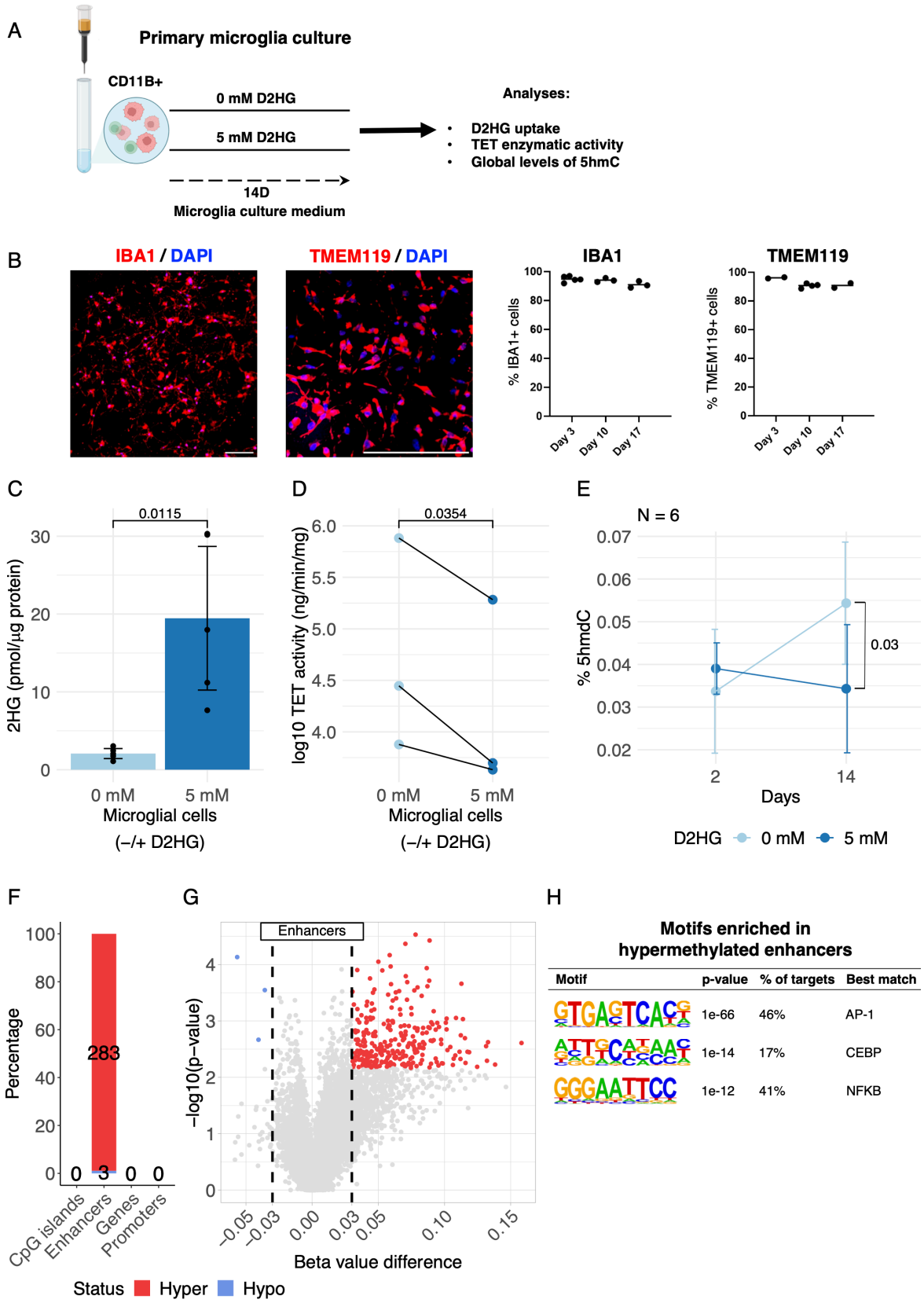

Figure 4. D-2HG uptake by human primary microglial cells inhibits TET function. (A) Overview of the experimental workflow for establishing primary microglia cultures treated with D-2HG, and analyses assessing the inhibition of TET-mediated DNA demethylation. The tissue collection procedures and culture conditions are thoroughly detailed in the Methods section. **(B)** Representative immunofluorescence images show the preserved expression of microglial markers TMEM119 (confocal microscopy) and IBA1 (Apotome) in primary cells at 12 days in culture (scale bars: 100 µm). Estimated percentages of TMEM119+ and IBA1+ cells in primary cultures at different time points are indicated on the right. **(C)** The quantification of intracellular levels of 2HG was determined using LC/MS in primary human microglia obtained from five surgical aspirates with IDH^{wt} (n=2) or IDH^{mut} (n=3) status. Data are represented as the mean with a 95% CI; p-value was calculated using a one-sided paired t-test. **(D)** TET enzymatic activity measured as detection of hydroxymethylated product (ng) after 1-hour incubation of the substrate with protein extracts from microglia untreated and treated with 5 mM D-2HG over 48 h. Primary cultures were generated from surgical aspirates with IDH^{wt} status (n=3). The p-value was calculated using one-sided paired t-test. **(E)** Assessment of global levels of 5hmC, determined by LC-MS/MS, in primary human microglia obtained from six surgical aspirates with IDH^{wt} (n=5) or IDH^{mut} (n=1) status after 48 h and 14 days of treatment with 5 mM D-2HG (added every 2-3 days). Data are represented as the mean with a 95% CI; p-value was calculated using a one-sided paired t-test. **(F)** DNA methylation profiling of primary microglia was conducted with EPIC array. Stacked bar chart shows absolute numbers and relative percentages of functional genomic regions respect to the methylation status (absolute $\Delta\beta > 0.03$, FDR < 0.25) in D-2HG treated vs. untreated primary microglia cultured for 14 days. Samples were obtained from eight surgical aspirates with IDH^{wt} (n=5) or IDH^{mut} (n=3) status. **(G)** Volcano plot illustrates the magnitude and extent of differentially methylated enhancers in D-2HG treated vs. untreated primary microglia. **(H)** Motif enrichment analysis of hypermethylated enhancers in D-2HG-treated primary microglia. Significant sequence motifs (ranked by p-value) were determined using HOMER.

However, in contrast to the *ex vivo* context, no concomitant increase in 5mC levels was observed in D-2HG-treated microglia (data not shown). This suggested a passive demethylation mechanism in low-proliferating microglia *in vitro*. Nonetheless, analysis of the DNA methylome in microglial cells treated with D-2HG for 14 days, using the same EPIC array applied to *ex vivo* CD11B+ cells in gliomas, revealed subtle but reproducible hypermethylation at 283 enhancers (absolute $\Delta\beta > 0.03$, FDR < 0.25) (Fig. 4F and 4G). Importantly, these enhancers showed significant enrichment for motifs of lineage-determining and stimulus-responsive TFs, similar to the *ex vivo* study, including AP-1, C/EBP and NF-κβ, but not SPI1 (PU.1) (Fig. 4H).

Although EPIC arrays offer sufficient coverage of enhancers, only a single probe can capture methylation changes across an enhancer region[50]. Moreover, this profiling method does not

discriminate between 5hmC and 5mC, which could provide valuable insights into impaired TET function. Considering the high turnover of DNA methylation at enhancers, which relies on TET activity rather than replicative passive dilution of 5mC[51], we wondered whether D-2HG affects TET-mediated demethylation at enhancers across the genome. To investigate this possibility, we performed DNA methylome and hydroxymethylome profiling of microglial cells treated with D-2HG for 48 h and 14 days. For this experiment, we used microglial preparations from normal brain tissues of three individuals with drug-resistant epilepsy to exclude tumor influences other than released D-2HG, and we applied a reduced representation and non-bisulfite sequencing approach[52]. This method enables a more confident assessment of 5mCG and 5hmCG levels in enhancers, albeit only across 20% of the enhancers analyzed with EPIC array, which covers ~58% of FANTOM-annotated enhancers[50]. Changes in 5mCG and 5hmCG levels within the full-length sequences of enhancer elements were most evident after 14 days of treatment compared to 48 h, with a marked difference observed for 5hmCG, reflecting its accumulation over time in D-2HG-treated cells (Fig. 5A). This result indicates that D-2HG-related changes in genomic 5hmC content, initially detected by LC-MS/MS, mostly occur in non-CpG contexts and/or repeated sequences. It also shows that TET function along the entire enhancer region is not affected, at least *in vitro*. While EPIC arrays revealed some lineage-specific enhancers that underwent hypermethylation following D-2HG treatment (Fig. 4F-H), only a few of them were covered by the reduced representation sequencing approach.

To ascertain whether inhibition of TET-mediated demethylation by D-2HG affected a subset of lineage-specific enhancers, we pursued the following analytical strategy using our sequencing data (Fig. 5B). We aimed to use as ground truth the enhancers in CD11B+ cells from normal brain tissue that were hypermethylated in myeloid cells from IDH^{mut} gliomas, likely corresponding to microglia (Fig. 1C). Given that TET activity is highest near TF-binding motifs in enhancers[51,53], we focused our analysis on TF-binding motifs located in hypermethylated enhancers from both CD11B+ cells in IDH^{mut} gliomas (Fig. 1F) and D-2HG-

treated microglia (Fig. 4H), as hypermethylation in these regions could impair TF occupancy (Fig. 3A and 3B).

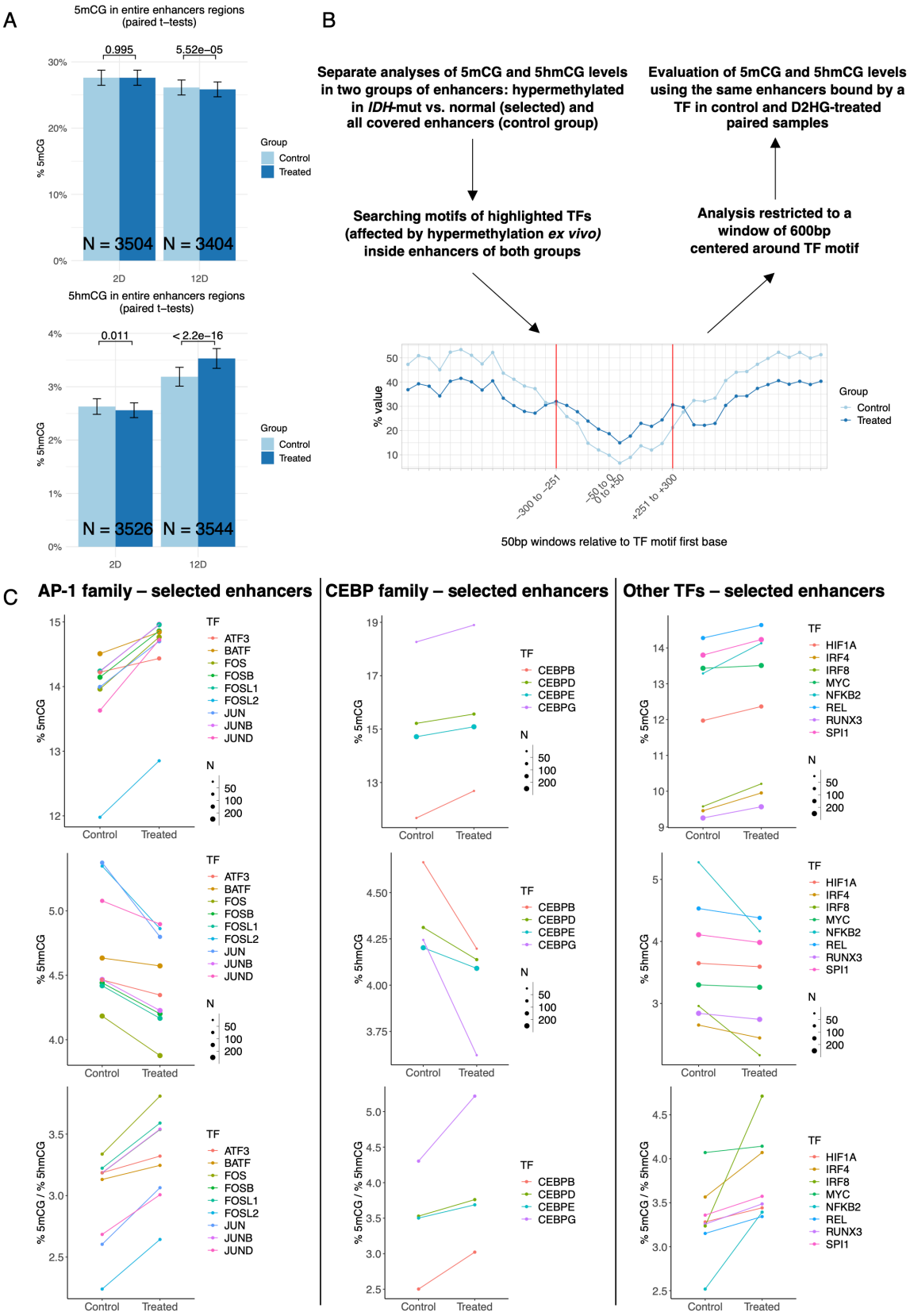

Figure 5. Reduced representation non-bisulfite sequencing reveals high 5mCG/5hmCG ratios at lineage-specific enhancers in D-2HG-treated primary microglia. (A) Bar plots show the percentages of 5mCG and 5hmCG in the full-length sequences of covered enhancers in primary human microglia treated with D-2HG for 48 h or 14 days and in paired untreated controls. The number of paired enhancers for each comparison is indicated. Only common enhancers across patients were analyzed. **(B)** Workflow analysis of 5mCG and 5hmCG levels quantification in defined windows around TFs binding motifs, located in lineage-specific enhancers, in D-2HG-treated microglia for 14 days and in paired untreated controls. **C)** Plots showing a separate analysis of 5mCG and 5hmC percentages (upper) around TFs binding motifs for the indicated TFs in D-2HG-treated microglia and paired untreated controls. Only common enhancers across patients were analyzed. The size of each dot indicates the number of enhancers analyzed in a paired manner between conditions. The 5mCG/5hmCG ratios (bottom), which are higher in D-2HG-treated microglia than in paired controls, are also shown. The TFs binding motifs for this analysis are located in enhancers exhibiting hypermethylation in CD11B+ cells from IDH^{mut} gliomas vs. normal brain tissues in the *ex vivo* study (Fig. 1C).

Remarkably, higher 5mCG/5hmCG ratios were detected around TF-binding motifs of members of the AP-1, C/EBP, and NF-κβ TFs families in D-2HG-treated primary microglia than in paired untreated controls (Fig. 5C), in line with motifs enriched in hypermethylated enhancers of CD11B+ cells from IDH^{mut} gliomas vs. normal brain tissue (Fig. 1F). Similar results were obtained when this analysis was extended to SPI1 (PU.1), IRF4/8, RUNX3, HIF1A, and MYC motifs (Fig. 5C), which also appeared to be relevant in the *ex vivo* context. In sharp contrast, 5mCG and 5hmCG levels in the proximity of TF-binding motifs located in the entire set of covered enhancers exhibited opposite trends (Supplementary Fig. 9A). Furthermore, among the genes regulated by selected enhancers exhibiting both hypermethylation and hypohydroxymethylation (Fig. 5C), we observed an enrichment of downregulated genes, suggesting a direct impact of D-2HG-induced hypermethylation on gene expression (Supplementary Fig. 9B; Supplementary Table S5). Collectively, these results strongly support the idea that D-2HG impedes TET-mediated DNA demethylation at lineage-specific enhancers, leading to a blunted microglial cell response.

D-2HG dampens the LPS-induced inflammatory response and increases basal oxidative metabolism in human microglial cells

Lineage-specific enhancers that were affected by D-2HG treatment in our *in vitro* experiments are known to be transcribed upon macrophage stimulation[54]. Therefore, we

hypothesized that the methylome primed by D-2HG could hinder the activation of enhancers that regulate the proinflammatory capacity of human microglia. To address this issue, we evaluated transcriptional changes in cells pretreated with D-2HG for 14 days and subsequently challenged with LPS for 6 h (Fig. 6A).

Gene set enrichment analysis (GSEA) indicated that D-2HG treatment attenuated LPS-induced microglial activation (Fig. 6B). Specifically, these cells exhibited an M2-like phenotype characterized by enhanced OXPHOS and fatty acid metabolism, coupled with notable suppression of inflammatory response pathways, such as TNF-α signaling via NF-κβ (Fig. 6B). In addition, RNA-seq data from our *ex vivo* study showed reduced expression of proinflammatory cytokines in CD11B+ cells from IDH^{mut} compared to those from IDH^{wt} gliomas (Supplementary Fig. S10A). We then evaluated the effect of D-2HG on the expression of LPS-induced cytokines using RT-qPCR in an independent series of primary microglial preparations. We confirmed that D-2HG abrogated the expression of TNFA and IL6 in LPS-challenged cells compared to paired controls (p-value=0.02 and 0.07, respectively) (Supplementary Fig. S10B). Similarly, assessment of mitochondrial respiration parameters demonstrated that D-2HG-treated microglia exhibited an increase in basal and maximal respiration, even after LPS stimulation (Supplementary Fig. S10C). This observation suggests that this oncometabolite impedes the glycolytic shift that accompanies cellular activation, and instead favors OXPHOS metabolism. Taken together, these results indicate that D-2HG dampens the microglial proinflammatory response to LPS, likely through direct effects on TET-mediated demethylation at enhancers governing microglial activation.

Finally, to determine whether suppressed microglial cell signaling linked to D-2HG-driven enhancer hypermethylation can be restored by targeted therapy, we analyzed microglial cells from single-nucleus RNA-seq (snRNA-seq) data obtained from an oligodendroglioma patient treated with ivosidenib, an inhibitor of the IDH1 mutant enzyme that reduces D-2HG levels in tumor bulk (Fig. 6C; Supplementary Table S1)[55].

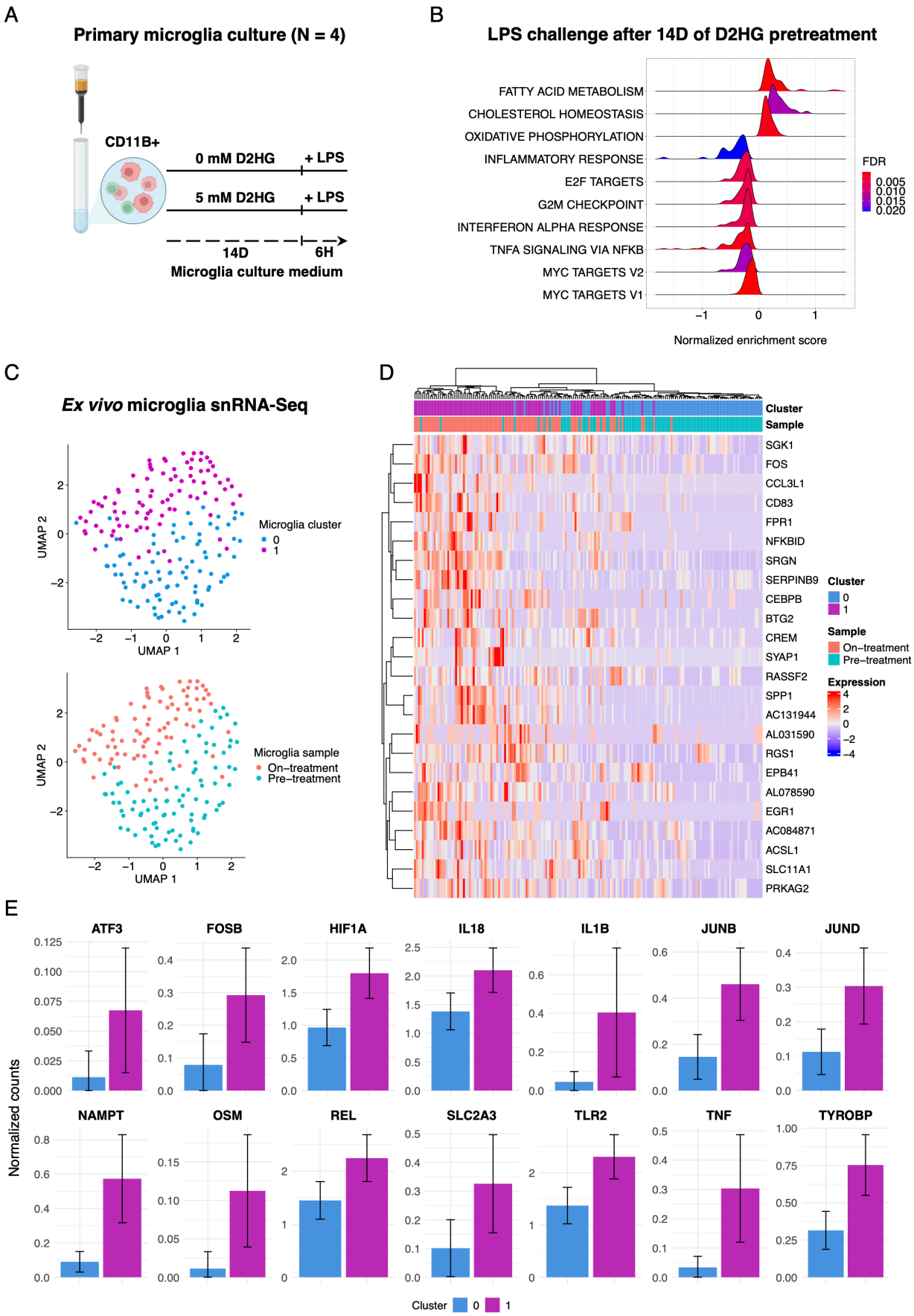
A
Primary microglia culture (N = 4)
CD11B+
0 mM D2HG
+ LPS
5 mM D2HG
+ LPS
14D
6H
Microglia culture medium
B
LPS challenge after 14D of D2HG pretreatment
FATTY ACID METABOLISM
CHOLESTEROL HOMEOSTASIS
OXIDATIVE PHOSPHORYLATION
INFLAMMATORY RESPONSE
E2F TARGETS
G2M CHECKPOINT
INTERFERON ALPHA RESPONSE
TNFA SIGNALING VIA NFKB
MYC TARGETS V2
MYC TARGETS V1
FDR
0.005
0.010
0.015
0.020
Normalized enrichment score
C
Ex vivo microglia snRNA-Seq
UMAP 2
UMAP 1
Microglia cluster
0
1
Microglia sample
On−treatment
Pre−treatment
D
Cluster
Sample
SGK1
FOS
CCL3L1
CD83
FPR1
NFKBID
SRGN
SERPINB9
CEBPB
BTG2
CREM
SYAP1
RASSF2
SPP1
AC131944
AL031590
RGS1
EPB41
AL078590
EGR1
AC084871
ACSL1
SLC11A1
PRKAG2
Cluster
0
1
Sample
On−treatment
Pre−treatment
Expression
E
ATF3
FOSB
HIF1A
IL18
IL1B
JUNB
JUND
NAMPT
OSM
REL
SLC2A3
TLR2
TNF
TYROBP
Normalized counts
Cluster 0 1

Figure 6. D-2HG impairs microglial activation. (A) Experimental workflow for the LPS challenge experiment in primary microglia pre-treated with D-2HG for 14 days. RNA-seq data was generated from human primary microglia obtained from four surgical aspirates with IDH^{wt} (n=3) or IDH^{mut} (n=1) status. Patient-paired approach was adopted for RNA-seq data analysis. **(B)** GSEA ridge plot illustrates "hallmark gene sets" in D-2HG-treated microglia for 14 days, 6 h after LPS stimulation. Gene sets with positive or negative normalized enrichment score are associated with up or down regulated genes, respectively (FDR < 0.05). **(C)** Uniform Manifold Approximation and Projection (UMAP) plots depict microglial cells analyzed with snRNA-seq from one oligodendroglioma patient pre- and on-treatment with the mutant IDH inhibitor ivosidenib. **(D)** The heatmap illustrates the significantly upregulated genes (log2FC > 1, Bonferroni-adjusted p-value < 0.05) in microglia upon ivosidenib treatment. **(E)** Normalized counts of selected genes in microglia pre and on-treatment. Data are represented as the mean with a 95% CI.

After removing low-quality cells, 178 microglial cells remained, as determined by the high expression of the markers TAL1 and SLC2A5 and the low/absence of expression of the MDMs markers CD163 and TGFBI. These cells encompassed two well-defined clusters corresponding almost entirely to on- (n=87) and pre-treatment (n=91) microglia, on which the analysis was focused (Fig. 6C). We noticed a transcriptional shift towards gene upregulation in cluster 1 (on-treatment) compared to cluster 2 (pre-treatment) (1683 genes with log2FC >1 and 501 genes with log2FC < -1, respectively). Furthermore, we found 24 upregulated genes (including the master regulators TFs FOS and CEBPB) (Fig. 6D) and three downregulated genes (Bonferroni-adjusted p-value < 0.05, log2FC > 1 or < -1, respectively) with a strong enrichment of the upregulated genes in TNF-α signaling via the NF-κβ gene set (FDR=1.5e-4; ORA). Additionally, microglial cells in cluster 1 displayed overexpression of other TFs governing activation, including AP-1 family members (FOSB, ATF3, JUNB, and JUND), REL, and HIF1A, as well as related target genes highlighted in the *ex vivo* and *in vitro* analyses, such as OSM, IL18, IL1B, FPR1, TLR2, NAMPT, TNF, TYROBP, and SLC2A3 (GLUT-3) (Fig. 6D and 6E). This result suggests that decreased levels of D-2HG in the TME may reverse the hypermethylation phenotype observed in microglia isolated from IDH^{mut} gliomas, thereby enabling their activation. Supporting this hypothesis, a significant proportion of genes upregulated following ivosidenib treatment are regulated by enhancers that were hypermethylated in CD11B+ cells from IDH^{mut} gliomas (p = 0.0012, ORA).

Discussion

The development of new therapeutic options to cure glioma requires a deep understanding of the epigenetic mechanisms governing the transcriptional programs, cell states, and proinflammatory capacities of TAMs. Differences in transcriptome and chromatin landscapes of these cells have been associated with the IDH status of tumors[17,18,21], but the extent and role of DNA methylation have remained uncharacterized. Herein, through genome-wide profiling of the DNA methylome, we uncovered global and differential distributions of 5mC and 5hmC changes in TAMs from IDH^{mut} gliomas. Our findings reveal how differential methylation affects microglial enhancers involved in the regulation of proinflammatory and metabolic pathways.

We found that CD11B+ cells residing in an IDH^{mut} environment displayed a striking bias towards DNA hypermethylation. TAMs comprise MDMs and microglia in proportions and states of activation that differ according to glioma IDH^{mut} status, subtype, and grade[17-23]. Previous studies have reported that most TAMs in IDH^{mut} tumors are microglia, whereas IDH^{wt} gliomas are marked by an influx of MDMs[17-20]. In this regard, we cannot rule out the possibility that differentially methylated changes observed in CD11B+ cells partly reflect a decreased recruitment of MDMs in IDH^{mut} tumors compared to IDH^{wt} tumors. However, the hypermethylation we observed holds true even when comparing CD11B+ cells from IDH^{mut} gliomas to non-tumor brain tissues, both of which are highly enriched in microglia. In addition, a recent study indicated that immunomodulatory activity programs are expressed across myeloid cell types and demonstrated convergent phenotypes of resident microglia and infiltrating MDMs, with the latter acquiring a microglia-like phenotype in tumors[23]. Moreover, mouse studies have indicated that MDMs can adopt a DNA methylation profile very similar to that of microglia after colonizing the central nervous system niche[56]. Therefore, our bulk profiling of CD11B+ cells strongly suggests that microglia undergo a hypermethylated state in IDH^{mut} tumors. This assumption was further substantiated by our analyses of methylation across gene regulatory regions, which revealed functional implications related to proinflammatory activation and metabolism in microglia.

We highlighted that the occurrence and extent of differentially methylated changes were more prominent in distal enhancers. DNA methylation at CpG sites within or flanking motifs may prevent TF binding to regulatory regions by inducing steric hindrance, altering DNA shape and rigidity, or influencing nucleosome positioning, thereby affecting the formation of active chromatin[36,38,43,57-59]. A recent study showed that only a minority of enhancers in a given cell type are sensitive to DNA methylation[60]. In line with this, our integrative analysis of methylome and transcriptome changes demonstrated that among the hypermethylated enhancers displayed by CD11B+ cells from the IDH^{mut} vs. IDH^{wt} comparison, 23% may account for the downregulated expression of target genes. We also observed that hypermethylated enhancers were enriched for motifs of lineage-determining TFs, including SPI1 (PU.1) and members of the C/EBP and RUNX families, as well as motifs of stimulus-induced TFs such as AP-1, IRF, and NF-κB. These TFs regulate the functional properties of myeloid cells. Our investigation of gene regulatory networks further supports the hypothesis that hypermethylated enhancers are responsible for the reduced activity of core TFs that govern the identity and activation of human microglial cells[39]. Specifically, hypermethylation seems to disrupt cooperative regulatory functions involving lineage-determining TFs SPI1 (PU.1) and C/EBP, and stimulus-responsive TFs AP-1 and NF-κβ, which in turn affect the expression of key genes involved in inflammatory responses. Hypermethylated enhancers also appear to influence the expression of activating receptors as well as genes involved in antigen presentation, an observation previously reported in bulk methylome analysis of IDH^{mut} gliomas[61]. These findings indicate that microglia in these tumors undergo a profound alteration of the promoter-enhancer interactions that characterize these cells[62].

In addition to microglial TFs, our data revealed reduced activation of HIF1A and MYC, which may reinforce the silencing of shared targets essential for the glycolytic shift of stimulated macrophages[63-66]. Along with a marked downregulation of several target genes, there was low expression of HIF1A, accompanied by hypermethylation at the regulatory regions of HIF1A and some of its targets. In particular, reduced expression of HIF1A targets, such as LDHA, ENO1, HK2, PKM, VIM, ITGB2, and PGK1, has also been reported in bulk IDH^{mut} tumors

and/or cells[67], which may be attributable to hypermethylation driving the silencing of these genes, in addition to the effect of D-2HG on HIF-1α protein destabilization[68]. Collectively, our findings provide evidence that DNA hypermethylation may contribute to a reduced proinflammatory microglial response by targeting enhancers that orchestrate synergistic responses to environmental stimuli that drive myeloid cell activation[69-71]. This assumption is supported by our experiments, which demonstrated how oncometabolite signaling modulates the methylome and subsequently affects the activation of human microglia.

Our analysis of single-nucleus RNA sequencing data from two paired oligodendroglioma samples revealed that treatment with an inhibitor of the IDH1 mutant enzyme could unleash the signaling that suppresses microglial activation. This observation supports the notion that D-2HG production plays a major role in suppressive signaling that affects microglial function, and highlights the prognostic and therapeutic value of microglial activation in IDH^{mut} gliomas. By establishing primary cultures of human microglia, we showed that D-2HG is taken up by these cells, inhibits TET-mediated DNA demethylation, and hampers the accumulation of 5hmC after 14 days of treatment. Although D-2HG-driven global hypermethylation is challenging to reproduce in our microglial cultures, our analysis of the methylome and hydroxymethylome at nucleotide resolution clearly demonstrated higher 5mCG/5hmCG ratios in lineage-specific enhancers that were also hypermethylated in *ex vivo* CD11B+ cells from IDH^{mut} gliomas. This result is consistent with previous reports showing that the highest TET activity is localized to enhancer elements[51,53]. Our observation that 5hmC turnover is limited in cultures of non-proliferating microglial cells points to a passive demethylation mechanism that can unfold under successive rounds of replication. Nevertheless, a comprehensive characterization of other TET-mediated oxidized derivatives, such as 5fC and 5caC, and an assessment of the activity and role of thymidine DNA glycosylase[47] are required to determine the relative contribution of active vs. passive demethylation mechanisms in human microglia.

Regardless of the demethylation mechanism, we speculate that inhibition of TET2 in slowly proliferating microglial cells of IDH^{mut} gliomas, which have been exposed to D-2HG for several years, may lead to full-blown hypermethylation, as opposed to the limited changes observed in our non-proliferating microglial cultures exposed to this oncometabolite for no more than two weeks. It is also possible that additional mechanisms contribute to hypermethylation highlighted in the *ex vivo* context. Nevertheless, our *in vitro* system was instrumental in demonstrating that D-2HG readily affects TET-mediated demethylation at specific enhancers, leading to suppressed expression of targeted genes. High turnover of DNA methylation at enhancers is crucial for cellular plasticity, differentiation, and responsiveness to environmental changes, such as during macrophage activation[72,73]. Thus, the significant overlap of enhancer elements affected by D-2HG *in vitro* with those exhibiting hypermethylation in myeloid cells from IDH^{mut} gliomas strongly suggests that the methylome of microglial cells primed by D-2HG negatively affects the transcriptional response to inflammatory stimuli.

Consistent with this hypothesis, we observed that D-2HG-treated microglia challenged with LPS displayed attenuation of the inflammatory response while favoring OXPHOS metabolism, which marks anti-inflammatory M2-like macrophage phenotypes[74,75]. While the hypermethylation we observed may affect the glycolytic shift—a metabolic response documented in iPSC-derived human microglia treated with LPS[76]— our data indicate that hypermethylation could also affect the expression of genes involved in cytokine production. Considering the time-dependent effects of D-2HG on the microglia methylome, we propose that an epigenetic drift, involving the selection of hypermethylated enhancers over time, underlies the silencing of master regulators, which impedes not only the proinflammatory response but also glycolytic reprogramming, both of which are essential for microglial cell activation. This does not exclude the possibility of contributions from chromatin remodeling and non-epigenetic mechanisms to LPS hyporesponsiveness of D-2HG-treated microglia, including signaling pathways targeted by D-2HG in other cell types[6,9,10,77]. In particular, it has been reported that acute octyl-D-2HG treatment can dampen LPS-triggered cytokine

expression in immortalized mouse microglial cells through a mechanism involving AMP-activated protein kinase (AMPK)-mTOR-mediated reduction of NF-κB activity[77]. Whether this mechanism also applies to human primary microglia remains undetermined.

In conclusion, we provide evidence that D-2HG reshapes the enhancer landscape of resident microglia in IDH^{mut} gliomas, thus impairing the regulatory function of core TFs. This priming mechanism precludes the capacity of these cells to mount the inflammatory response and possibly the shift towards glycolytic metabolism. We speculate that D-2HG effects on myeloid cells promote a cold immune TME that favors tumor progression. Given that the reduced concentration of D-2HG in bulk tumors induced by inhibitors of the IDH mutant enzyme is associated with inflammatory and metabolic changes[78], it is important to evaluate the extent of these effects in myeloid cells and correlate them with the clinical response to this therapeutic option.

Limitations of the study

We acknowledge certain limitations in our study that should be taken into consideration. Our comparative analyses of CD11B+ myeloid fractions from gliomas and non-tumor tissues remained at the bulk level. Moreover, methylome profiling is limited to CpG residues in the EPIC array and to global levels assessed by LC-MS/MS, whereas no exhaustive analysis of 5hmC at nucleotide resolution has been conducted *ex vivo*. While our results indicate that hypermethylation affects the dominant population of resident microglial cells in IDH^{mut} gliomas, employing single-cell multimodal approaches will be necessary to better associate enhancer landscapes with their regulatory roles in specific myeloid cell subsets/states. Finally, we did not analyze the potential effects of D-2HG on the local chromatin environment, which could also influence enhancer function.

Author's Disclosures

L.A.S. is a scientific advisor and co-founder of Cellintec L.L.C., which had no role in this research. M.L.S. is an equity holder, scientific co-founder, and advisory board member of Immunitas Therapeutics. The other authors declare no competing financial interests.

Author's Contributions

A.L: Conceptualization, optimization of primary microglial cultures, design and performance *in vitro* experiments, data collection, analysis and interpretation of results, and draft editing. P.P: Conceptualization, data curation, computational and statistical analyses, interpretation of results, data visualization, and draft editing. B.M: Provided tissues from surgical resections, optimized primary microglial cultures, and draft editing. Q.R. and S.J: Performed *ex vivo* experiments and data visualization. Y.H. and S.S: Conducted validation experiments, data analysis and interpretation, data visualization, and draft editing. P. M.: Provided tissues from surgical resections. K.L. and A.A: Bioinformatics assistance and draft editing. M.V., A.I., C.B., E.H., N.P., K.M., S.T., M.L.S., M.T., and F.B: Provided material and data curation. A.D., I.F: Performed LC/MS analysis of 2HG. G.A.K., P.J.K., L.J.M: Performed LC-MS/MS and data analysis of global 5mC and 5hmC levels. E.D. and E.E-H: Performed seahorse experiments and data analysis. L.A.S: Analysis of epigenetic clock and draft editing. A.I: Data analysis, interpretation, and draft editing. M.C: Computational analyses and draft editing. M.M: Conceptualization, experimental design, data analysis and interpretation, and draft editing. M.S: Conceptualization, experimental design, data analysis and interpretation, draft editing, funding acquisition, supervision. L.J.C-V: Conceptualization, experimental design, data analysis and interpretation, data visualization, writing of the original draft, funding acquisition, project administration, and supervision. All the authors critically revised the manuscript for important intellectual content and approved it for publication.

Acknowledgements

The authors express their deepest gratitude to Prof. Dr. Laurent Capelle for his insightful feedback and invaluable contributions to the collection of neurosurgical specimens for research purposes, including this study. The authors also thank the personnel working at the

ICM platforms iGenSeq (sequencing), Celis (cell culture), and Histomics (histology) for their technical support, and Julie Jardon, Coralie Gimonnet, and Giovanni Scala for their assistance with experiments and bioinformatics. This work is supported by the Ligue Nationale contre le Cancer (Équipe Labellisée), as well as by the following grants: INCa-DGOS-Inserm 12560, Site de Recherche Intégré sur le Cancer (SiRIC CURAMUS), French National Cancer Institute (INCa-PLBIO22-243), Fondation Bristol Myers Squibb pour la Recherche en Immuno-Oncologie (BMS 2104009NA), French National Cancer Institute (INCa), Fondation ARC and Ligue National contre le cancer (LNCC) grant (PAIR TUMC21-001, INCa-16280), and Entreprises contre le Cancer Paris-Île-de-France (GEFLUC R20202DD). A.L. is supported by a Fondation Recherche Médicale (FRM) scholarship, Q.R. is supported by a French Ministry of Education and Research scholarship, and Y.H. is supported by a La Ligue Nationale contre le Cancer scholarship.

Methods

Tumor samples and CD11B sorting

Human brain tissues were obtained with informed consent approved by the Institutional Ethical Committee Board in accordance with the Declaration of Helsinki. Samples for analyses were selected from the Pitié-Salpêtrière tumor bank Onconeurotek based on clinical information and validation by expert neuropathologists (K.M., S.T., F.B) of both histological features and molecular diagnosis as previously described[79]. Cryopreservation was performed as follows: tumors taken from the neurosurgery room were immediately transported on ice in HBSS (Gibco), cut into 2-5 mm diameter pieces, and submerged in cryotubes containing 1 mL of DMEM/F-12 (Gibco), 20% FBS, and 10% DMSO (Sigma-Aldrich). The cryotubes were placed at -80°C in alcohol-free freezing containers (Corning® CoolCell®). Cryopreserved samples were stored in liquid nitrogen until use. On the day of analysis, the tumor pieces were thawed and rinsed in DMEM/F-12. Next, the tissue was enzymatically and mechanically digested for 5-10 minutes at 37°C in HBSS-papain-based lysis buffer (Worthington) containing DNAse (0.01%, Worthington) and L-cysteine (124 µg/mL, Sigma). Enzymatic

digestion was stopped with ovomucoid (700 µg/mL; Worthington). The homogenates were sequentially filtered using 100 µm, 70 µm, and 30 µm SmartStrainers (Miltenyi) to remove residual clumps. HBSS was added, and samples were then centrifuged at 300 × g for 10 min at 4°C. Cell pellets were resuspended in an appropriate volume of cold MACS debris removal solution according to the manufacturer's instructions (Miltenyi). The suspension was gently mixed by pipetting 10-12 times, and ice-cold DPBS without calcium or magnesium was added slowly above the cell suspension to create a transparent gradient. The suspension was centrifuged at 3000 g for 10 min at 4 °C. After centrifugation, the top liquid and solid phases were discarded, and the cell suspensions were resuspended in cold MACS Buffer (0,5% BSA and 2 mM EDTA in PBS). The tubes were gently inverted 3-5 times and then centrifuged at 1000 g for 10 min at 4°C. After centrifugation, the supernatant was completely removed and red blood cell lysis was performed using ACK buffer (Gibco) for 5 min at room temperature. Next, the cells were centrifuged at 4°C and pellets were washed with cold DPBS. After centrifugation, cells were resuspended in MACS buffer and counted. Next, the cell pellets were labeled with an appropriate volume of CD11B MicroBeads (Miltenyi) in MACS buffer and incubated for 15 min at 4°C. Subsequently, the cells were resuspended in cold MACS buffer and centrifuged at 300 g for 10 min at 4°C. The supernatant was aspirated, and the cells were resuspended in cold MACS buffer. The LS MACS Separation Columns were placed in the magnetic field of a suitable MACS Separator, and the cell suspension was applied to the columns. The CD11B+ and CD11B- fractions were collected separately on ice. The dry pellets were stored at -80°C until nucleic acid extraction.

Nucleic acids extractions

RNA and DNA from CD11B+ and CD11B- samples were co-eluted using the AllPrep DNA/RNA Micro Kit (Qiagen, 80284) or AllPrep DNA/RNA Mini Kit (Qiagen, 80204), following the manufacturer’s instructions. In some cases, nucleic acids were purified separately using the Maxwell RSC simplyRNA Cells Kit (Promega, AS 1390) and Maxwell RSC Blood DNA Kit (Promega, AS 1400) following the manufacturer’s instructions. The yield and quality of total RNA were assessed using a Tapestation 2200 (Agilent) instrument.

Digital droplet PCR

IDH1 R132H, TERT C228T, and TERT C250T mutations were analyzed in the CD11B+ and CD11B- fractions from human gliomas using ddPCR. Droplet generation and partitioning were performed using the Bio-Rad system QX200. Primer sets, probes, and ddPCR Supermix for Probes (No dUTP) were used to quantify the absolute copy number in 3 ng of input DNA following the manufacturer's instructions. All the primers and probes were obtained from Bio-Rad Laboratories. Sequence information is available at www.bio-rad.com using the ID numbers: IDH1 p.R132H Hsa, Human (Ref: 10031246 UniqueAssayID: dHsaCP2000055), IDH1 WT for p.R132H Hsa, Human (Ref: 10031249 UniqueAssayID: dHsaCP2000056), TERT C228T_113 Hsa, Human (Ref: 12009308 UniqueAssayID: dHsaEXD72405942), TERT C250T_113 Hsa, Human (Ref: 12003908 UniqueAssayID: dHsaEXD46675715). The data were analyzed using Poisson statistics to determine the target DNA template concentration in the original sample. Positive controls consisted of tumor DNA from the CD11B- fractions, and negative controls contained water instead of DNA.

DNA methylation profiling

Genomic DNA was quantified using the Quant-iT dsDNA Broad Range Assay (Thermo Fisher Scientific, Waltham, MA, USA) on a Tecan SPARK microplate reader (TECAN, Switzerland). Total DNA (500 ng) from each sample was sodium bisulfite-converted using the Zymo EZ-96 DNA Methylation kit following the manufacturer's recommendations for the Infinium assay (Zymo Research, catalog number: D5004). After conversion, the DNA concentration of each sample was adjusted to 50 ng/µL with M-elution Buffer or concentrated using speed vacuum. In total, 300 ng of converted DNA for each sample was used as a template on the Infinium MethylationEPIC BeadChip following the manufacturer's recommendations. Briefly, bisulfite-converted DNA was whole-genome amplified, fragmented, and hybridized to the array. After hybridization, the unhybridized and non-specifically hybridized DNA was washed away and the captured product was extended with fluorescent labels coupled to nucleotides. Finally, the arrays were scanned using a high-resolution Illumina scanner (iScan), which acquires light images emitted from the fluorophores. The intensities were measured and

methylation signals were extracted and recorded as raw data (IDAT). These assays were performed at the P3S platform (Sorbonne University). DNA methylation data were analyzed using the RnBeads package. Briefly, after the removal of bad quality samples, data were aligned to the hg19 assembly using the beta Mixture Quantile dilation (BMIQ) method for normalization and adjusted for sex as a covariate. Sex chromosomes were included, and sites with a standard deviation below 0.01 across all samples were filtered out. Together with default annotations, we included the enhancer coordinates (entire enhancer regions) as defined in the FANTOM5 enhancer-robust promoter associations. Briefly, using Pearson's correlation, enhancers with FDR < 1e-5 in an enhancer-promoter pair within 500 kb across cell types and organs were retained. Enhancer–promoter associations were computed between enhancers and all FANTOM-robust promoters. Epigenetic clock analysis of CD11B+ cells from the *ex vivo study* was conducted using "epiTOC2" (Epigenetic Timer Of Cancer), which calculates the mitotic age of the cells using the updated total number of divisions per stem cell[80]. This new method approximates age as a weighted estimate based on 163 CpG sites interrogated by the EPIC arrays.

RNA sequencing

Library preparations were performed with Kapa mRNA Hyper prep (Roche) following the manufacturer's instructions and sequenced (paired end) with the Illumina Novaseq 6000 Sequencing system with 200 cycles cartridge to obtain 2 × 60 million reads 100bases/RNA. Sequencing was performed at the iGenseq platform at the ICM – Paris Brain Institute. For the *in vitro* experiments, we combined Illumina Stranded Total RNA Prep and Ribo-Zero Plus. The quality of the raw data was evaluated using Fast QC. Sequences were trimmed or removed using Fastp software to retain only high-quality paired reads. Star v2.5.3a was used to align reads on the GRCh38 reference genome using default parameters, except for the maximum number of multiple alignments allowed for a read set to 1. Transcript quantification was performed using the rsem 1.2.28. Differential expression analysis was conducted using the quasi-likelihood F-test in the edgeR package. Normalized data were computed using the cpm function. Multiple hypothesis testing was corrected using the False

Discovery Rate Benjamini-Hochberg method. Samples from all *in vitro* experiments were analyzed in a paired manner for each individual.

Sequence motif enrichment analysis

Motif enrichment was performed using Hypergeometric Optimization of Motif EnRichment (HOMER) v4.11[81], enabling masking repeats, setting the parameter size to "given" and searching for motifs with a length within the range of 7-14 bp. We used HOCOMOCO v12 CORE as the reference dataset (matrix with a threshold level corresponding to a p-value of 0.001)[82].

Transcription factor activity

We used the CollecTRI database[41], which contains regulons comprising signed TF-target gene interactions, to infer TF activity. To estimate TF activity in hypermethylated enhancers, we considered genes with associated overexpression or downregulation (falling in quadrants I and IV, respectively; Fig. 2a). These genes were then interrogated among the targets of each TF in the database. TFs with at least five targets that were regulated in a positive or negative manner were retained. We then computed TF activity using the Normalized Enrichment Score (NES) of the Mann-Whitney-Wilcoxon gene set test (MWW-GST)[42]. We applied MWW-GST to each sample's normalized data and retained TFs with an FDR < 0.05, for the NES in at least 18 samples and an FDR < 0.05, in the comparison of the activity between groups (Wilcoxon's test). For promoters, we considered all genes associated with hypermethylation in the IDH^{mut} vs. IDH^{wt} comparison, without testing for differential activity between TFs. Heatmaps depicting TF activity at hypermethylated enhancers and promoters were generated using the z-score of activity.

Primary cultures of human microglia

Primary microglial cultures were prepared using surgical aspirates obtained from patients with brain tumors or drug-resistant epilepsy, following established surgical protocols. For gliomas, tissue collection involves the removal of both the adjacent "entry cortex" (the tissue

surrounding the surgical access point) and the tumor core, whereas in cases of epilepsy surgery, only normal tissue at the entry point is collected. Upon receipt (averaging 2 h), the tissues were promptly processed according to the protocol specified for human tumor samples. After enzymatic digestion and MACS purification, CD11B+ cells were counted and directly seeded in non-coated 12-well plates at a density of 750-1000 K cells/well in DMEM/F12, GlutaMAX medium (Gibco Ref# 10565018) supplemented with N-acetyl-cysteine and insulin [5 µg/mL], apo-Transferrin [100 µg/mL], sodium selenite [100 ng/mL], human TGFβ2 [2 ng/mL], CSF-1 [20 ng/mL], ovine wool cholesterol [1.5 µg/mL], ascorbic acid [75 µM] and penicillin/streptomycin[49]. All reagents and growth factors were purchased from Sigma and Preprotech, respectively. Non-permeable D-2HG acid disodium salt (Sigma-Aldrich) was used at a final concentration of 5 mM for all experiments, with treatments starting after 48 h of culture. Half of the culture medium was renewed every 2-3 days. For the 6 h LPS challenge experiments, 1% FBS was added to all conditions.

IDH^{mut} and IDH^{wt} cell lines

Human glioma cell lines IDH^{wt} were established by the GlioTEx team (Glioblastoma and Experimental Therapeutics) in the Paris Brain Institute (ICM) laboratory. Cultured cells were maintained at 37°C and 5% CO2 under neurosphere growth conditions in DMEM/F12 medium (Gibco) supplemented with 1% penicillin/streptomycin, B27 diluted 1:50 (Gibco), EGF (20 ng/mL), and FGF (20 ng/mL) (Preprotech). Human glioma cell lines IDH^{mut} BT88 and BT54, were kindly provided by Artee Luchman and Sam Weiss (University of Calgary), and BT237 and BT138 were kindly provided by Keith Ligon (Dana-Farber Cancer Institute). Cells were grown in DMEM/F12 medium (Gibco) supplemented with B27 (1/100; Gibco), 20ng/ml EGF and FGF (Peprotech). IDH^{wt} and IDH^{mut} cell lines were used as negative and positive controls, respectively, in the assays used to quantify intracellular D-2HG levels. An Idh1 R132H conditional knock-in (cKI) mouse line (Bardella et al., 2016) crossed with *Rosa26*$^{LSL\text{-}YFP}$ (Srinivas et al., 2001) was used to generate postnatal (P0-P1) neural progenitor cells. Cells were grown in DMEM/F-12 with GlutaMAX™ Supplement (61965-026, ThermoFisher), penicillin-streptomycin 1X (15140122, Life Technologies), B27 supplement 1X (17502048,

Thermo Fisher), N2 supplement 1X (17502048, Thermo Fisher), 0.6% w/v D-glucose (G8769, Sigma), 5mM HEPES (15630056, Life Technologies) and 20µg/ mL insulin (I5500, Sigma). Growth factors (20 ng/mL EGF GMP100-15, Peprotech and 10 ng/mL bFGF GMP100-18B, Peprotech) were added to the cultures and replaced every 2-3 days. Cells were maintained in a humidified incubator at 37°C and 5% CO2. Cultures were infected with a Cre-expressing adenovirus (Ad:cre, VB180308-1398jmt, VectorBuilder) after one passage, enabling recombination at the Idh1 and Rosa26LSL-YFP loci and leading to the expression of Idh1 R132H and YFP. Efficient DNA recombination was assessed by YFP visualization of NSC. Cells were cultured for 3-6 passages and assayed for D-2HG levels using a fluorometric test, TET enzymatic activity, and 5mC/5hmC genomic content using LC-MS/MS.

Immunofluorescence staining

Sterile coverslips were placed in 12 multiple wells and the surface was covered with poly-D-lysine and laminin (Sigma). The plate was incubated at room temperature (RT) for 2 h, and the solution was aspirated, rinsed with sterile water, and allowed to dry. Cells were seeded at a density of 750 K cells/well and maintained as described for 3, 10, and 17 days. The cells were washed with PBS (Gibco) and fixed with 4% paraformaldehyde (Electron Microscopy Sciences) in PBS for 10 min at RT. The cells were washed with PBS and permeabilized with 0,1% Triton X-100 in 1x PBS for 5 min at RT. Cells were quickly washed with PBS and blocked for non-specific binding sites with Human Fc Block (#564219, BD Pharmingen) for 10 min at RT, and subsequently with 5% donkey in PBS for 30-60 ^{2}min at RT. Incubation with primary antibodies was performed overnight at 4°C using anti-Iba1 (#19-19741, Wako; diluted 1/800), Tmem119 (#A16075D, BioLegend; diluted 1/100), or Ki-67 (#AB16667-1001, Abcam; diluted 1/250) in a humidified and light-protected chamber. The coverslips were washed with PBS and incubated with secondary antibodies (anti-rabbit #A21206 or anti-mouse #A21203; diluted 1/1000) in a blocking solution for 30 min at RT and temperature in the dark. Subsequently, the coverslips were washed with PBS, mounted with Fluoroshield-DAPI solution (Sigma), and observed under an Apotome inverted microscope (ZEISS Apotome 3) and a confocal microscope (A1R HD25 Nikon Inverted). Negative controls (background

fluorescence) were obtained by omitting the primary antibodies. The percentages of TMEM119+ and IBA1+ cells were determined in primary cultures grown in uncoated wells by counting three to five fields covering 0.22% of the well surface at different time points over a two-week period. Fields were randomly selected in the area where the cell density, as assessed by DAPI staining, was adequate.

Intracellular quantifications of D-2HG

Cultured cells were pelleted by centrifugation to remove the media, followed by two washes with ice-cold DPBS to ensure the complete removal of all D-2HG-containing media. Microglial cells were collected by trypsinization (0.25% for 5 min), whereas glioma cells and neurospheres were collected using Accutase. The corresponding culture medium, supplemented with 10% FBS, was added for inactivation. After centrifugation (300 g at 4°C for 5 min), the resulting pellet was washed with cold DPBS. Cell pellets were then preserved at -80°C until use. The concentration of D-2HG in the cell lysates was determined using the D-2-Hydroxyglutarate (D-2HG) Assay Kit (Ref MAK320, Sigma) and LC/MS for validation. For the fluorometric assay, cellular extracts were prepared by adding 75 µL of CelLytic MT Cell Lysis Reagent (Sigma) with a Protease Inhibitor Cocktail (Sigma). An aliquot was used for protein quantification using the Pierce™ BCA Protein Assay Kit (Thermo Fisher Scientific). The collected supernatants were deproteinized by perchloric acid precipitation and neutralized with KOH. A standard curve was prepared using serial dilutions of D-2HG. An equivalent of 5000 pmol was added to the cell extract and used as a spike-in internal control. The plates were then incubated at 37°C for 30–60 min. This assay is based on the oxidation of D-2HG to α-ketoglutarate (αKG) by the enzyme (D)-2-hydroxyglutarate dehydrogenase (HGDH) coupled with the reduction of NAD+ to NADH[83]. The amount of NADH formed was then quantitated by diaphorase-mediated reduction of resazurin to the fluorescent dye resorufin (λex = 540 nm, λem = 590 nm) using a Spectramax i3x microplate reader. The concentration of D-2HG in each sample was estimated as pmol/µg protein. For quantification of 2HG using LC-MS, dry cell pellets were lysed in water, and the solution was divided in half for 2-HG measurement and protein quantification. NaCl was added and the samples were acidified

using HCl. Liquid-liquid extraction of organic acids with ethyl acetate was performed. Three extractions were performed and the organic phases were pooled and dried under a nitrogen stream at 30°C. The samples were then derived using a standard silylation protocol, N, O-bis [trimethylsilyl] trifluoroacetamide, and 1% trimethylchlorosilane (TMCS) under anhydrous conditions using pyridine. Chromatographic separation was performed using a TR-5MS (30m x 0.25 mm x 0.25 mm) column from Thermo Scientific (Waltham, Massachusets, USA). The spectral data were acquired using XCalibur software (Thermo Electron Corporation, Austin, TX, USA). The samples were placed for 30 min at 80°C and then injected into the GC system. Quantification was performed using the internal standard 2-hydroxyglutaric acid-D3 from Cambridge Isotope Laboratories (Tewksbury, Massachusetts, USA).

LC-MS/MS assessment of genomic 5mC and 5hmC content

Genomic DNA (gDNA) was isolated as indicated and concentrated by ethanol precipitation. Samples were then digested at 37°C for 12 h in 25 µL reactions containing 1-4 µg of gDNA, 7.5 U of DNA Degradase Plus (Zymo Research), reaction buffer, and isotope-labeled internal standards [700 pmol 2'-deoxycytidine-15N3 (Cambridge Isotope Laboratories, Inc.); 1.75 pmol 5-methyl-2′-deoxy cytidine-d3 (Toronto Research Chemicals), 1 pmol 5-hydroxymethyl-2′-deoxycytidine-d3 (Toronto Research Chemicals)] for quantification. Prior to LC/MS analysis, the samples were diluted 1:1 in mobile phase component A (see below). The LC-MS system consisted of a Shimadzu Nexera UPLC system in line with a SCIEX 6500 QTrap mass spectrometer equipped with a TurboV Ion spray source and operated in positive ion mode. The analytes were chromatographed on a gradient elution system in which mobile phase A was water with 10 mM ammonium formate and 0.05% trifluoroacetic acid (TFA) (Sigma Aldrich), and mobile phase B was 7:1 methanol:acetonitrile (Thermo Fisher Scientific) with 10 mM ammonium formate and 0.05% TFA. The column was a Phenomenex Curosil-PFP column (10 x 0.2 cm 1.7 um) (Phenomenex Inc.) held at 42°C. The flow rate was 300 µL/min and the gradient started at 1.0% B (held for 30 s) and was then increased to 19% over 5 min. All analytes were detected using selected reaction monitoring (SRM). Analyst software (version 1.6.2) was used to acquire and process data. Supplementary Table S6 lists

the Q1 and Q3 m/z values, collision energies (CE), and declustering potentials (DP) for all analytes and their internal standards. The analytes were quantified using stable isotope dilutions against stably labeled internal standards. Data represent the percentage of each analyte relative to the total cytosine pool (dC+5mC+5hmC) in the same sample.

Reduced Representation Enzymatic Methyl sequencing (RREM-seq)

Library preparation was performed using 100 ng of genomic DNA spiked with 0.95 ng of unmethylated Lambda DNA and 0.05 ng and CpG methylated pUC19. The mixture was digested with 400 units of MspI (New England Biolabs) in NEB Ultra II buffer (New England Biolabs) in a final volume of 57 µL for 2 h at 37°C. After enzymatic DNA digestion, the fragments were repaired and A-tailed using 15 units of Klenow 3'-5' exo- (New England Biolabs). After End-repair and A-tailing, Illumina universal methylated adapters were ligated to DNA fragments using the NEB Ultra II ligation module, following the manufacturer's recommendations. After ligation, DNA fragments were purified and size-selected using two-step SPRI bead purification to select fragments from 40bp to 400bp. The clean-up ligated DNA was eluted with 10 mM Tris at pH 8. The purified product was then converted using the enzymatic methyl-seq module (New England Biolabs), following the manufacturer's recommendations. Briefly, 5mC was converted to 5hmC by TET2, and 5hmC was specifically protected from APOBEC deamination by T4-BGT glycosylation. After 5hmC/5mC glycosylation, the libraries were denatured for 10 min at 85°C in 20% formamide. The unmodified cytosines were then deaminated during the APOBEC reaction. The converted product was amplified by PCR using indexing primers and polymerase KAPA HiFi Hotstart U+ Ready Mix 2X in a final volume of 50 µL for 13 cycles. PCR products were purified at a 1.2 × SPRI ratio and then controlled by capillary electrophoresis on a Fragment Analyzer. After quantification by qPCR, libraries were sequenced on Illumina Novaseq 6000 paired-end 100b reads.

Reduced Representation hydroxyMethyl sequencing (RREhM-seq)

We used the RREhM-seq protocol described by Sun et al[52] with slight modifications. Library preparation was performed using an input of 200 ng with a spike of 1.9 ng of unmethylated Lambda DNA and CpG methylated pUC19 (0.1 ng). Following MspI digestion and reparation with Klenow 3'-5' exo-and pyrrolo-dC, Illumina adapters were used instead of 5mC adapters during the ligation step. For the TET2 step during conversion, the TET2 enzyme and Fe2+ were replaced with H_2O to avoid 5mC protection. The product was deaminated, amplified, qualified, and sequenced under the same conditions as those used in the RREM-seq libraries. RREM-seq and RREhM-seq were performed using Integragen SA (Evry, France).

RREM-seq & RREhM-seq data analysis

The FastQ files were aligned using BSseeker2 (https://github.com/BSSeeker/BSseeker2) on the hg19 genome using bowtie2. The hg19 index was built with the rrbs option, and fragment size between 40bp and 400 bp were selected. The adapter sequence and CCGG motifs were removed during alignment. After alignment, methylation calling was performed to obtain the methylation level and cover each cytosine position in the library. Options for removing overlaps and low-quality sequences were also enabled. For RREM-seq libraries, methylation signals correspond to 5mC and 5hmC, whereas methylation signals only concern 5hmC in RREhM-seq libraries[84]. Levels of total 5mC (methylation and hydroxymethylation) or 5hmC were defined as the percentage of the number of reads with the corresponding modification on a specific cytosine divided by the number of reads covering that cytosine (modified or unmodified). The methylation-only level was calculated by subtracting the 5hmC level from the total 5mC level. CpG sites were analyzed with the methylKit package[85] using a minimum coverage of 10 reads per base. For the defined window analysis, TFs motifs were retrieved from HOCOMOCO v12 CORE and searched inside entire enhancer regions using the Biostrings package[86] with a maximum mismatch of one base. The region of interest was defined as a window of 600 bp centered around the first base of the motif. For each patient, only the common enhancer windows between the treated and control samples were analyzed. Microglial samples used for analyses of 5mC and 5hmC at 2 days (2D) and 14 days (14D) were obtained from surgical aspirates of normal tissue from

three patients with epilepsy who underwent surgery. One technical outlier from the 5hmC analysis at 14D was excluded from the study. The 5mC-only and 5hmC levels were reported as the mean across patients for each time point/condition using only the common enhancer regions or defined windows shared among patients.

TET enzymatic assay

Nuclei were isolated using a nuclear extraction kit (Cat. Ab113474, Abcam, Cambridge, MA, USA). Cells were collected by trypsinization (0.25% for 5 min) and counted. The cells were then resuspended in an appropriate volume of pre-extraction buffer containing dithiothreitol and protease inhibitor cocktail and incubated on ice for 2 min. After centrifugation at 12,000 rpm for 3 min, the cytoplasmic extract (supernatant) was carefully removed, leaving a nuclear pellet. Two volumes of extraction buffer containing dithiothreitol and protease inhibitor cocktail were added to the nuclear pellet. The extract was incubated on ice for 15 min and vortexed every 3 min for 5 s. After incubation, the suspension was centrifuged for 10 min at 14,000 rpm and 4°C, and the resulting supernatant was transferred to a new microcentrifuge vial. Protein quantification from the nuclear extract was performed using a Pierce™ BCA Protein Assay Kit (Thermo Fisher Scientific) following the manufacturer's instructions. Technical triplicates for this assay were performed using 12 µg of protein from nuclear extracts of microglial cells (untreated and treated with D-2HG), as well as from external controls (neurospheres obtained from the cKI Idh R132H mouse model). To determine TET enzymatic activity, we used the TET Hydroxylase Activity Kit from Abcam (ab156913). In this fluorometric assay, a methylated substrate was stably coated onto microplate wells. Active TET enzymes bind to the substrate and convert the methylated substrate into hydroxymethylated products. The hydroxymethylated products generated by the TET activity can be detected using a specific antibody. The ratio or amount of hydroxymethylated products, which is proportional to the enzyme activity, was measured fluorometrically using a fluorescent microplate reader with excitation at 530 nm and emission at 590 nm. The TET enzyme activity was proportional to the measured relative fluorescent units.

RT-qPCR

Total RNA from cultured microglia was purified using a Maxwell RSC simplyRNA Cell Kit (Promega). Next, 300 ng of RNA was reverse-transcribed into complementary DNA using the Maxima First Strand cDNA Synthesis Kit (Thermo Fisher Scientific). Assays were run in triplicate on a Light Cycler 480 instrument (Roche) using the LightCycler 480 SYBR Green Master 2X (Roche). The primer sequences used were as follows: TNFA, forward: 5'-GAGCCAGCTCCCTCTATTTA-3'; reverse: 5'-GGGAACAGCCTATTGTTCAG-3'; IL-6, forward: 5'-CCTTCCAAAGATGGCTGAAA-3'; reverse: 5'-TGGCTTGTTCCTCACTACT-3'; PPIA, forward: 5'-ATGCTGGACCCAACACAAAT-3'; reverse: 5'-TCTTTCACTTTGCCAAACACC-3'; ACTB, forward: 5'-CCAACCGCGAGAAGATGA-3'; reverse: 5'- CCAGAGGCGTACAGGGATAG-3'. Linearity, efficiency, and specific amplification were verified for all primer sets. Relative quantification of cytokine expression was normalized to the mean of the two control genes (PPIA and ACTB) and expressed as fold change[87].

Mitochondrial respiration measurement

Real-time measurement of the oxygen consumption rate (OCR) was performed using an XFe extracellular flux analyzer (Seahorse Bioscience, Billerica, MA, USA), following the manufacturer's instructions. Primary isolated microglia were plated at a density of 1,000,000 cells/well in XFe24 cell culture microplates pre-coated with poly-L-lysine (Sigma-Aldrich). Cells were maintained in 200 µl DMEM/F-12 medium, supplemented as previously indicated, and treated with 5 mM D-2HG for 12 days. Half of the culture medium was renewed every 2-3 days. On the day of the experiment, cells were stimulated with LPS (1µg/mL) in medium supplemented with FBS 1% for 6 h. FBS 1% was also added to the other experimental conditions. Next, the medium was replaced by Seahorse XF base medium (Agilent, 102353-100) supplemented with 17.5 mM D-Glucose (Dextrose), 0.5 mM sodium pyruvate and 2.5 mM L-Glutamine and incubated for 1 h in CO2 free incubator at 37°C. The utility plate was hydrated with an XF calibrant solution (pH 7.4) (Agilent, 100840-000; 1 mL/well) and incubated overnight (37°C, CO2-free). The next day, the utility plate with the cartridge containing the injector ports and sensors was run on Seahorse for calibration. The assay

medium (Seahorse XF DMEM assay medium, pH 7.4) was prepared immediately before the assay. OCR was measured under basal conditions and after sequential injections of the following inhibitors: oligomycin (1 µM) to stop ATP synthase, FCCP (1 µM) to dissipate the proton gradient, and Rotenone/Antimycin A (0.5 µM each to block the electron transport chain (ETC). All the following measurements were carried out with a 2 min mix, 2 min delay, and 3 min measure. Three baseline OCR measurements were recorded, and mitochondrial metabolism was assessed by injection of oligomycin, FCCP, and a combination of rotenone and antimycin A. The following parameters were deduced: basal respiration (OCR values used to provide ATP under baseline conditions), ATP-linked respiration (following oligomycin injection, a reduction in OCR values represents the part of basal respiration used to produce ATP), and maximal respiration (maximal OCR values following FCCP injection). Basal respiration was calculated by subtracting the last rate measured before oligomycin injection from the non-mitochondrial respiration rate (NMRT), which was determined as the minimum rate measured after rotenone/antimycin A injection. Maximal respiration was calculated by subtracting the maximum measurement after the FCCP injection and NMRT. ATP-linked respiration was calculated by subtracting the last rate measured before oligomycin injection from the minimum rate measured after oligomycin injection. OCR data were normalized to the number of viable cells estimated at the end of the experiment. To do this, the cells were fixed with paraformaldehyde 4%, followed by washing with PBS and DAPI [10 µg/mL]. Nuclei were automatically counted on the CellInsight NXT platform.

Single-nucleus RNA sequencing analysis

We downloaded raw data for oligodendroglioma (patient BWH445) from Spitzer et al. study on IDHi[55] GSE260928 and used Seurat (version 5.0.3)[88] to perform the data analysis. First, we performed data quality control, excluding cells with less than 1500 or more than 3400 genes expressed and less than 2200 or more than 12000 unique molecular identifiers. These stringent thresholds allowed us to obtain high-quality nuclei and to avoid doublets. Subsequently, we normalized the entire raw gene count matrix by regularized negative binomial regression using the sctransform function version 2 and clustered the cells using

30 principal components. We selected the microglial cluster based on the expression of TAL1, P2RY12, and SLC2A5 and the absence of the infiltrating myeloid marker CD163. Selected microglial cells were then analyzed using the raw expression matrix, normalized with the SC Transform function version 2, and clustered using 20 principal components. Differential expression analysis was performed using the FindMarker function.

Statistical analysis and plots generation

Sample sizes and statistical tests are provided in the figure legends. Analyses were performed using R. normal distribution of data was verified using Shapiro-Wilk's normality test (p-value > 0.05). Plots and analyses were generated using ggplot2[89], extension ggsignif[90], ComplexHeatmap[91], Cytoscape[92], clusterProfiler[93] and eulerr[94]. The hallmark gene set collection (v2023.1. Hs) for GSEA analyses[95] were downloaded from the Molecular Signatures Database (MSigDB)[96].

Data and code availability

Data and code are available upon request.

Supplementary Tables

Supplementary Table S1: Clinical, pathological and genetic features of the study cohort.

Supplementary Table S2: Genes regulated by hypermethylated enhancers and promoters in CD11B+ cells from IDH^{mut} gliomas.

Supplementary Table S3: Differentially expressed genes in CD11B+ cells from IDH^{mut} vs. IDH^{wt} gliomas.

Supplementary Table S4: Genes regulated by hypermethylated enhancers and/or promoters linked to downregulated expression in CD11B+ cells from IDH^{mut} vs. IDH^{wt} gliomas.

Supplementary Table S5: Genes regulated by the selected enhancers bound by TFs in Fig. 5c exhibiting hypermethylation/hypohydroxymethylation in D-2HG-treated microglia.

Supplementary Table S6: Analyte and internal standard Q1 and Q3 *m/z* values, collision energy (CE), and declustering potential (DP) for LC-MS/MS quantification.

References

1. van den Bent, M. J., Geurts, M., French, P. J., Smits, M., Capper, D., Bromberg, J. E. C., & Chang, S. M. (2023). Primary brain tumours in adults. The Lancet, 402(10412), 1564–1579. https://doi.org/10.1016/S0140-6736(23)01054-1.
2. Dang, L., White, D. W., Gross, S., Bennett, B. D., Bittinger, M. A., Driggers, E. M., Fantin, V. R., Jang, H. G., Jin, S., Keenan, M. C., Marks, K. M., Prins, R. M., Ward, P. S., Yen, K. E., Liau, L. M., Rabinowitz, J. D., Cantley, L. C., Thompson, C. B., vander Heiden, M. G., & Su, S. M. (2009). Cancer-associated IDH1 mutations produce 2-hydroxyglutarate. Nature, 462(7274), 739–744. https://doi.org/10.1038/nature08617.
3. Richard, Q., Laurenge, A., Mallat, M., Sanson, M., & Castro-Vega, L. J. (2022). New insights into the Immune TME of adult-type diffuse gliomas. Current Opinion in Neurology, 35(6), 794–802. https://doi.org/10.1097/WCO.0000000000001112.
4. Linninger, A., Hartung, G. A., Liu, B. P., Mirkov, S., Tangen, K., Lukas, R. v, Unruh, D., James, C. D., Sarkaria, J. N., & Horbinski, C. (2018). Modeling the diffusion of D-2-hydroxyglutarate from IDH1 mutant gliomas in the central nervous system. Neuro-Oncology, 20(9), 1197–1206. https://doi.org/10.1093/neuonc/noy051.
5. Pickard, A. J., Sohn, A. S. W., Bartenstein, T. F., He, S., Zhang, Y., & Gallo, J. M. (2016). Intracerebral Distribution of the Oncometabolite d-2-Hydroxyglutarate in Mice Bearing Mutant Isocitrate Dehydrogenase Brain Tumors: Implications for Tumorigenesis. Frontiers in Oncology, 6. https://doi.org/10.3389/fonc.2016.00211.
6. Bunse, L., Pusch, S., Bunse, T., Sahm, F., Sanghvi, K., Friedrich, M., Alansary, D., Sonner, J. K., Green, E., Deumelandt, K., Kilian, M., Neftel, C., Uhlig, S., Kessler, T., von Landenberg, A., Berghoff, A. S., Marsh, K., Steadman, M., Zhu, D., … Platten, M. (2018). Suppression of antitumor T cell immunity by the oncometabolite (R)-2-hydroxyglutarate. Nature Medicine, 24(8), 1192–1203. https://doi.org/10.1038/s41591-018-0095-6.
7. Böttcher, M., Renner, K., Berger, R., Mentz, K., Thomas, S., Cardenas-Conejo, Z. E., Dettmer, K., Oefner, P. J., Mackensen, A., Kreutz, M., & Mougiakakos, D. (2018). D-2-hydroxyglutarate interferes with HIF-1α stability skewing T-cell metabolism towards

oxidative phosphorylation and impairing Th17 polarization. OncoImmunology, 7(7), e1445454. https://doi.org/10.1080/2162402X.2018.1445454.

8. Ugele, I., Cárdenas-Conejo, Z., Hammon, K., Wehrstein, M., Bruss, C., Peter, K., Singer, K., Gottfried, E., Boesch, J., Oefner, P., Dettmer, K., Renner, K., & Kreutz, M. (2019). D-2-Hydroxyglutarate and L-2-Hydroxyglutarate Inhibit IL-12 Secretion by Human Monocyte-Derived Dendritic Cells. International Journal of Molecular Sciences, 20(3), 742. https://doi.org/10.3390/ijms20030742.
9. Friedrich, M., Sankowski, R., Bunse, L., Kilian, M., Green, E., Ramallo Guevara, C., Pusch, S., Poschet, G., Sanghvi, K., Hahn, M., Bunse, T., Münch, P., Gegner, H. M., Sonner, J. K., von Landenberg, A., Cichon, F., Aslan, K., Trobisch, T., Schirmer, L., … Platten, M. (2021). Tryptophan metabolism drives dynamic immunosuppressive myeloid states in IDH-mutant gliomas. Nature Cancer, 2(7), 723–740. https://doi.org/10.1038/s43018-021-00201-z.
10. Notarangelo, G., Spinelli, J. B., Perez, E. M., Baker, G. J., Kurmi, K., Elia, I., Stopka, S. A., Baquer, G., Lin, J.-R., Golby, A. J., Joshi, S., Baron, H. F., Drijvers, J. M., Georgiev, P., Ringel, A. E., Zaganjor, E., McBrayer, S. K., Sorger, P. K., Sharpe, A. H., … Haigis, M. C. (2022). Oncometabolite R-2HG alters T cell metabolism to impair CD8 + T cell function. Science, 377(6614), 1519–1529. https://doi.org/10.1126/science.abj5104.
11. Ruiz-Moreno, C., Marco Salas, S., Samuelsson, E., Brandner, S., Kranendonk, M.E., Nilsson, M., Stunnenberg, H.G. Harmonized single-cell landscape, intercellular crosstalk and tumor architecture of glioblastoma. doi: https://doi.org/10.1101/2022.08.27.505439.
12. Müller, S., Kohanbash, G., Liu, S. J., Alvarado, B., Carrera, D., Bhaduri, A., Watchmaker, P. B., Yagnik, G., di Lullo, E., Malatesta, M., Amankulor, N. M., Kriegstein, A. R., Lim, D. A., Aghi, M., Okada, H., & Diaz, A. (2017). Single-cell profiling of human gliomas reveals macrophage ontogeny as a basis for regional differences in macrophage activation in the tumor microenvironment. Genome Biology, 18(1), 234. https://doi.org/10.1186/s13059-017-1362-4.

13. Mantovani, A., Allavena, P., Marchesi, F., & Garlanda, C. (2022). Macrophages as tools and targets in cancer therapy. Nature Reviews Drug Discovery, 21(11), 799–820. https://doi.org/10.1038/s41573-022-00520-5.
14. Park, M. D., Silvin, A., Ginhoux, F., & Merad, M. (2022). Macrophages in health and disease. Cell, 185(23), 4259–4279. https://doi.org/10.1016/j.cell.2022.10.007.
15. Amit, I., Winter, D. R., & Jung, S. (2016). The role of the local environment and epigenetics in shaping macrophage identity and their effect on tissue homeostasis. Nature Immunology, 17(1), 18–25. https://doi.org/10.1038/ni.3325.
16. Bowman, R. L., Klemm, F., Akkari, L., Pyonteck, S. M., Sevenich, L., Quail, D. F., Dhara, S., Simpson, K., Gardner, E. E., Iacobuzio-Donahue, C. A., Brennan, C. W., Tabar, V., Gutin, P. H., & Joyce, J. A. (2016). Macrophage Ontogeny Underlies Differences in Tumor-Specific Education in Brain Malignancies. Cell Reports, 17(9), 2445–2459. https://doi.org/10.1016/j.celrep.2016.10.052.
17. Klemm, F., Maas, R. R., Bowman, R. L., Kornete, M., Soukup, K., Nassiri, S., Brouland, J.-P., Iacobuzio-Donahue, C. A., Brennan, C., Tabar, V., Gutin, P. H., Daniel, R. T., Hegi, M. E., & Joyce, J. A. (2020). Interrogation of the Microenvironmental Landscape in Brain Tumors Reveals Disease-Specific Alterations of Immune Cells. Cell, 181(7), 1643-1660.e17. https://doi.org/10.1016/j.cell.2020.05.007.
18. Friebel, E., Kapolou, K., Unger, S., Núñez, N. G., Utz, S., Rushing, E. J., Regli, L., Weller, M., Greter, M., Tugues, S., Neidert, M. C., & Becher, B. (2020). Single-Cell Mapping of Human Brain Cancer Reveals Tumor-Specific Instruction of Tissue-Invading Leukocytes. Cell, 181(7), 1626-1642.e20. https://doi.org/10.1016/j.cell.2020.04.055.
19. Venteicher, A. S., Tirosh, I., Hebert, C., Yizhak, K., Neftel, C., Filbin, M. G., Hovestadt, V., Escalante, L. E., Shaw, M. L., Rodman, C., Gillespie, S. M., Dionne, D., Luo, C. C., Ravichandran, H., Mylvaganam, R., Mount, C., Onozato, M. L., Nahed, B. v., Wakimoto, H., … Suvà, M. L. (2017). Decoupling genetics, lineages, and microenvironment in IDH-mutant gliomas by single-cell RNA-seq. Science, 355(6332). https://doi.org/10.1126/science.aai8478.

20. Hara, T., Chanoch-Myers, R., Mathewson, N. D., Myskiw, C., Atta, L., Bussema, L., Eichhorn, S. W., Greenwald, A. C., Kinker, G. S., Rodman, C., Gonzalez Castro, L. N., Wakimoto, H., Rozenblatt-Rosen, O., Zhuang, X., Fan, J., Hunter, T., Verma, I. M., Wucherpfennig, K. W., Regev, A., … Tirosh, I. (2021). Interactions between cancer cells and immune cells drive transitions to mesenchymal-like states in glioblastoma. Cancer Cell, 39(6), 779-792.e11. https://doi.org/10.1016/j.ccell.2021.05.002.
21. Blanco-Carmona, E., Narayanan, A., Hernandez, I., Nieto, J. C., Elosua-Bayes, M., Sun, X., Schmidt, C., Pamir, N., Özduman, K., Herold-Mende, C., Pagani, F., Cominelli, M., Taranda, J., Wick, W., von Deimling, A., Poliani, P. L., Rehli, M., Schlesner, M., Heyn, H., & Turcan, Ş. (2023). Tumor heterogeneity and tumor-microglia interactions in primary and recurrent IDH1-mutant gliomas. Cell Reports Medicine, 4(11), 101249. https://doi.org/10.1016/j.xcrm.2023.101249.
22. Gupta, P., Dang, M., Oberai, S., Migliozzi, S., Trivedi, R., Kumar, G., … & Bhat, K. P. (2024). Immune landscape of isocitrate dehydrogenase-stratified primary and recurrent human gliomas. Neuro-Oncology, noae139. doi: https://doi.org/10.1093/neuonc/noae139.
23. Miller, E., El Farran, C.A., Couturier, C.P., Chen, Z., D'Antonio, J.P., Verga, J., Villanueva, M.A., Gonzalez Castro, L.N., Tong, Y.E., Saadi, T.A., Chiocca, A.N., Fischer, D.S., Heiland, D.H., Guerriero, J.L., Petrecca, K., Suva, M.L., Shalek, A.K., Bernstein, B.E. (2023). Programs, Origins, and Niches of Immunomodulatory Myeloid Cells in Gliomas. doi: https://doi.org/10.1101/2023.10.24.563466.
24. Pombo Antunes, A. R., Scheyltjens, I., Lodi, F., Messiaen, J., Antoranz, A., Duerinck, J., Kancheva, D., Martens, L., de Vlaminck, K., van Hove, H., Kjølner Hansen, S. S., Bosisio, F. M., van der Borght, K., de Vleeschouwer, S., Sciot, R., Bouwens, L., Verfaillie, M., Vandamme, N., Vandenbroucke, R. E., … Movahedi, K. (2021). Single-cell profiling of myeloid cells in glioblastoma across species and disease stage reveals macrophage competition and specialization. Nature Neuroscience, 24(4), 595–610. https://doi.org/10.1038/s41593-020-00789-y.

25. Yeo, A. T., Rawal, S., Delcuze, B., Christofides, A., Atayde, A., Strauss, L., Balaj, L., Rogers, V. A., Uhlmann, E. J., Varma, H., Carter, B. S., Boussiotis, V. A., & Charest, A. (2022). Single-cell RNA sequencing reveals evolution of immune landscape during glioblastoma progression. Nature Immunology, 23(6), 971–984. https://doi.org/10.1038/s41590-022-01215-0.
26. Abdelfattah, N., Kumar, P., Wang, C., Leu, J.-S., Flynn, W. F., Gao, R., Baskin, D. S., Pichumani, K., Ijare, O. B., Wood, S. L., Powell, S. Z., Haviland, D. L., Parker Kerrigan, B. C., Lang, F. F., Prabhu, S. S., Huntoon, K. M., Jiang, W., Kim, B. Y. S., George, J., & Yun, K. (2022). Single-cell analysis of human glioma and immune cells identifies S100A4 as an immunotherapy target. Nature Communications, 13(1), 767. https://doi.org/10.1038/s41467-022-28372-y.
27. Noushmehr, H., Weisenberger, D. J., Diefes, K., Phillips, H. S., Pujara, K., Berman, B. P., Pan, F., Pelloski, C. E., Sulman, E. P., Bhat, K. P., Verhaak, R. G. W., Hoadley, K. A., Hayes, D. N., Perou, C. M., Schmidt, H. K., Ding, L., Wilson, R. K., van den Berg, D., Shen, H., … Aldape, K. (2010). Identification of a CpG Island Methylator Phenotype that Defines a Distinct Subgroup of Glioma. Cancer Cell, 17(5), 510–522. https://doi.org/10.1016/j.ccr.2010.03.017.
28. Chuntova, P., Yamamichi, A., Chen, T., Narayanaswamy, R., Ronseaux, S., Hudson, C., Tron, A. E., Hyer, M. L., Montoya, M., Mende, A. L., Nejo, T., Downey, K. M., Diebold, D., Lu, M., Nicolay, B., & Okada, H. (2022). Inhibition of D-2HG leads to upregulation of a proinflammatory gene signature in a novel HLA-A2/HLA-DR1 transgenic mouse model of IDH1R132H-expressing glioma. Journal for ImmunoTherapy of Cancer, 10(5), e004644. https://doi.org/10.1136/jitc-2022-004644.
29. de Witte, L. D., Wang, Z., Snijders, G. L. J. L., Mendelev, N., Liu, Q., Sneeboer, M. A. M., Boks, M. P. M., Ge, Y., & Haghighi, F. (2022). Contribution of Age, Brain Region, Mood Disorder Pathology, and Interindividual Factors on the Methylome of Human Microglia. Biological Psychiatry, 91(6), 572–581. https://doi.org/10.1016/j.biopsych.2021.10.020.

30. Zheng, P.-P., van der Weiden, M., van der Spek, P. J., Vincent, A. J. P. E., & Kros, J. M. (2012). Isocitrate dehydrogenase 1R132H mutation in microglia/macrophages in gliomas. Cancer Biology & Therapy, 13(10), 836–839. https://doi.org/10.4161/cbt.20836.
31. Ceccarelli, M., Barthel, F. P., Malta, T. M., Sabedot, T. S., Salama, S. R., Murray, B. A., Morozova, O., Newton, Y., Radenbaugh, A., Pagnotta, S. M., Anjum, S., Wang, J., Manyam, G., Zoppoli, P., Ling, S., Rao, A. A., Grifford, M., Cherniack, A. D., Zhang, H., … Zmuda, E. (2016). Molecular Profiling Reveals Biologically Discrete Subsets and Pathways of Progression in Diffuse Glioma. Cell, 164(3), 550–563. https://doi.org/10.1016/j.cell.2015.12.028.
32. Klughammer, J., Kiesel, B., Roetzer, T., Fortelny, N., Nemc, A., Nenning, K.-H., Furtner, J., Sheffield, N. C., Datlinger, P., Peter, N., Nowosielski, M., Augustin, M., Mischkulnig, M., Ströbel, T., Alpar, D., Ergüner, B., Senekowitsch, M., Moser, P., Freyschlag, C. F., … Bock, C. (2018). The DNA methylation landscape of glioblastoma disease progression shows extensive heterogeneity in time and space. Nature Medicine, 24(10), 1611–1624. https://doi.org/10.1038/s41591-018-0156-x.
33. Binder, H., Willscher, E., Loeffler-Wirth, H., Hopp, L., Jones, D. T. W., Pfister, S. M., Kreuz, M., Gramatzki, D., Fortenbacher, E., Hentschel, B., Tatagiba, M., Herrlinger, U., Vatter, H., Matschke, J., Westphal, M., Krex, D., Schackert, G., Tonn, J. C., Schlegel, U., … Loeffler, M. (2019). DNA methylation, transcriptome and genetic copy number signatures of diffuse cerebral WHO grade II/III gliomas resolve cancer heterogeneity and development. Acta Neuropathologica Communications, 7(1), 59. https://doi.org/10.1186/s40478-019-0704-8.
34. Andersson, R., Gebhard, C., Miguel-Escalada, I., Hoof, I., Bornholdt, J., Boyd, M., Chen, Y., Zhao, X., Schmidl, C., Suzuki, T., Ntini, E., Arner, E., Valen, E., Li, K., Schwarzfischer, L., Glatz, D., Raithel, J., Lilje, B., Rapin, N., … Sandelin, A. (2014). An atlas of active enhancers across human cell types and tissues. Nature, 507(7493), 455–461. https://doi.org/10.1038/nature12787.

35. Chaligne, R., Gaiti, F., Silverbush, D., Schiffman, J. S., Weisman, H. R., Kluegel, L., Gritsch, S., Deochand, S. D., Gonzalez Castro, L. N., Richman, A. R., Klughammer, J., Biancalani, T., Muus, C., Sheridan, C., Alonso, A., Izzo, F., Park, J., Rozenblatt-Rosen, O., Regev, A., … Landau, D. A. (2021). Epigenetic encoding, heritability and plasticity of glioma transcriptional cell states. Nature Genetics, 53(10), 1469–1479. https://doi.org/10.1038/s41588-021-00927-7.
36. Stadler, M. B., Murr, R., Burger, L., Ivanek, R., Lienert, F., Schöler, A., Nimwegen, E. van, Wirbelauer, C., Oakeley, E. J., Gaidatzis, D., Tiwari, V. K., & Schübeler, D. (2011). DNA-binding factors shape the mouse methylome at distal regulatory regions. Nature, 480(7378), 490–495. https://doi.org/10.1038/nature10716.
37. Aran, D., Sabato, S., & Hellman, A. (2013). DNA methylation of distal regulatory sites characterizes dysregulation of cancer genes. Genome Biology, 14(3), R21. https://doi.org/10.1186/gb-2013-14-3-r21.
38. Blattler, A., & Farnham, P. J. (2013). Cross-talk between Site-specific Transcription Factors and DNA Methylation States. Journal of Biological Chemistry, 288(48), 34287–34294. https://doi.org/10.1074/jbc.R113.512517.
39. Gosselin, D., Skola, D., Coufal, N. G., Holtman, I. R., Schlachetzki, J. C. M., Sajti, E., Jaeger, B. N., O'Connor, C., Fitzpatrick, C., Pasillas, M. P., Pena, M., Adair, A., Gonda, D. D., Levy, M. L., Ransohoff, R. M., Gage, F. H., & Glass, C. K. (2017). An environment-dependent transcriptional network specifies human microglia identity. Science, 356(6344). https://doi.org/10.1126/science.aal3222.
40. Court, F., le Boiteux, E., Fogli, A., Müller-Barthélémy, M., Vaurs-Barrière, C., Chautard, E., Pereira, B., Biau, J., Kemeny, J.-L., Khalil, T., Karayan-Tapon, L., Verrelle, P., & Arnaud, P. (2019). Transcriptional alterations in glioma result primarily from DNA methylation–independent mechanisms. Genome Research, 29(10), 1605–1621. https://doi.org/10.1101/gr.249219.119.
41. Müller-Dott, S., Tsirvouli, E., Vazquez, M., Ramirez Flores, R. O., Badia-i-Mompel, P., Fallegger, R., Türei, D., Lægreid, A., & Saez-Rodriguez, J. (2023). Expanding the coverage of regulons from high-confidence prior knowledge for accurate estimation

of transcription factor activities. Nucleic Acids Research, 51(20), 10934–10949. https://doi.org/10.1093/nar/gkad841.

42. Frattini, V., Pagnotta, S. M., Tala, Fan, J. J., Russo, M. v., Lee, S. B., Garofano, L., Zhang, J., Shi, P., Lewis, G., Sanson, H., Frederick, V., Castano, A. M., Cerulo, L., Rolland, D. C. M., Mall, R., Mokhtari, K., Elenitoba-Johnson, K. S. J., Sanson, M., … Iavarone, A. (2018). A metabolic function of FGFR3-TACC3 gene fusions in cancer. Nature, 553(7687), 222–227. https://doi.org/10.1038/nature25171.
43. Yin, Y., Morgunova, E., Jolma, A., Kaasinen, E., Sahu, B., Khund-Sayeed, S., Das, P. K., Kivioja, T., Dave, K., Zhong, F., Nitta, K. R., Taipale, M., Popov, A., Ginno, P. A., Domcke, S., Yan, J., Schübeler, D., Vinson, C., & Taipale, J. (2017). Impact of cytosine methylation on DNA binding specificities of human transcription factors. Science, 356(6337). https://doi.org/10.1126/science.aaj2239.
44. Suzuki, T., Maeda, S., Furuhata, E., Shimizu, Y., Nishimura, H., Kishima, M., & Suzuki, H. (2017). A screening system to identify transcription factors that induce binding site-directed DNA demethylation. Epigenetics & Chromatin, 10(1), 60. https://doi.org/10.1186/s13072-017-0169-6.
45. Yang, J., Zhang, X., Blumenthal, R. M., & Cheng, X. (2020). Detection of DNA Modifications by Sequence-Specific Transcription Factors. Journal of Molecular Biology, 432(6), 1661–1673. https://doi.org/10.1016/j.jmb.2019.09.013.
46. Spruijt, C. G., Gnerlich, F., Smits, A. H., Pfaffeneder, T., Jansen, P. W. T. C., Bauer, C., Münzel, M., Wagner, M., Müller, M., Khan, F., Eberl, H. C., Mensinga, A., Brinkman, A. B., Lephikov, K., Müller, U., Walter, J., Boelens, R., van Ingen, H., Leonhardt, H., … Vermeulen, M. (2013). Dynamic Readers for 5-(Hydroxy)Methylcytosine and Its Oxidized Derivatives. Cell, 152(5), 1146–1159. https://doi.org/10.1016/j.cell.2013.02.004
47. Wu, X., & Zhang, Y. (2017). TET-mediated active DNA demethylation: mechanism, function and beyond. Nature Reviews Genetics, 18(9), 517–534. https://doi.org/10.1038/nrg.2017.33.

48. Turcan, S., Rohle, D., Goenka, A., Walsh, L. A., Fang, F., Yilmaz, E., Campos, C., Fabius, A. W. M., Lu, C., Ward, P. S., Thompson, C. B., Kaufman, A., Guryanova, O., Levine, R., Heguy, A., Viale, A., Morris, L. G. T., Huse, J. T., Mellinghoff, I. K., & Chan, T. A. (2012). IDH1 mutation is sufficient to establish the glioma hypermethylator phenotype. Nature, 483(7390), 479–483. https://doi.org/10.1038/nature10866.
49. Tewari, M., Khan, M., Verma, M., Coppens, J., Kemp, J. M., Bucholz, R., Mercier, P., & Egan, T. M. (2021). Physiology of Cultured Human Microglia Maintained in a Defined Culture Medium. ImmunoHorizons, 5(4), 257–272. https://doi.org/10.4049/immunohorizons.2000101.
50. Pidsley, R., Zotenko, E., Peters, T. J., Lawrence, M. G., Risbridger, G. P., Molloy, P., van Djik, S., Muhlhausler, B., Stirzaker, C., & Clark, S. J. (2016). Critical evaluation of the Illumina MethylationEPIC BeadChip microarray for whole-genome DNA methylation profiling. Genome Biology, 17(1), 208. https://doi.org/10.1186/s13059-016-1066-1.
51. Ginno, P. A., Gaidatzis, D., Feldmann, A., Hoerner, L., Imanci, D., Burger, L., Zilbermann, F., Peters, A. H. F. M., Edenhofer, F., Smallwood, S. A., Krebs, A. R., & Schübeler, D. (2020). A genome-scale map of DNA methylation turnover identifies site-specific dependencies of DNMT and TET activity. Nature Communications, 11(1), 2680. https://doi.org/10.1038/s41467-020-16354-x.
52. Sun, Z., Vaisvila, R., Hussong, L.-M., Yan, B., Baum, C., Saleh, L., Samaranayake, M., Guan, S., Dai, N., Corrêa, I. R., Pradhan, S., Davis, T. B., Evans, T. C., & Ettwiller, L. M. (2021). Nondestructive enzymatic deamination enables single-molecule long-read amplicon sequencing for the determination of 5-methylcytosine and 5-hydroxymethylcytosine at single-base resolution. Genome Research, *31*(2), 291–300. https://doi.org/10.1101/gr.265306.120.
53. Yu, M., Hon, G. C., Szulwach, K. E., Song, C.-X., Zhang, L., Kim, A., Li, X., Dai, Q., Shen, Y., Park, B., Min, J.-H., Jin, P., Ren, B., & He, C. (2012). Base-Resolution Analysis of 5-Hydroxymethylcytosine in the Mammalian Genome. Cell, 149(6), 1368–1380. https://doi.org/10.1016/j.cell.2012.04.027.

54. Kaikkonen, M. U., Spann, N. J., Heinz, S., Romanoski, C. E., Allison, K. A., Stender, J. D., Chun, H. B., Tough, D. F., Prinjha, R. K., Benner, C., & Glass, C. K. (2013). Remodeling of the Enhancer Landscape during Macrophage Activation Is Coupled to Enhancer Transcription. Molecular Cell, 51(3), 310–325. https://doi.org/10.1016/j.molcel.2013.07.010.
55. Spitzer, A., Gritsch, S., Nomura, M., Jucht, A., Fortin, J., Raviram, R., Weisman, H. R., Gonzalez Castro, L. N., Druck, N., Chanoch-Myers, R., Lee, J. J. Y., Mylvaganam, R., Lee Servis, R., Fung, J. M., Lee, C. K., Nagashima, H., Miller, J. J., Arrillaga-Romany, I., Louis, D. N., … Tirosh, I. (2024). Mutant IDH inhibitors induce lineage differentiation in IDH-mutant oligodendroglioma. Cancer Cell, 42(5), 904-914.e9. https://doi.org/10.1016/j.ccell.2024.03.008.
56. Lund, H., Pieber, M., Parsa, R., Han, J., Grommisch, D., Ewing, E., Kular, L., Needhamsen, M., Espinosa, A., Nilsson, E., Överby, A. K., Butovsky, O., Jagodic, M., Zhang, X.-M., & Harris, R. A. (2018). Competitive repopulation of an empty microglial niche yields functionally distinct subsets of microglia-like cells. Nature Communications, 9(1), 4845. https://doi.org/10.1038/s41467-018-07295-7.
57. Keshet, I., Lieman-Hurwitz, J., & Cedar, H. (1986). DNA methylation affects the formation of active chromatin. Cell, 44(4), 535–543. https://doi.org/10.1016/0092-8674(86)90263-1.
58. Lee, J. Y., & Lee, T.-H. (2012). Effects of DNA Methylation on the Structure of Nucleosomes. Journal of the American Chemical Society, 134(1), 173–175. https://doi.org/10.1021/ja210273w.
59. Rao, S., Chiu, T.-P., Kribelbauer, J. F., Mann, R. S., Bussemaker, H. J., & Rohs, R. (2018). Systematic prediction of DNA shape changes due to CpG methylation explains epigenetic effects on protein–DNA binding. Epigenetics & Chromatin, 11(1), 6. https://doi.org/10.1186/s13072-018-0174-4.
60. Kreibich, E., Kleinendorst, R., Barzaghi, G., Kaspar, S., & Krebs, A. R. (2023). Single-molecule footprinting identifies context-dependent regulation of enhancers by DNA

methylation. Molecular Cell, 83(5), 787-802.e9. https://doi.org/10.1016/j.molcel.2023.01.017.

61. Luoto, S., Hermelo, I., Vuorinen, E. M., Hannus, P., Kesseli, J., Nykter, M., & Granberg, K. J. (2018). Computational Characterization of Suppressive Immune Microenvironments in Glioblastoma. Cancer Research, 78(19), 5574–5585. https://doi.org/10.1158/0008-5472.CAN-17-3714.
62. Nott, A., Holtman, I. R., Coufal, N. G., Schlachetzki, J. C. M., Yu, M., Hu, R., Han, C. Z., Pena, M., Xiao, J., Wu, Y., Keulen, Z., Pasillas, M. P., O'Connor, C., Nickl, C. K., Schafer, S. T., Shen, Z., Rissman, R. A., Brewer, J. B., Gosselin, D., … Glass, C. K. (2019). Brain cell type–specific enhancer–promoter interactome maps and disease - risk association. Science, 366(6469), 1134–1139. https://doi.org/10.1126/science.aay0793.
63. Cheng, S.-C., Quintin, J., Cramer, R. A., Shepardson, K. M., Saeed, S., Kumar, V., Giamarellos-Bourboulis, E. J., Martens, J. H. A., Rao, N. A., Aghajanirefah, A., Manjeri, G. R., Li, Y., Ifrim, D. C., Arts, R. J. W., van der Veer, B. M. J. W., Deen, P. M. T., Logie, C., O'Neill, L. A., Willems, P., … Netea, M. G. (2014). mTOR- and HIF-1α–mediated aerobic glycolysis as metabolic basis for trained immunity. Science, 345(6204). https://doi.org/10.1126/science.1250684.
64. Palsson-McDermott, E. M., Curtis, A. M., Goel, G., Lauterbach, M. A. R., Sheedy, F. J., Gleeson, L. E., van den Bosch, M. W. M., Quinn, S. R., Domingo-Fernandez, R., Johnston, D. G. W., Jiang, J., Israelsen, W. J., Keane, J., Thomas, C., Clish, C., Vander Heiden, M., Xavier, R. J., & O'Neill, L. A. J. (2015). Pyruvate Kinase M2 Regulates Hif-1α Activity and IL-1β Induction and Is a Critical Determinant of the Warburg Effect in LPS-Activated Macrophages. Cell Metabolism, 21(1), 65–80. https://doi.org/10.1016/j.cmet.2014.12.005.
65. Corcoran, S. E., & O'Neill, L. A. J. (2016). HIF1α and metabolic reprogramming in inflammation. Journal of Clinical Investigation, 126(10), 3699–3707. https://doi.org/10.1172/JCI84431.

66. Sangineto, M., Ciarnelli, M., Cassano, T., Radesco, A., Moola, A., Bukke, V. N., Romano, A., Villani, R., Kanwal, H., Capitanio, N., Duda, L., Avolio, C., & Serviddio, G. (2023). Metabolic reprogramming in inflammatory microglia indicates a potential way of targeting inflammation in Alzheimer's disease. Redox Biology, 66, 102846. https://doi.org/10.1016/j.redox.2023.102846.
67. Chesnelong, C., Chaumeil, M. M., Blough, M. D., Al-Najjar, M., Stechishin, O. D., Chan, J. A., Pieper, R. O., Ronen, S. M., Weiss, S., Luchman, H. A., & Cairncross, J. G. (2014). Lactate dehydrogenase A silencing in IDH mutant gliomas. Neuro-Oncology, 16(5), 686–695. https://doi.org/10.1093/neuonc/not243.
68. Koivunen, P., Lee, S., Duncan, C. G., Lopez, G., Lu, G., Ramkissoon, S., Losman, J. A., Joensuu, P., Bergmann, U., Gross, S., Travins, J., Weiss, S., Looper, R., Ligon, K. L., Verhaak, R. G. W., Yan, H., & Kaelin Jr, W. G. (2012). Transformation by the (R)-enantiomer of 2-hydroxyglutarate linked to EGLN activation. Nature, 483(7390), 484–488. https://doi.org/10.1038/nature10898
69. Lavin, Y., Winter, D., Blecher-Gonen, R., David, E., Keren-Shaul, H., Merad, M., Jung, S., & Amit, I. (2014). Tissue-Resident Macrophage Enhancer Landscapes Are Shaped by the Local Microenvironment. Cell, 159(6), 1312–1326. https://doi.org/10.1016/j.cell.2014.11.018.
70. Gosselin, D., Link, V. M., Romanoski, C. E., Fonseca, G. J., Eichenfield, D. Z., Spann, N. J., Stender, J. D., Chun, H. B., Garner, H., Geissmann, F., & Glass, C. K. (2014). Environment Drives Selection and Function of Enhancers Controlling Tissue-Specific Macrophage Identities. Cell, 159(6), 1327–1340. https://doi.org/10.1016/j.cell.2014.11.023.
71. Troutman, T. D., Kofman, E., & Glass, C. K. (2021). Exploiting dynamic enhancer landscapes to decode macrophage and microglia phenotypes in health and disease. Molecular Cell, 81(19), 3888–3903. https://doi.org/10.1016/j.molcel.2021.08.004.
72. Parry, A., Rulands, S., & Reik, W. (2021). Active turnover of DNA methylation during cell fate decisions. Nature Reviews Genetics, 22(1), 59–66. https://doi.org/10.1038/s41576-020-00287-8.

73. Onodera, A., González-Avalos, E., Lio, C.-W. J., Georges, R. O., Bellacosa, A., Nakayama, T., & Rao, A. (2021). Roles of TET and TDG in DNA demethylation in proliferating and non-proliferating immune cells. Genome Biology, 22(1), 186. https://doi.org/10.1186/s13059-021-02384-1.
74. Vats, D., Mukundan, L., Odegaard, J. I., Zhang, L., Smith, K. L., Morel, C. R., Greaves, D. R., Murray, P. J., & Chawla, A. (2006). Oxidative metabolism and PGC-1β attenuate macrophage-mediated inflammation. Cell Metabolism, 4(1), 13–24. https://doi.org/10.1016/j.cmet.2006.05.011.
75. Huang, S. C.-C., Everts, B., Ivanova, Y., O'Sullivan, D., Nascimento, M., Smith, A. M., Beatty, W., Love-Gregory, L., Lam, W. Y., O'Neill, C. M., Yan, C., Du, H., Abumrad, N. A., Urban, J. F., Artyomov, M. N., Pearce, E. L., & Pearce, E. J. (2014). Cell-intrinsic lysosomal lipolysis is essential for alternative activation of macrophages. Nature Immunology, 15(9), 846–855. https://doi.org/10.1038/ni.2956.
76. Sabogal-Guáqueta, A. M., Marmolejo-Garza, A., Trombetta-Lima, M., Oun, A., Hunneman, J., Chen, T., Koistinaho, J., Lehtonen, S., Kortholt, A., Wolters, J. C., Bakker, B. M., Eggen, B. J. L., Boddeke, E., & Dolga, A. (2023). Species-specific metabolic reprogramming in human and mouse microglia during inflammatory pathway induction. Nature Communications, 14(1), 6454. https://doi.org/10.1038/s41467-023-42096-7.
77. Han, C., Zheng, J., Sun, L., Yang, H., Cao, Z., Zhang, X., Zheng, L., & Zhen, X. (2019). The oncometabolite 2-hydroxyglutarate inhibits microglial activation via the AMPK/mTOR/NF-κB pathway. Acta Pharmacologica Sinica, 40(10), 1292–1302. https://doi.org/10.1038/s41401-019-0225-9.
78. Mellinghoff, I. K., Lu, M., Wen, P. Y., Taylor, J. W., Maher, E. A., Arrillaga-Romany, I., Peters, K. B., Ellingson, B. M., Rosenblum, M. K., Chun, S., Le, K., Tassinari, A., Choe, S., Toubouti, Y., Schoenfeld, S., Pandya, S. S., Hassan, I., Steelman, L., Clarke, J. L., & Cloughesy, T. F. (2023). Vorasidenib and ivosidenib in IDH1-mutant low-grade glioma: a randomized, perioperative phase 1 trial. Nature Medicine, 29(3), 615–622. https://doi.org/10.1038/s41591-022-02141-2.

79. di Stefano, A. L., Picca, A., Saragoussi, E., Bielle, F., Ducray, F., Villa, C., Eoli, M., Paterra, R., Bellu, L., Mathon, B., Capelle, L., Bourg, V., Gloaguen, A., Philippe, C., Frouin, V., Schmitt, Y., Lerond, J., Leclerc, J., Lasorella, A., … Sanson, M. (2020). Clinical, molecular, and radiomic profile of gliomas with FGFR3-TACC3 fusions. Neuro-Oncology, 22(11), 1614–1624. https://doi.org/10.1093/neuonc/noaa121.
80. Teschendorff, A. E. (2020). A comparison of epigenetic mitotic-like clocks for cancer risk prediction. Genome Medicine, 12(1), 56. https://doi.org/10.1186/s13073-020-00752-3.
81. Heinz, S., Benner, C., Spann, N., Bertolino, E., Lin, Y. C., Laslo, P., Cheng, J. X., Murre, C., Singh, H., & Glass, C. K. (2010). Simple Combinations of Lineage-Determining Transcription Factors Prime cis-Regulatory Elements Required for Macrophage and B Cell Identities. Molecular Cell, 38(4), 576–589. https://doi.org/10.1016/j.molcel.2010.05.004.
82. Vorontsov, I. E., Eliseeva, I. A., Zinkevich, A., Nikonov, M., Abramov, S., Boytsov, A., Kamenets, V., Kasianova, A., Kolmykov, S., Yevshin, I. S., Favorov, A., Medvedeva, Y. A., Jolma, A., Kolpakov, F., Makeev, V. J., & Kulakovskiy, I. V. (2024). HOCOMOCO in 2024: a rebuild of the curated collection of binding models for human and mouse transcription factors. Nucleic Acids Research, 52(D1), D154–D163. https://doi.org/10.1093/nar/gkad1077.
83. Balss, J., Pusch, S., Beck, A.-C., Herold-Mende, C., Krämer, A., Thiede, C., Buckel, W., Langhans, C.-D., Okun, J. G., & von Deimling, A. (2012). Enzymatic assay for quantitative analysis of (d)-2-hydroxyglutarate. Acta Neuropathologica, 124(6), 883–891. https://doi.org/10.1007/s00401-012-1060-y.
84. Ewing, A. D., Smits, N., Sanchez-Luque, F. J., Faivre, J., Brennan, P. M., Richardson, S. R., Cheetham, S. W., & Faulkner, G. J. (2020). Nanopore Sequencing Enables Comprehensive Transposable Element Epigenomic Profiling. Molecular Cell, 80(5), 915-928.e5. https://doi.org/10.1016/j.molcel.2020.10.024.
85. Akalin, A., Kormaksson, M., Li, S., Garrett-Bakelman, F. E., Figueroa, M. E., Melnick, A., & Mason, C. E. (2012). methylKit: a comprehensive R package for the analysis of

genome-wide DNA methylation profiles. Genome Biology, 13(10), R87. https://doi.org/10.1186/gb-2012-13-10-r87

86. Pagès H, Aboyoun P, Gentleman R, DebRoy S (2024). Biostrings: Efficient manipulation of biological strings. R package version 2.72.0, https://bioconductor.org/packages/Biostrings
87. Schmittgen, T. D., & Livak, K. J. (2008). Analyzing real-time PCR data by the comparative CT method. Nature Protocols, 3(6), 1101–1108. https://doi.org/10.1038/nprot.2008.73.
88. Hao, Y., Stuart, T., Kowalski, M. H., Choudhary, S., Hoffman, P., Hartman, A., Srivastava, A., Molla, G., Madad, S., Fernandez-Granda, C., & Satija, R. (2024). Dictionary learning for integrative, multimodal and scalable single-cell analysis. Nature Biotechnology, 42(2), 293–304. https://doi.org/10.1038/s41587-023-01767-y.
89. Wickham, H., & Wickham, H. (2016). Data analysis (pp. 189-201). Springer International Publishing. doi.org/10.1007/978-3-319-24277-4_9.
90. Ahlmann-Eltze, C., & Patil, I. (2021). ggsignif: R Package for Displaying Significance Brackets for 'ggplot2'. PsyArxiv. doi.org/10.31234/osf.io/7awm6.
91. Gu, Z. (2022). Complex Heatmap Visualization, iMeta. doi.org/10.1002/imt2.43.
92. Shannon, P., Markiel, A., Ozier, O., Baliga, N. S., Wang, J. T., Ramage, D., ... & Ideker, T. (2003). Cytoscape: a software environment for integrated models of biomolecular interaction networks. Genome research, 13(11), 2498-2504. doi.org/10.1101/gr.1239303.
93. Wu, T., Hu, E., Xu, S., Chen, M., Guo, P., Dai, Z., ... & Yu, G. (2021). clusterProfiler 4.0: A universal enrichment tool for interpreting omics data. The innovation, 2(3). doi.org/10.1016/j.xinn.2021.100141.
94. Larsson J. (2024). eulerr: Area-Proportional Euler and Venn Diagrams with Ellipses. R package version 7.0.0, https://CRAN.R-project.org/package=eulerr.
95. Subramanian, A., Tamayo, P., Mootha, V. K., Mukherjee, S., Ebert, B. L., Gillette, M. A., ... & Mesirov, J. P. (2005). Gene set enrichment analysis: a knowledge-based approach for interpreting genome-wide expression profiles. Proceedings of the

National Academy of Sciences, 102(43), 15545-15550. doi.org/10.1073/pnas.0506580102.

96. Liberzon, A., Birger, C., Thorvaldsdóttir, H., Ghandi, M., Mesirov, J. P., & Tamayo, P. (2015). The molecular signatures database hallmark gene set collection. Cell systems, 1(6), 417-425. doi.org/10.1016/j.cels.2015.12.004.
97. Khanna, A., Larson, D., Srivatsan, S., Mosior, M., Abbott, T., Kiwala, S., ... & Miller, C. (2022). Bam-readcount - rapid generation of basepair-resolution sequence metrics. The Journal of Open Source Software, 7(69), 3722. doi.org/10.21105/joss.03722.
98. Aaronson, J., Beaumont, V., Blevins, R. A., Andreeva, V., Murasheva, I., Shneyderman, A., ... & Vogt, T. F. (2021). HDinHD: A rich data portal for Huntington's disease research. Journal of Huntington's Disease, 10(3), 405-412. doi.org/10.3233/JHD-210491.

Supplementary Figures

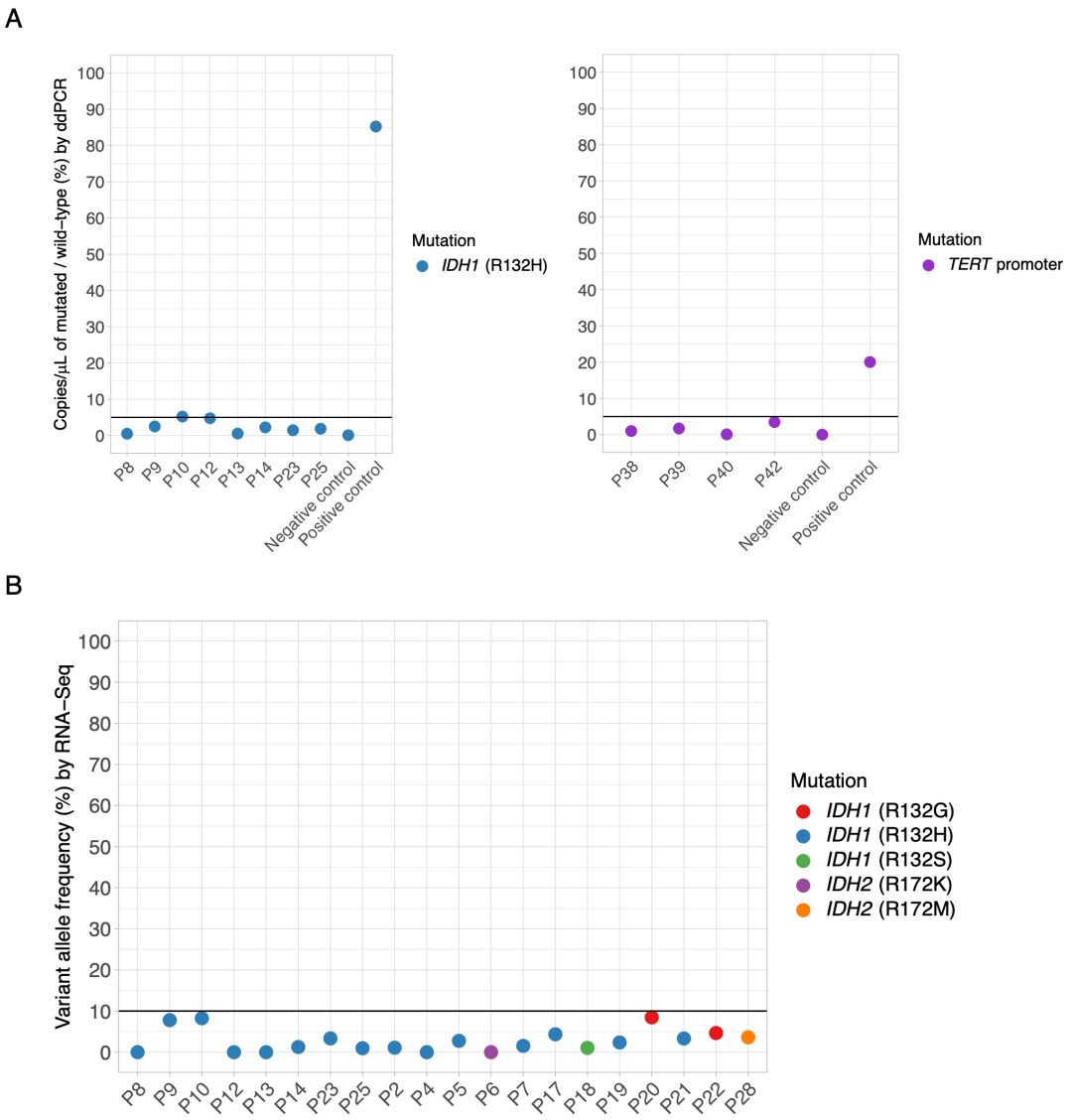

Supplementary Fig. S1. Purity of CD11B+ myeloid fractions isolated from human gliomas. (A) Digital droplet PCR (ddPCR) performed with specific assays to evaluate IDH1 R132H, TERT promoter mutations C228T/C250T, and the corresponding wild-type alleles in available DNAs from CD11B+ samples (n=12) isolated from human gliomas with known mutation status. Less than 5% copies/µL of the indicated mutations relative to their corresponding wild-type alleles were detected in the same reaction for each analyzed sample. Positive and negative controls from bulk tumors for each assay are also shown. The detection of IDHmut and TERT mutations in positive controls differed, possibly reflecting regional clonal heterogeneity. **(B)** Expression frequency of IDH-mutated alleles was assessed in RNA-seq data from CD11B+ samples (n=20) isolated from human gliomas with a known mutation status using bam-readcount[97]. Compared to ddPCR, this analysis slightly overestimated the contamination in samples P9 and P10.

A

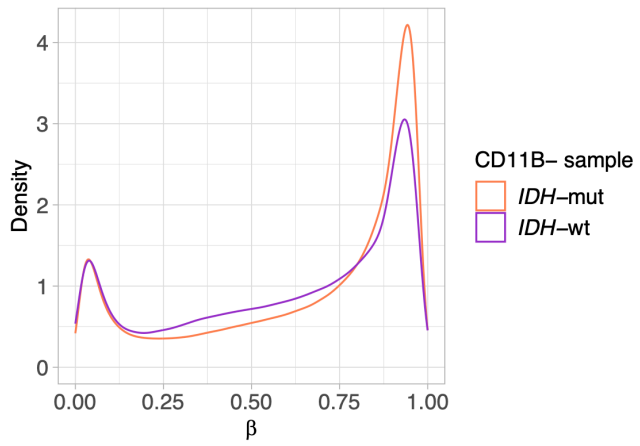
Density
β
CD11B– sample
IDH–mut
IDH–wt

B

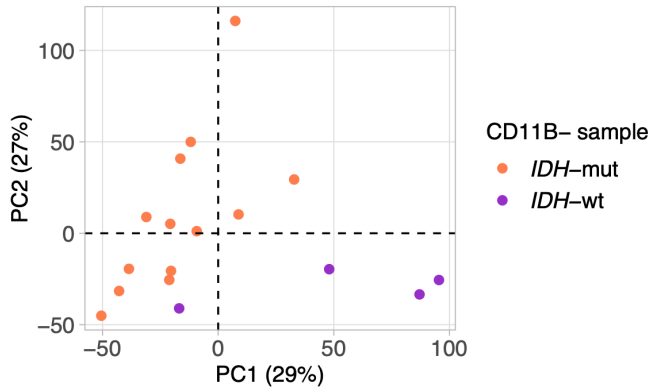
PC2 (27%)
PC1 (29%)
CD11B– sample
IDH–mut
IDH–wt

C

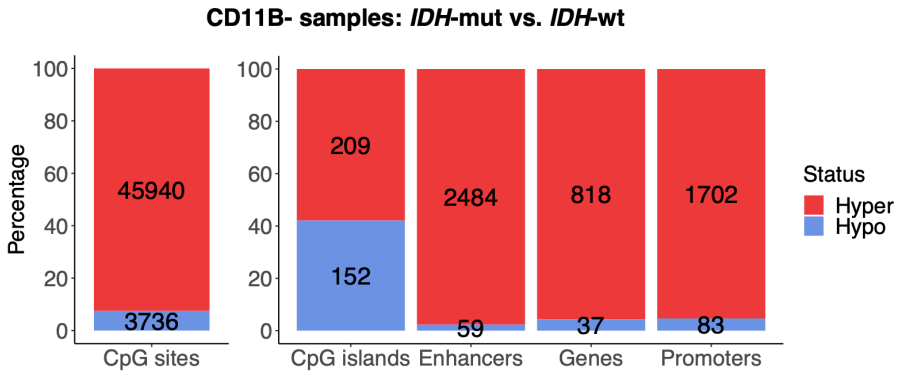
CD11B- samples: IDH-mut vs. IDH-wt
Percentage
45940
3736
209
152
2484
59
818
37
1702
83
CpG sites
CpG islands
Enhancers
Genes
Promoters
Status
Hyper
Hypo

D

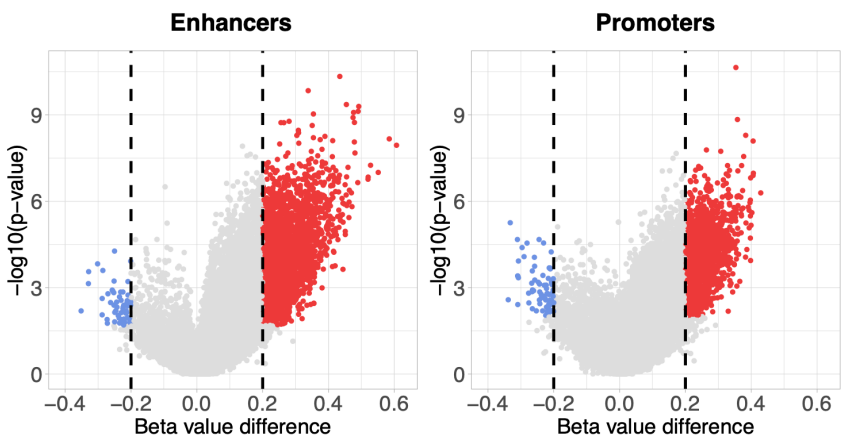
Enhancers
Promoters
−log10(p−value)
Beta value difference

Supplementary Fig. S2. CD11B- fractions enriched of glioma cells display global DNA hypermethylation in IDH^{mut} gliomas. (A) Density plot of DNA methylation levels (β-values) in glioma cells-enriched CD11B- fractions isolated from IDH^{mut} (n=13) and IDH^{wt} (n=4) tumors. **(B)** Principal component analysis was performed using methylome data from approximately 600,000 CpG sites across the genome in CD11B- samples from the study cohort. **(C)** Stacked bar charts show absolute numbers and relative percentages of CpG sites and four functional genomic regions with respect to the methylation status in CD11B- samples from IDH^{mut} vs. IDH^{wt} tumors. **(D)** Volcano plots depicting the magnitude and extent of differentially methylated changes (red and blue) located at enhancers and promoters in CD11B- samples from IDH^{mut} vs. IDH^{wt} tumors.

A

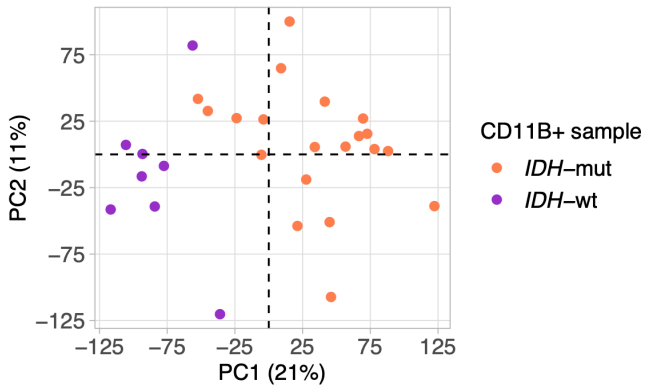
75
25
−25
−75
−125
PC2 (11%)
−125
−75
−25
25
75
125
PC1 (21%)
CD11B+ sample
IDH–mut
IDH–wt

B

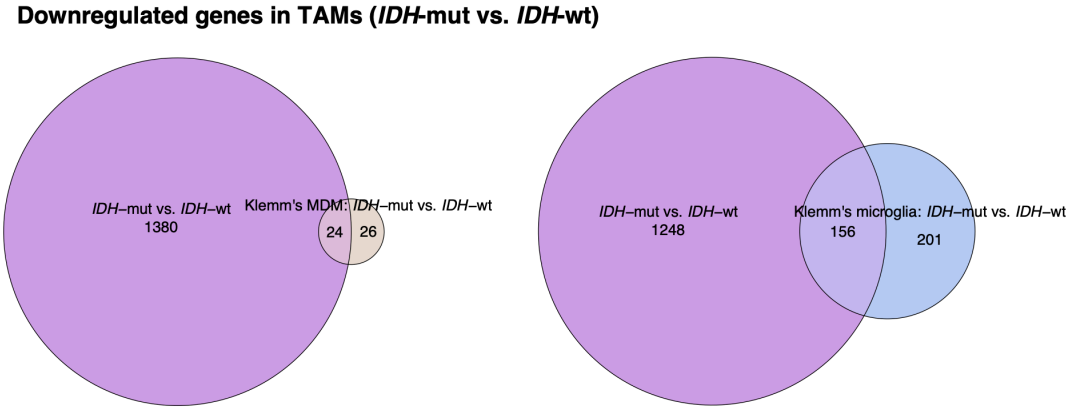
Downregulated genes in TAMs (IDH-mut vs. IDH-wt)
IDH–mut vs. IDH–wt
1380
Klemm's MDM: IDH–mut vs. IDH–wt
24
26
IDH–mut vs. IDH–wt
1248
Klemm's microglia: IDH–mut vs. IDH–wt
156
201

C

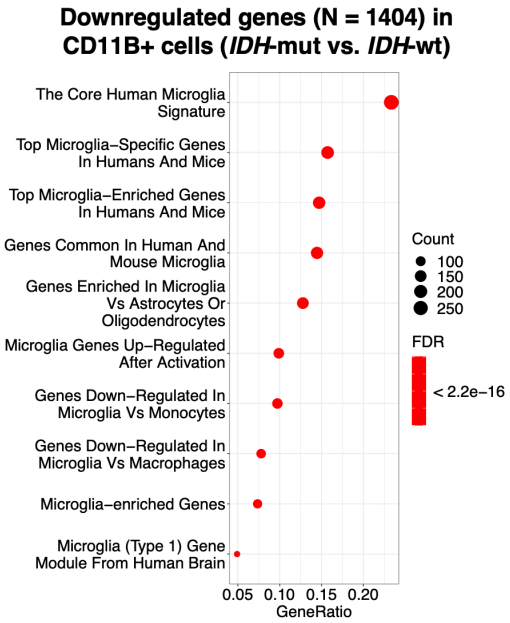
Downregulated genes (N = 1404) in CD11B+ cells (IDH-mut vs. IDH-wt)
The Core Human Microglia Signature
Top Microglia–Specific Genes In Humans And Mice
Top Microglia–Enriched Genes In Humans And Mice
Genes Common In Human And Mouse Microglia
Genes Enriched In Microglia Vs Astrocytes Or Oligodendrocytes
Microglia Genes Up–Regulated After Activation
Genes Down–Regulated In Microglia Vs Monocytes
Genes Down–Regulated In Microglia Vs Macrophages
Microglia–enriched Genes
Microglia (Type 1) Gene Module From Human Brain
0.05
0.10
0.15
0.20
GeneRatio
Count
100
150
200
250
FDR
< 2.2e−16

D

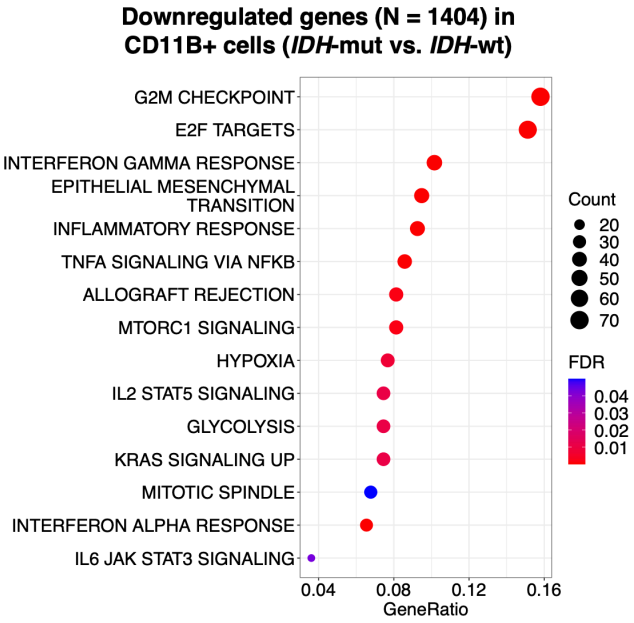
Downregulated genes (N = 1404) in CD11B+ cells (IDH-mut vs. IDH-wt)
G2M CHECKPOINT
E2F TARGETS
INTERFERON GAMMA RESPONSE
EPITHELIAL MESENCHYMAL TRANSITION
INFLAMMATORY RESPONSE
TNFA SIGNALING VIA NFKB
ALLOGRAFT REJECTION
MTORC1 SIGNALING
HYPOXIA
IL2 STAT5 SIGNALING
GLYCOLYSIS
KRAS SIGNALING UP
MITOTIC SPINDLE
INTERFERON ALPHA RESPONSE
IL6 JAK STAT3 SIGNALING
0.04
0.08
0.12
0.16
GeneRatio
Count
20
30
40
50
60
70
FDR
0.04
0.03
0.02
0.01

Supplementary Fig. S3. Genes with reduced expression in CD11B+ cells from IDH^{mut} human gliomas belong to microglial signatures. (A) Principal component analysis performed using RNA-seq data from *ex vivo* CD11B+ myeloid cells isolated from IDH^{mut} (n=20) and IDH^{wt} (n=8) tumors. **(B)** Venn diagrams illustrating significant overlap between downregulated genes displayed by CD11B+ cell fractions from IDH^{mut} gliomas (this study) and downregulated genes displayed by MDMs (left) or microglial cells (right) in the study by Klemm et al. P-values were computed using over-representation analysis (ORA). **(C)** Enrichment analysis of the downregulated genes in CD11B+ cell fractions from IDH^{mut} gliomas in the present study using the HDinHD microglia signature dataset[98]. **(D)** Enrichment analysis of downregulated genes in the CD11B+ cell fractions from IDH^{mut} gliomas (this study) using the hallmark signature dataset.

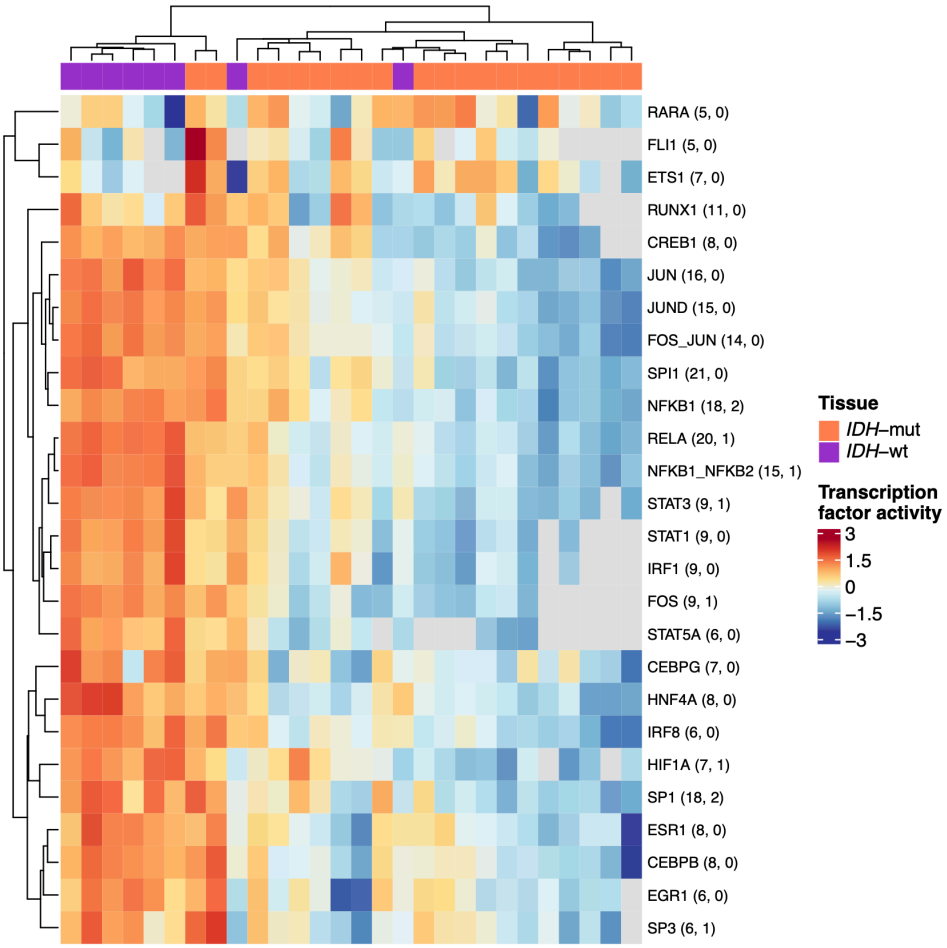

Supplementary Fig. S4. Transcription factors activity controlling genes with hypermethylated promoter in CD11B+ cells from human gliomas. The heatmap depicts TFs (n=26) exhibiting differential activity (FDR <0.05; Wilcoxon's test) in CD11B+ cells according to the IDH mutation status of the corresponding tumors. The TF targets used for this analysis, retrieved from the CollecTRI database, were searched among the genes displaying hypermethylation at promoters in the CD11B+ cell fractions from the IDH^{mut} vs. IDH^{wt} gliomas (Fig. 1D). The number of targets positively and negatively regulated by each TF is shown in parentheses. Unsupervised clustering was performed using z-scores of TF activity, where red and blue indicate high and low activity, respectively. Non-significant activity is shown in gray.

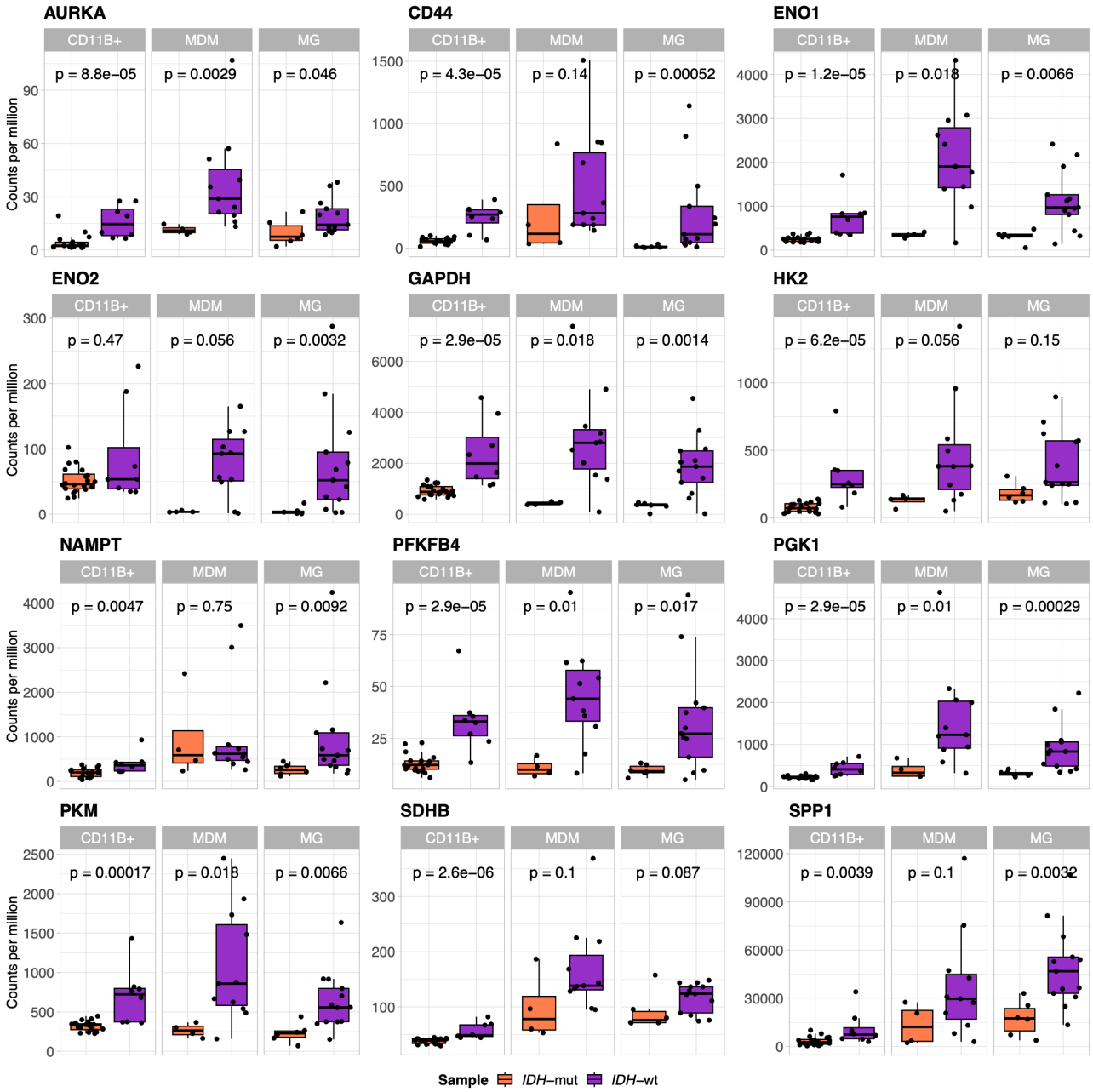

Supplementary Fig. S5. Positive targets of HIF1A/MYC display low expression in microglia and MDMs from IDH^{mut} gliomas. Box plots showing normalized RNA-seq expression data for representative targets of HIF1A/MYC in CD11B+ myeloid cells from the present study cohort (IDH^{mut}, n=20 vs. IDH^{wt}, n=8), as well as in myeloid cells from the study by Klemm et al., comprising MDMs (IDH^{mut}, n=4 vs. IDH^{wt}, n=11) and microglia (IDH^{mut}, n=6 vs. IDH^{wt}, n=13) used as validation set. P-values were computed using Wilcoxon's test.

A

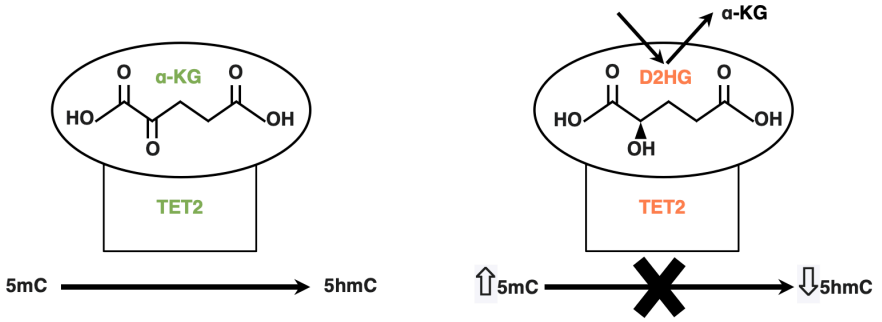
α-KG
HO
OH
TET2
5mC
5hmC
α-KG
D2HG
HO
OH
OH
TET2
5mC
5hmC

B

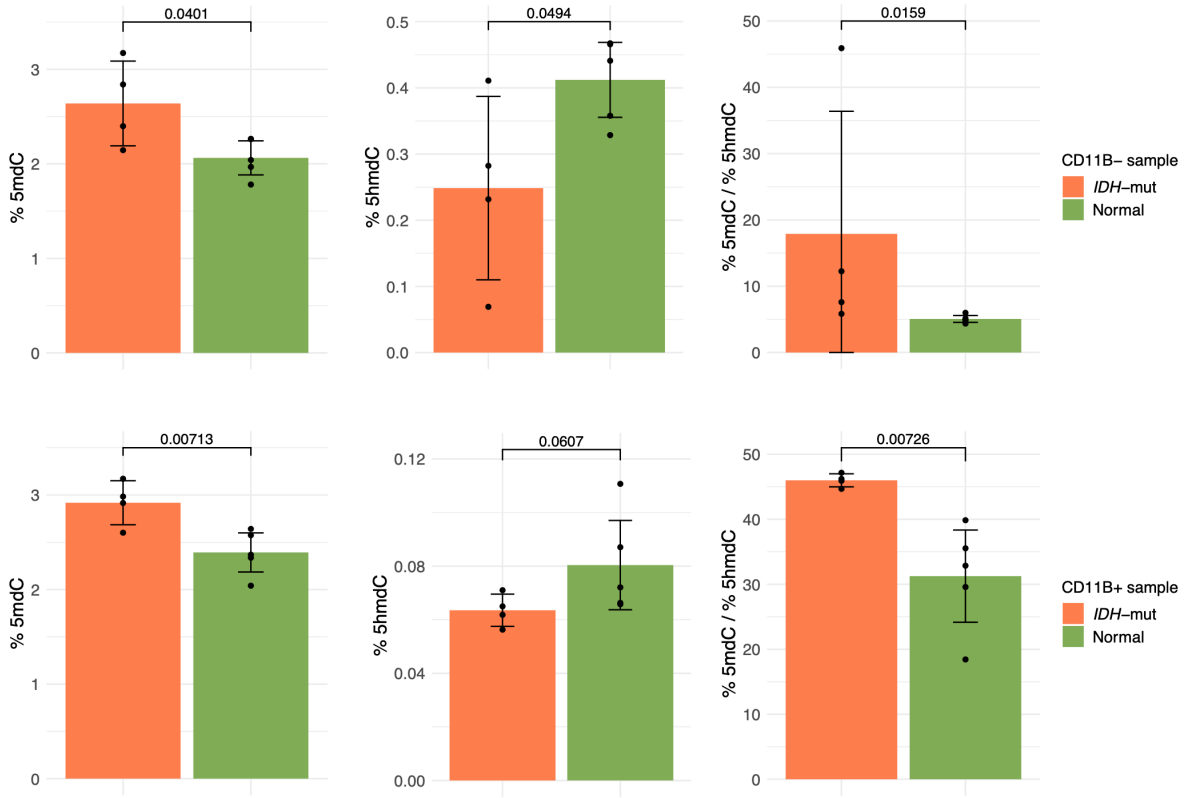
0.0401
% 5mdC
0.0494
% 5hmdC
0.0159
% 5mdC / % 5hmdC
CD11B– sample
IDH–mut
Normal
0.00713
% 5mdC
0.0607
% 5hmdC
0.00726
% 5mdC / % 5hmdC
CD11B+ sample
IDH–mut
Normal

C

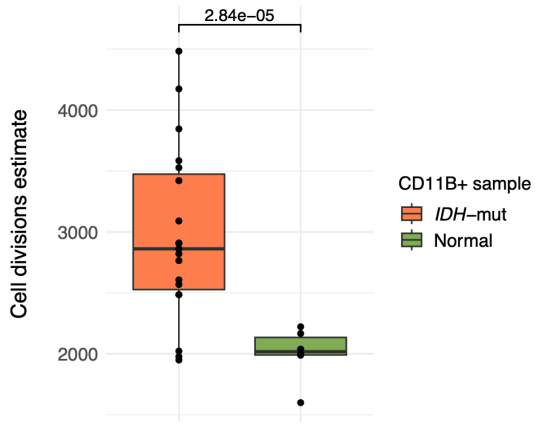
2.84e−05
Cell divisions estimate
CD11B+ sample
IDH–mut
Normal

Supplementary Fig. S6. LC-MS/MS analysis of 5mC and 5hmC genomic content and cell divisions estimate in CD11B+ myeloid cells from IDH^{mut} gliomas and normal brain tissues. **(A)** Schematic representation of α-KG-dependent enzymatic oxidation of 5mC by TET2 and the effect of competitive inhibition of TET2 by D-2HG over time in bulk IDH^{mut} gliomas. **(B)** Global levels of 5mC and 5hmC (left) and 5mC/5hmC ratios (right) were measured in the CD11B- (upper) and CD11B+ (bottom) fractions from IDH^{mut} gliomas (n=4) and normal tissues collected during epilepsy surgery (n=5), which served as controls for comparison. Data are represented as the mean with a 95% CI; p-values were calculated using one-sided Welch's test, except for the comparison of ratios in CD11B- (one-sided Wilcoxon's test). **(C)** Epigenetic mitotic clock analysis was conducted by applying the epiTOC2[80] model to the methylome data (EPIC arrays) of CD11B+ fractions from IDH^{mut} gliomas (n=19) and normal brain tissues (n=6). The model (adjusted for age) estimates the cumulative number of stem cell divisions in the myeloid compartment. The p-value was calculated using Welch's test.

A

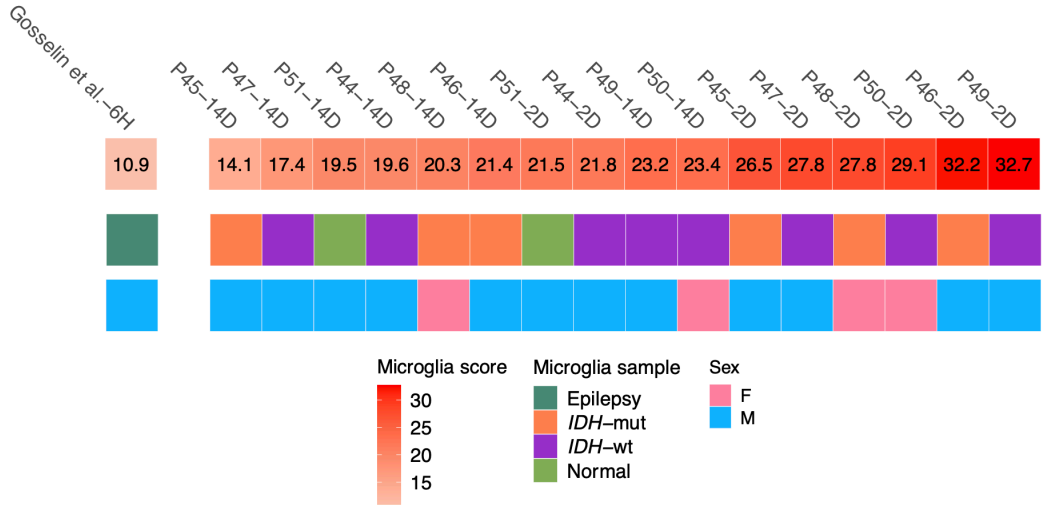
Gosselin et al.–6H
P45–14D
P47–14D
P51–14D
P44–14D
P48–14D
P46–14D
P51–2D
P44–2D
P49–14D
P50–14D
P45–2D
P47–2D
P48–2D
P50–2D
P46–2D
P49–2D
10.9
14.1
17.4
19.5
19.6
20.3
21.4
21.5
21.8
23.2
23.4
26.5
27.8
27.8
29.1
32.2
32.7
Microglia score
30
25
20
15
Microglia sample
Epilepsy
IDH–mut
IDH–wt
Normal
Sex
F
M

B

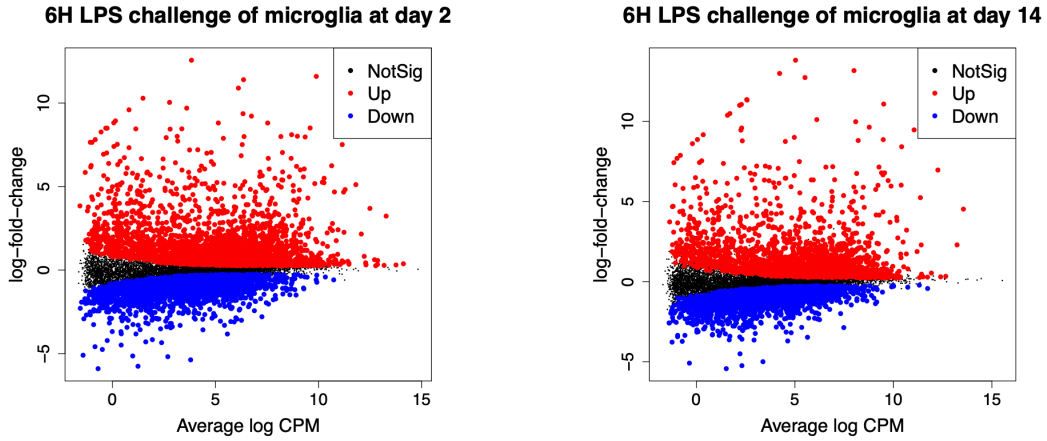
6H LPS challenge of microglia at day 2
6H LPS challenge of microglia at day 14
NotSig
Up
Down
log–fold–change
Average log CPM

C

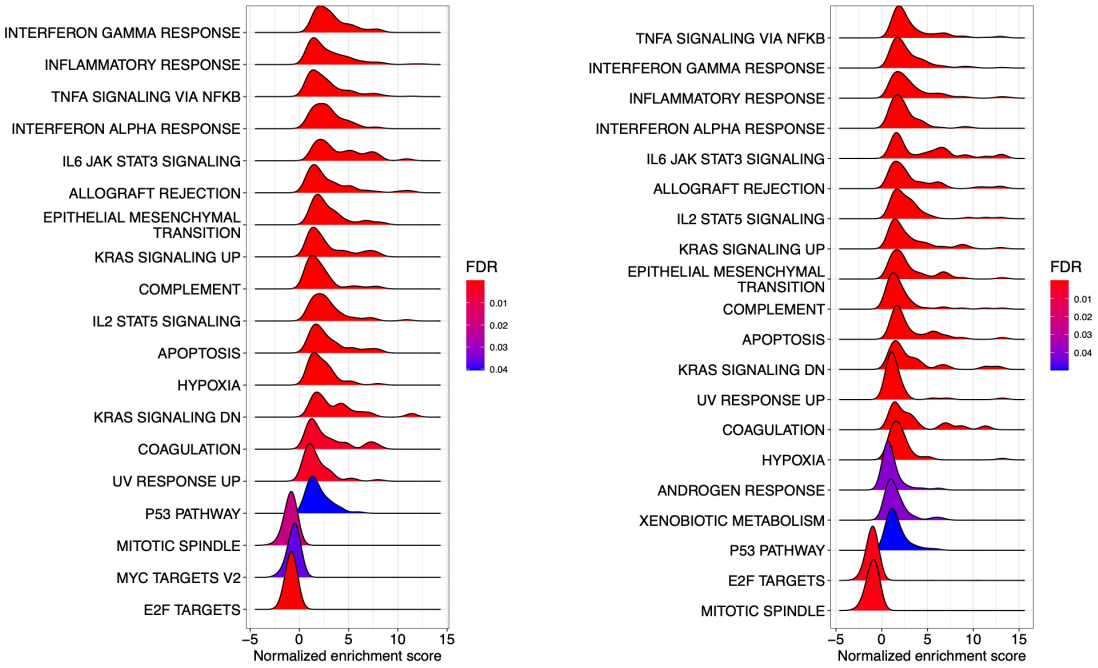
INTERFERON GAMMA RESPONSE
INFLAMMATORY RESPONSE
TNFA SIGNALING VIA NFKB
INTERFERON ALPHA RESPONSE
IL6 JAK STAT3 SIGNALING
ALLOGRAFT REJECTION
EPITHELIAL MESENCHYMAL TRANSITION
KRAS SIGNALING UP
COMPLEMENT
IL2 STAT5 SIGNALING
APOPTOSIS
HYPOXIA
KRAS SIGNALING DN
COAGULATION
UV RESPONSE UP
P53 PATHWAY
MITOTIC SPINDLE
MYC TARGETS V2
E2F TARGETS
FDR
Normalized enrichment score
TNFA SIGNALING VIA NFKB
INTERFERON GAMMA RESPONSE
INFLAMMATORY RESPONSE
INTERFERON ALPHA RESPONSE
IL6 JAK STAT3 SIGNALING
ALLOGRAFT REJECTION
IL2 STAT5 SIGNALING
KRAS SIGNALING UP
EPITHELIAL MESENCHYMAL TRANSITION
COMPLEMENT
APOPTOSIS
KRAS SIGNALING DN
UV RESPONSE UP
COAGULATION
HYPOXIA
ANDROGEN RESPONSE
XENOBIOTIC METABOLISM
P53 PATHWAY
E2F TARGETS
MITOTIC SPINDLE
FDR
Normalized enrichment score

Supplementary Fig. S7. Assessment of the functionality of primary microglial cultures. **(A)** Analysis of human microglial signatures at 2 days (2D) and 14 days (14D) using RNA-seq data from eight independent primary cultures. The microglial score was determined as follows: we used the microglia signature genes and the raw gene expression matrix from Gosselin et al[39]. Subsequently, after normalizing the expression data, we calculated the median of the differences in each gene from the microglial signature in our samples with respect to the five negative samples used as controls in the study by Gosselin et al. The microglia score was defined as the average of five medians. The plot (upper), showing the microglia score per sample, demonstrates that the signature is nearly twice as high, even after 14 days of culture, when using defined culture conditions (as in our study), compared to the study by Gosselin et al. (culture shock at 6 h), irrespective of tissue origin and sex (as indicated at the bottom). **(B)** The plots illustrate expression changes using four primary microglial cultures analyzed by RNA-seq in a paired manner 6 h after LPS stimulation at 2 days (left) and 14 days (right). Red and blue colors indicate upregulation and downregulation, respectively, with FDR <0.05, in LPS-stimulated microglia vs. control. **(C)** Ridge plots illustrate hallmark gene set GSEA analyses in LPS-stimulated microglia after 2 days (left) and 14 days (right) of culture. Activated (>0) and inactivated (<0) gene sets with FDR < 0.05 are shown.

A

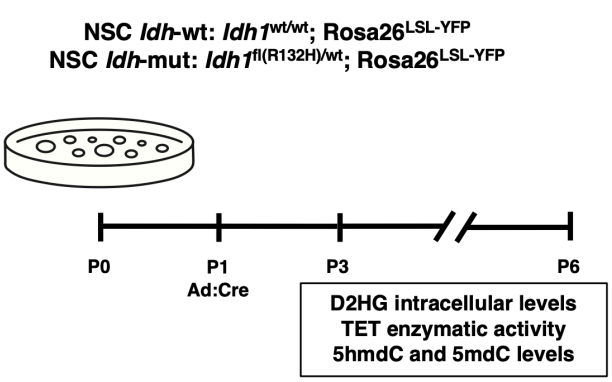
NSC *Idh*-wt: *Idh1*$^{wt/wt}$; Rosa26$^{LSL-YFP}$
NSC *Idh*-mut: *Idh1*$^{fl(R132H)/wt}$; Rosa26$^{LSL-YFP}$
P0
P1
Ad:Cre
P3
P6
D2HG intracellular levels
TET enzymatic activity
5hmdC and 5mdC levels

B

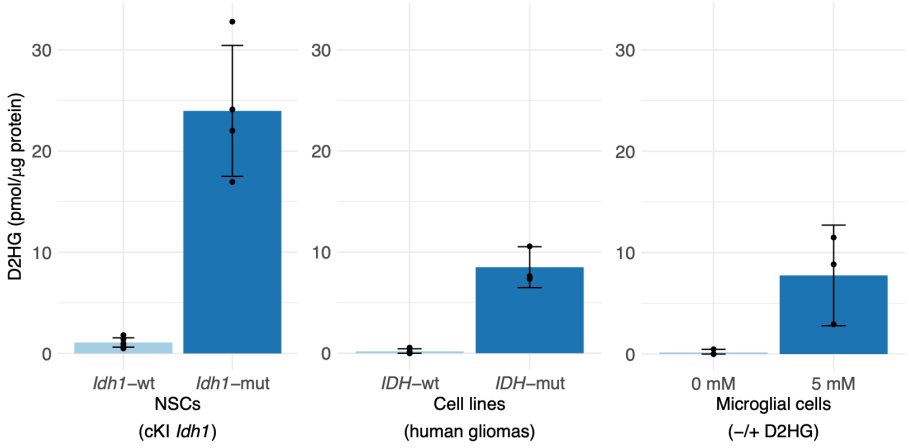
D2HG (pmol/µg protein)
30
20
10
0
Idh1–wt
Idh1–mut
NSCs
(cKI *Idh1*)
IDH–wt
IDH–mut
Cell lines
(human gliomas)
0 mM
5 mM
Microglial cells
(–/+ D2HG)

C

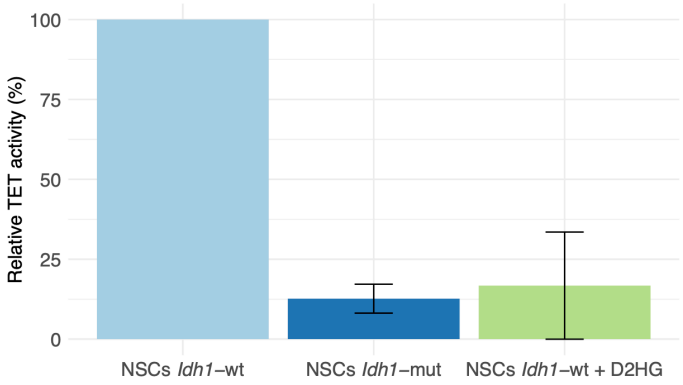
Relative TET activity (%)
100
75
50
25
0
NSCs *Idh1*–wt
NSCs *Idh1*–mut
NSCs *Idh1*–wt + D2HG

D

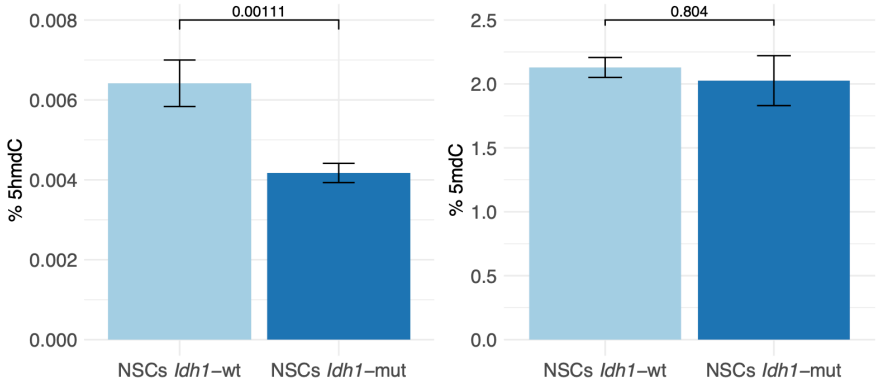
% 5hmdC
0.008
0.006
0.004
0.002
0.000
0.00111
NSCs *Idh1*–wt
NSCs *Idh1*–mut
% 5mdC
2.5
2.0
1.5
1.0
0.5
0.0
0.804
NSCs *Idh1*–wt
NSCs *Idh1*–mut

Supplementary Fig. S8. Assessment of D-2HG levels and TET function in external controls. (A) Workflow procedure for inducing the *in vitro* expression of Idh1 R132H in neural progenitor cells (NSCs) obtained from a conditional knock-in IDH^{mut} mouse model (cKI Idh1) used as an external isogenic control in three assays. Cells collected on day 14 for analyses underwent 3-6 passages. **(B)** Intracellular levels of D-2HG were determined using a fluorometric assay in primary microglia treated with D-2HG [5 mM] for 48 h. Microglia were obtained from samples with IDH^{wt} status (n=3). External controls for comparison (cKI model Idhwt n=5; Idhmut n=4, and patient-derived glioma cells IDH^{wt} n=4; IDH^{mut} n=3) are also shown. The levels of D-2HG in each sample were normalized to the corresponding micrograms of protein to enable comparisons among cell types. Data are presented as the mean with 95% CI. **(C)** TET enzymatic activity was assessed in nuclear extracts from NSCs after 14 days of culture. The plot shows a dramatic reduction in TET activity in IDH^{mut} cells compared with that in the IDH^{wt} control. Data are presented as the mean with a 95% CI from technical replicates (n=2). A negative internal control consisting of D-2HG at a final concentration of 400 µM was added to the IDH^{wt} extract during the assay (green color). **(D)** Quantification of 5hmC and 5mC global levels determined by LC-MS/MS in IDH^{mut} and IDH^{wt} NSCs controls after 14 days of culture. Data are presented as mean with 95% CI from technical replicates (n=4). P-values were calculated using one-sided Welch's test.

A

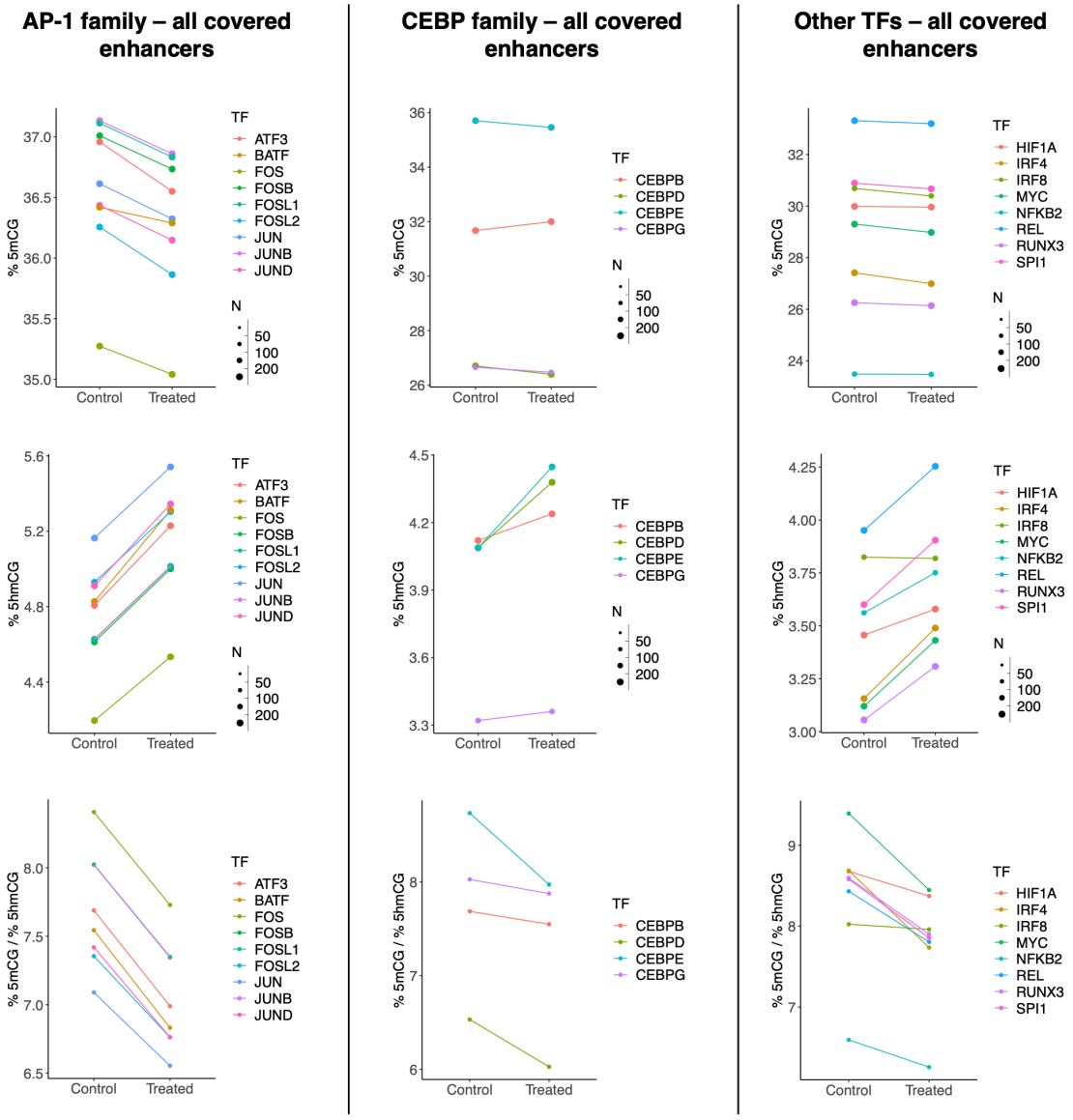
AP-1 family – all covered enhancers
CEBP family – all covered enhancers
Other TFs – all covered enhancers
% 5mCG
% 5hmCG
% 5mCG / % 5hmCG
Control
Treated
TF
ATF3
BATF
FOS
FOSB
FOSL1
FOSL2
JUN
JUNB
JUND
CEBPB
CEBPD
CEBPE
CEBPG
HIF1A
IRF4
IRF8
MYC
NFKB2
REL
RUNX3
SPI1
N
50
100
200

B

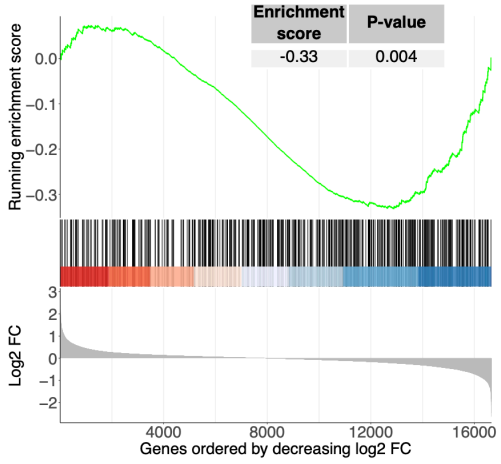
Enrichment score
P-value
-0.33
0.004
Running enrichment score
Log2 FC
Genes ordered by decreasing log2 FC

Supplementary Fig. S9. Single-base resolution analysis of 5mCG and 5hmCG in the proximity of TFs motifs in all covered enhancers of D-2HG-treated primary microglia. **(A)** Plots showing separate analysis of 5mCG and 5hmCG percentages (upper panel) in the proximity of binding motifs residing in all covered enhancers for the indicated TFs in D-2HG-treated microglia and paired untreated controls. The size of each dot indicates the number of motifs analyzed in a paired manner between the conditions. The 5mCG/5hmCG ratios in the analyzed regions are also shown. **(B)** GSEA using ranked genes by decreasing log2FC of D-2HG-treated vs. control RNA-seq samples. The plot shows a significant bias towards decreased expression of genes regulated by D-2HG-driven hypermethylated and hypohydroxymethylated enhancers bound by TFs depicted in Fig. 5C. Methylome/hydroxymethylome and RNA-seq analyses were conducted using the same samples in a paired manner.

A

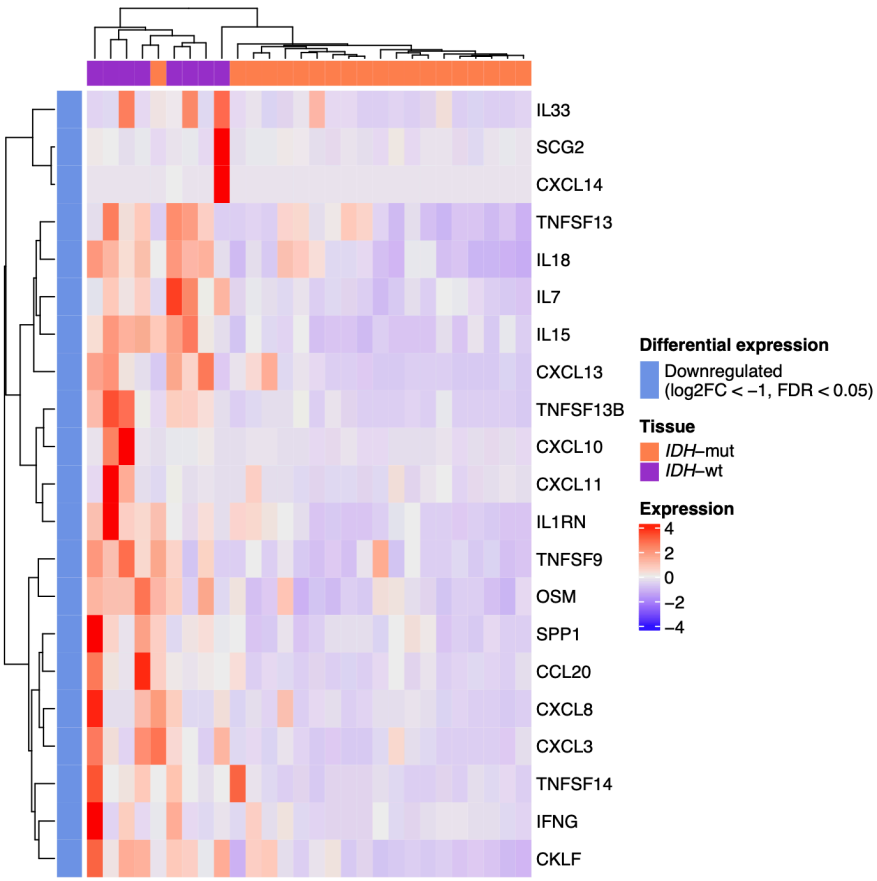
IL33
SCG2
CXCL14
TNFSF13
IL18
IL7
IL15
CXCL13
TNFSF13B
CXCL10
CXCL11
IL1RN
TNFSF9
OSM
SPP1
CCL20
CXCL8
CXCL3
TNFSF14
IFNG
CKLF
Differential expression
Downregulated
(log2FC < −1, FDR < 0.05)
Tissue
IDH–mut
IDH–wt
Expression
4
2
0
−2
−4

B

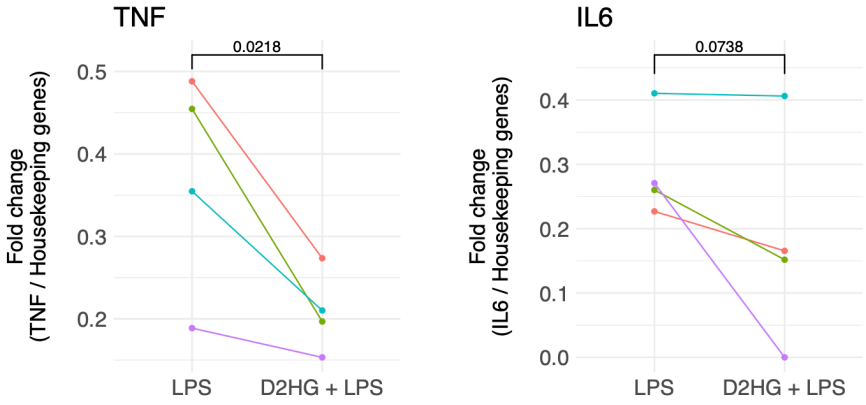
TNF
0.0218
Fold change
(TNF / Housekeeping genes)
0.5
0.4
0.3
0.2
LPS
D2HG + LPS
IL6
0.0738
Fold change
(IL6 / Housekeeping genes)
0.4
0.3
0.2
0.1
0.0
LPS
D2HG + LPS

C

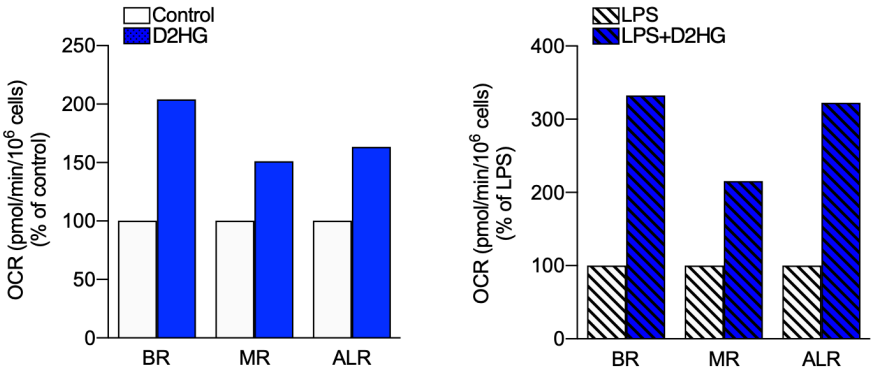
Control
D2HG
OCR (pmol/min/10^6 cells)
(% of control)
250
200
150
100
50
0
BR
MR
ALR
LPS
LPS+D2HG
OCR (pmol/min/10^6 cells)
(% of LPS)
400
300
200
100
0
BR
MR
ALR

Supplementary Fig. S10. Validation experiments on primary microglia treated with D-2HG for 14 days and challenged with LPS. (A) Heatmap depicting the expression of pro-inflammatory cytokines in CD11B+ cells from IDH^{mut} (n=20) and IDH^{wt} (n=8) human gliomas using RNA-seq data. **(B)** The plots indicate the expression of TNFA and IL6 (relative to housekeeping controls) in paired D-2HG-treated and control samples as determined by RT-qPCR. Primary microglia were obtained from surgical aspirates with IDH^{mut} status (n=4). P-values were calculated using a one-sided paired t-test. **(C)** Assessment of the oxygen consumption rate (OCR) in paired D-2HG-treated and control samples, as determined using the XFe extracellular flux analyzer. Basal respiration (BR), maximal respiration (MR), and ATP-linked respiration (ALR) parameters were compared between the control and D-2HG, and LPS vs. LPS+D-2HG. Primary microglia were obtained from the surgical aspirate of one IDH^{wt} meningioma. The cells were maintained, treated, and collected under the same conditions as those previously described (Fig. 6A).